ABSTRACT

Title of Document: ELECTRONIC TRANSPORT IN DIRAC MATERIALS: GRAPHENE AND A TOPOLOGICAL INSULATOR(Bi_2Se_3)

Sungjae Cho, Doctor of Philosophy, 2011

Directed By: Professor, Michael S. Fuhrer, Department of Physics

Materials with Dirac electronic spectra ("Dirac materials") have attracted much interest since the first successful electronic transport measurement in graphene in 2004. Dirac quasiparticles have novel physical properties such as absence of backscattering and Klein tunneling. Topological insulators are a more recently discovered class of materials that have a bulk band gap and gapless edge/surface states. The surface state in 3D topological insulators has a Dirac electronic spectrum like graphene, but is singly spin-degenerate, with spin-momentum locking. This thesis will describe electronic transport experiments in graphene and in Bi_2Se_3 ultrathin films, which are predicted to be either 2D topological insulators or conventional insulators.

The basic quantum physics of a particle confined in a box is demonstrated using electrons in single and bilayer graphene as examples of massless and massive

2D Fermions, respectively. Ballistic metal-graphene-metal devices act as Fabry-Pérot cavities for electrons, and resonant states of the Fabry-Pérot cavity observed in electronic transport are used to measure the density of states as a function of particle number for massless and massive 2D Fermions. Nonlocal spin-valve experiments are demonstrated up to room temperature in mesoscopic graphene contacted by ferromagnetic electrodes. At low temperature the spin-valve signal shows changes in magnitude and sign with back-gate voltage, which may also result from quantum-coherent transport through Fabry Pérot cavities.

The temperature- and magnetic-field-dependent longitudinal (ρ_{xx}) and Hall(ρ_{xy}) components of the resistivity of graphene were measured. Near the minimum conductivity point $\rho_{xx}(H)$ is strongly enhanced and $\rho_{xy}(H)$ is suppressed, indicating nearly equal electron and hole contributions to the current. The data are inconsistent with the standard two-fluid model, but consistent with the prediction for inhomogeneously distributed electron and hole regions of equal mobility.

Ultrathin three quintuple layer (3QL) Bi_2Se_3 field effect transistors (FETs) were fabricated by mechanical exfoliation on 300 nm SiO_2/Si susbtrates. Temperature and gate-voltage-dependent conductance measurements show a clear OFF state at negative gate voltage, with activated temperature-dependent conductance and energy barriers up to 250 meV, implying that 3QL-Bi_2Se_3 films are conventional insulators rather than 2D topological insulators, likely due to coupling of the topological surface states through the thin bulk.

ELECTRONIC TRANSPORT IN DIRAC MATERILAS: GRAPHENE AND A TOPOLOGICAL INSULATOR(Bi_2Se_3)

By

Sungjae Cho

Dissertation submitted to the Faculty of the Graduate School of the
University of Maryland, College Park, in partial fulfillment
of the requirements for the degree of
Doctor of Philosophy
2011

Advisory Committee:
Professor Michael S. Fuhrer, Chair
Professor H. Dennis Drew
Assistant Professor Johnpierre Paglione
Associate Research Scientist William G. Cullen
Professor Ichiro Takeuchi

Dedication

Dedicated to my mother

Acknowledgements

It has been 6 years since I began as a graduate student at the University of Maryland. After all these years, I have found that becoming an experimental physicist is not easy. I learned that an experimental physicist should have experimental techniques to realize physical ideas, a deep understanding of physics to follow the right direction in research and discover the hidden physical properties underneath experimental phenomena. I was full of confidence and not very modest at the beginning of graduate years. The past 6 years has taught me patience and modesty.

I was so lucky that I have had Prof. Michael Fuhrer as an advisor. He gave me enough freedom to test my experimental ideas while guiding me with his keen intuitions so that I did not get lost in research. He has always encouraged me even when I was not productive. He has been easily accessible and willing to answer my questions and discuss experiments to deepen my understanding of physics in given projects. I also thank him very much for giving me opportunities to do research on important issues.

I have had great lab mates and thank all of them. After I joined the group, I enjoyed discussing physics and experiments with Yung-Fu. We also worked together on my first paper. He is one of the smartest and the most diligent graduate students I have met at the University of Maryland. He recently became a faculty in Taiwan and I believe he will succeed in his academic career in the future. Todd was good at different experimental techniques. Enrique was humorous. Alex shares an office with me and always knows what she needs to do for her career and life. Dan liked doing exercises such as biking, was easygoing, but worked hard enough. Adrian was willing

to answer my questions on chemistry. Dave and Gokhan were good at computer programming. Tarek had experiences and physical knowledge. Chaun is efficient and productive in working. Shudong has a good understanding of physics and it is fun to talk to him about physics. Harold, Dohun and Liang work hard and are highly motivated. Jack, Jinglei and Dohun do their experiments so well and make it hard to believe they are 2^{nd} year graduate students. Jun gave me advice on giving presentations and has sharp understanding of the field he is studying. Claudia works hard, but unfortunately I have not had many chances to work with her.

I thank Dr. Euyheon Hwang for discussing theoretical physics problems with me even when they are not directly related to his field. Prof. Dennis Drew gave me important advices on my careers such as what to consider when applying for postdoc jobs and so on. He was also willing to share his deep understandings on topological insulator and graphene with me. I thank Prof. Johnpierre Paglione and Dr. Nick Butch for collaboration on topological insulators and helpful discussion about experiments. They grow some of the highest quality Bi_2Se_3 crystals. I thank Prof. Ian Appelbaum for discussing topological insulators, giving me advice on spintronics experiment and helping me to choose the right place for a postdoc job. Dr. Bill Cullen is the most experienced scientist in our lab about UHV systems and surface physics, and helped me a lot when I had problems in experiment. I also thank my dissertation committee, Prof. Ichiro Takeuchi, Prof. Dennis Drew, Prof. Johnpierre Paglione, Dr. Bill Cullen and Prof. Michael Fuhrer for spending their valuable time.

I want to thank Brian Straughn, who I bothered often when there were problems with equipment in CNAM. He was always willing to fix them as quickly as possible so that the problems in equipment did not make my progress stall.

I thank my wife, Sooyeon for always being with me through good and bad times, supporting me in every way and taking care of our lovely one year old son Woojin(Aiden). He makes me happy by smiling at me and playing with me at home. I also thank my parents-in-law for their mental support. I thank my brother Sungmin, sister Yeonkyeong, sister-in-law and brother-in-law. Finally, I want to thank my mother, who has been my big supporter. She has always understood, believed in and encouraged me. I can’t thank her enough in words.

Thank you all.

Table of Contents

Dedication ii

Acknowledgements iii

Table of Contents vi

List of Figures viii

Chapter 1: Introduction to Graphene 1

1.1 Lattice Structure of Graphene 1

1.2 Band Structure of Graphene 2

1.3 Low Energy Dispersion in Single Layer Graphene-Massless Fermion 7

1.4 Low Energy Dispersion in Bilayer Graphene-Massless Fermion 9

1.5 Organization of Thesis 14

Chapter 2: Graphene Fabrication and Characterization 17

2.1 Graphene Fabrication Method 17

2.2 Gate Tunable Device Fabrication Method 20

2.3 Graphene Characterization; Single Layer and Bilayer Graphene 24

2.3.1 Anomalous Quantum Hall Effect(QHE) ..... ……24

2.3.2 Raman Spectra of Graphene ..... ……29

Chapter 3: Massless and Massive Particle-in-a-box States in Single and Bilayer Graphene……..33

3.1 Density of States in Single and Bilayer Graphene 34

3.2 Sample Preparation and Characterization 37

3.3 Fabry-Pérot Interference Measurement and Discussion 42

3.3 Conclusion 48

Chapter 4: Charge Transport and Inhomogeneity near the Minimum Conductivity Point…...……..50

4.1 Minimum Conductivity and Electron-Hole Puddles in Graphene 50

4.2 Device Characterization(field effect mobility and QHE) 53

4.3Magnetoresistivity near Minimum Conductivity Point(MCP) 54

4.4 Conclusion 63

Chapter 5: Gate Tunable Graphene Spin Valve……...64

5.1 Why Graphene for Spintronics?..... 64

5.2 Nonlocal spin valve effect 65

5.3 Fabrication and Characterization 67

5.4 Gate-Modulated Spin Valve Measurement..... 69

5.5 Conclusion 77

Chapter 6: Insulating Behavior in Ultra-thin Bismuth Selenide Field Effect Transistors…….……...79

6.1 Introduction to Topological Insulator 79

6.2 Sample Fabrication and Characterization 84

6.3 Electrical Measurement and Discussion 85

6.4 Conclusion 91

Bibliography 92

List of Figures

Figure 1.1: Graphene lattice structure……1

Figure 1.2: Graphene band structure(tight binding model)……...6

Figure 1.3: Low energy dispersion of graphene…….……...8

Figure 1.4: Bilayer graphene lattice structure...…….…….11

Figure 1.5: Low energy band structure of bilayer graphene...…….13

Figure 2.1: Optical images of single and bilayer graphene...……..19

Figure 2.2: Optical images of single and bilayer graphene devices..……..20

Figure 2.3: Conductivity of graphene as a function of gate voltage..……..22

Figure 2.4: Charge carrier density and mobility of graphene as a function of gate voltage..……..……..23

Figure 2.5: quantum hall effect in single layer graphene…….…..……..26

Figure 2.6: quantum hall effect in bilayer graphene…….…..…….28

Figure 2.7: Raman spectra of graphene…….…..……29

Figure 2.8: Raman scattering process in single layer graphene..……30

Figure 2.9: Raman scattering process in bilayer graphene..……31

Figure 3.1: Energy of particle in a box for massless and massive fermions……36

Figure 3.2: Optical images of measured devices……..……...38

Figure 3.3: Quantum hall effect measured in the devices……....39

Figure 3.4: Two probe conductance in the devices……..41

Figure 3.5: Fabry Perot resonance in 2D(V_{sd}-V_g) conductance plot for single layer graphene device…….……..42

Figure 3.6: Fabry Perot resonance in 2D(V_{sd}-V_g) conductance plot for additional single layer graphene device……..……..43

Figure 3.7: Fabry Perot resonance in 2D(V_{sd}-V_g) conductance plot for bilayer graphene device…….……..44

Figure 3.8: Density of graphene…….……..46

Figure 4.1: Spatial density variations in graphene…….……..52

Figure 4.2: Conductivity and quantum hall effect in the graphene device measured..53

Figure 4.3: Longitudinal resistivity near Dirac point measured as a function of magnetic field at various temperatures.……...55

Figure 4.4: Longitudinal resistivity and conductivity near Dirac point measured as a function of magnetic field at various gate voltages…..……...57

Figure 4.4: Longitudinal resistivity near Dirac point fitted to a model……...59

Figure 5.1: Nonlocal spin valve effect…….……...65

Figure 5.2: Graphene spin valve device and conductivity measurement….……...67

Figure 5.3: Nonlocal spin valve effect in graphene…….…..……...70

Figure 5.4: Gate-voltage dependence of spin valve signal.…….…..……...72

Figure 5.5: Temperature dependence of spin valve signal.…….…..……...75

Figure 5.6: Fabry Perot resonance measured in a spin valve device..….…..……...76

Figure 6.1: Dispersion of surface states in Bi_2Se_3 ; calculation and ARPES data…...80

Figure 6.2: ARPES spectra of ultrathin Bi_2Se_3……...81

Figure 6.3: QHE and QSHE……....82

Figure 6.4: QSHE in HgTe quantum well……...83

Figure 6.5: AFM and optical images of ultrathin Bi_2Se_3.…….……...84

Figure 6.6: Gate voltage dependent conductivity in exfoliated Bi_2Se_3……...86

Figure 6.7: Temperature-dependent conductivity in ultrathin Bi_2Se_3..……...88

Figure 6.8: Activation energy as a function of gate voltage……...…….…...89

Chapter 1. Introduction to Graphene

1.1 Lattice Structure of Graphene

Graphene is a single atomic layer composed of carbon atoms arranged in 2D hexagonal lattice. Discovery of this true 2D material in 2005[1-3] has intrigued vigorous research in both theoretical and experimental condensed matter physics. Graphene is unique since its many physical properties are different from conventional two dimensional electron gas (2-DEG) system.

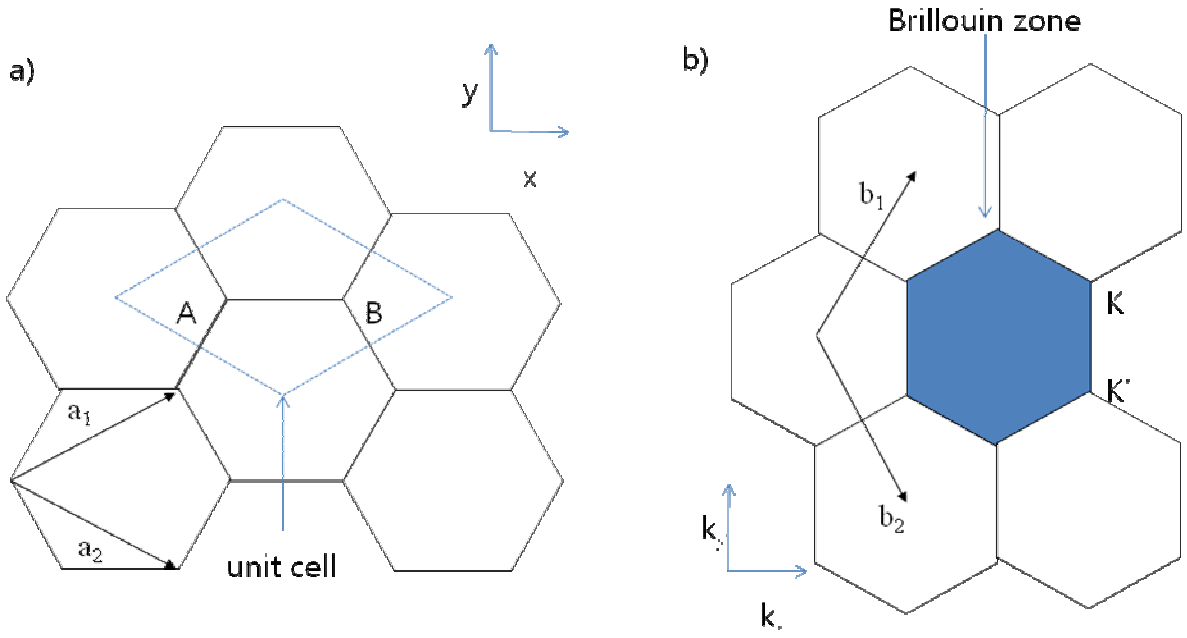

Fig.1.1 a)graphene honeycomb lattice. A and B are two carbon atoms in a unit cell[1]. Carbon atoms are located at corners of hexagons and sp^2 bonding between carbon atoms are depicted as lines. a_1 and a_2 are two primitive vectors. b)reciprocal lattice of graphene. The shaded hexagon is the first Brillouin zone.

As in Fig.1.1(a), graphene has honeycomb lattice structure[4-7]. Each carbon atoms are located at edges of hexagons. The unit cell of this honeycomb lattice is triangular and composed of two carbon atoms often called A and B. The unit vectors in real space are

$$\vec{a}_1 = (\frac{\sqrt{3}}{2}a, \frac{a}{2}), \vec{a}_2 = (\frac{\sqrt{3}}{2}a, -\frac{a}{2}) \tag{1.1}$$

where the lattice constant a=2.46Å.

The reciprocal lattice is also honeycomb as in Fig.1.1(b), and the reciprocal lattice vectors are

$$\vec{b}_1 = (\frac{2\pi}{\sqrt{3}a}, \frac{2\pi}{a}), \vec{b}_2 = (\frac{2\pi}{\sqrt{3}a}, -\frac{2\pi}{a}) \tag{1.2}$$

where the lattice constant is $4\pi/\sqrt{3}a$

The Brillouin zone is shown in Fig1.1(b) and the two inequivalent corners in the first Brillouin zone are called K and K' points.

1.2 Band Structure of Graphene

Out of four valence electrons in carbon atoms, three are used to form σ bonds hybridizing in sp^2 configuration. The other fourth electron forms p_z orbital, perpendicular to graphene plane and this p_z orbital forms so-called π bands in graphene. π bands are the most important in different physical properties of graphene at low energy regime. Since there are two carbon atoms in a unit cell, there are two such bands called π and π* bands.

I review the calculation of the π band dispersion of graphene by considering a simple tight binding model[8] following Wallace's method[4-6]. The Bloch wavefunction[8] can be written as

$$\Psi_{\vec{k}} = \sum_{\vec{R}} e^{i\vec{k}\cdot\vec{R}} \phi(\vec{x} - \vec{R}) \tag{1.3}$$

where the lattice vector $\vec{R} = m_1 + m_2$ (m_1, m_2 =integer) and $\phi(\vec{x})$ is the p_z atomic wave function. Following LCAO approximation, only considering nearest-neighbor interactions and the total wave function $\phi(\vec{x})$ can be described as a linear combination of two Bloch functions at the two inequivalent carbon atoms at A and B in Fig.1.1(a).

$$\phi(\vec{x}) = b_1\phi_1(\vec{x}) + b_2\phi_2(\vec{x}) \tag{1.4}$$

The Hamiltonian for an electron in graphene can be written as

$$H = \frac{\vec{p}_2}{2m} + \sum_{\vec{R}} [V(\vec{x} - \vec{x}_1 - \vec{R}) + V(\vec{x} - \vec{x}_2 - \vec{R})] \tag{1.5}$$

Where $\vec{x}_1$ and $\vec{x}_2$ are the position vectors of two carbon atoms in a unit cell and V is the atomic potential.

Applying this Hamiltonian to ϕ_1, one obtains

$$H\phi_1 = E_1\phi_1 + \{\sum_{\vec{R}} [V(\vec{x} - \vec{x}_1 - \vec{R}) + V(\vec{x} - \vec{x}_2 - \vec{R}) + V(\vec{x} - \vec{x}_2)]\}\phi_1 \tag{1.6}$$

where E_1 is an eigenvalue of the atomic p_z orbital state for carbon atom A. With a similar equation for ϕ_2, these two equations can be rewritten using abbreviations as

$$H\phi_{1,2} = E_{1,2} + \Delta V_{1,2}\phi_{1,2} \qquad (1.7)$$

$E_1 = E_2$ from symmetry and I can further choose $E_1 = E_2 = 0$. Then Eqn. 1.7 becomes

$$H\phi_1 = \Delta V_1\phi_1 \text{ and } H\phi_2 = \Delta V_2\phi_2 \qquad (1.8)$$

Now, the Schrödinger equation is used to find b_1 and b_2.

$$H\Psi_{\vec{k}} = E(\vec{k})\Psi_{\vec{k}} \qquad (1.9)$$

By projecting ϕ_1 and ϕ_2 to the equation (1.9), one gets

$$E(\vec{k}) < \phi_i \mid \Psi > = < \phi_i \mid \Delta V_i \mid \Psi > \qquad (1.10)$$

Here, the left-hand side of equation (1.10) can be calculated as

$$\begin{aligned} < \phi_1 \mid \Psi > &= b_1 + b_2(\int \phi_1^* \phi_2)(1 + e^{-i\vec{k}\cdot\vec{a}_1} + e^{-i\vec{k}\cdot\vec{a}_2}) \\ < \phi_2 \mid \Psi > &= b_2 + b_1(\int \phi_2^* \phi_1)(1 + e^{i\vec{k}\cdot\vec{a}_1} + e^{i\vec{k}\cdot\vec{a}_2}) \end{aligned} \qquad (1.11)$$

I now denote

$$\beta = \int \phi_1^* \phi_2 = \int \phi_2^* \phi_1 \qquad (1.12)$$

and these integrals are equal due to symmetry.

The right-hand sides of the equations (1.10) are obtained as

$$\begin{aligned} < \phi_1 \mid \Delta V_1 \mid \Psi > &= b_2\gamma_0(1 + e^{-i\vec{k}\cdot\vec{a}_1} + e^{-i\vec{k}\cdot\vec{a}_2}) = b_2\gamma_0 f(\vec{k}) \\ < \phi_2 \mid \Delta V_2 \mid \Psi > &= b_1\gamma_0(1 + e^{i\vec{k}\cdot\vec{a}_1} + e^{i\vec{k}\cdot\vec{a}_2}) = b_1\gamma_0 f(\vec{k})^* \end{aligned} \qquad (1.13)$$

where

$$\gamma_0 = \int \phi_1^* \Delta V_1 \phi_2 = \int \phi_2^* \Delta V_2 \phi_1 \tag{1.14}$$

These two integrals are also equal due to symmetry.

With equations (1.10)(1.11) and (1.13) into the Schrodinger equation (1.9), the eigenvalue equation becomes

$$\begin{pmatrix} E(\vec{k}) & f(\vec{k})^*(\beta E(\vec{k}) - \gamma_0) \\ f(\vec{k})(\beta E(\vec{k}) - \gamma_0) & E(\vec{k}) \end{pmatrix} \begin{pmatrix} b_1 \\ b_2 \end{pmatrix} = \begin{pmatrix} 0 \\ 0 \end{pmatrix} \tag{1.15}$$

Considering β is small, from determinant of the left hand side = 0, the dispersion relation is

$$E(\vec{k}) = E(k_x, k_y) = \pm\gamma_0 \mid f(\vec{k}) \mid \tag{1.16}$$

$$E(\vec{k}) = \pm\gamma_0 \sqrt{1 + 4\cos\left(\frac{k_x\sqrt{3}a}{2}\right)\cos\left(\frac{k_y a}{2}\right) + 4\cos^2\left(\frac{k_y a}{2}\right)} \tag{1.17}$$

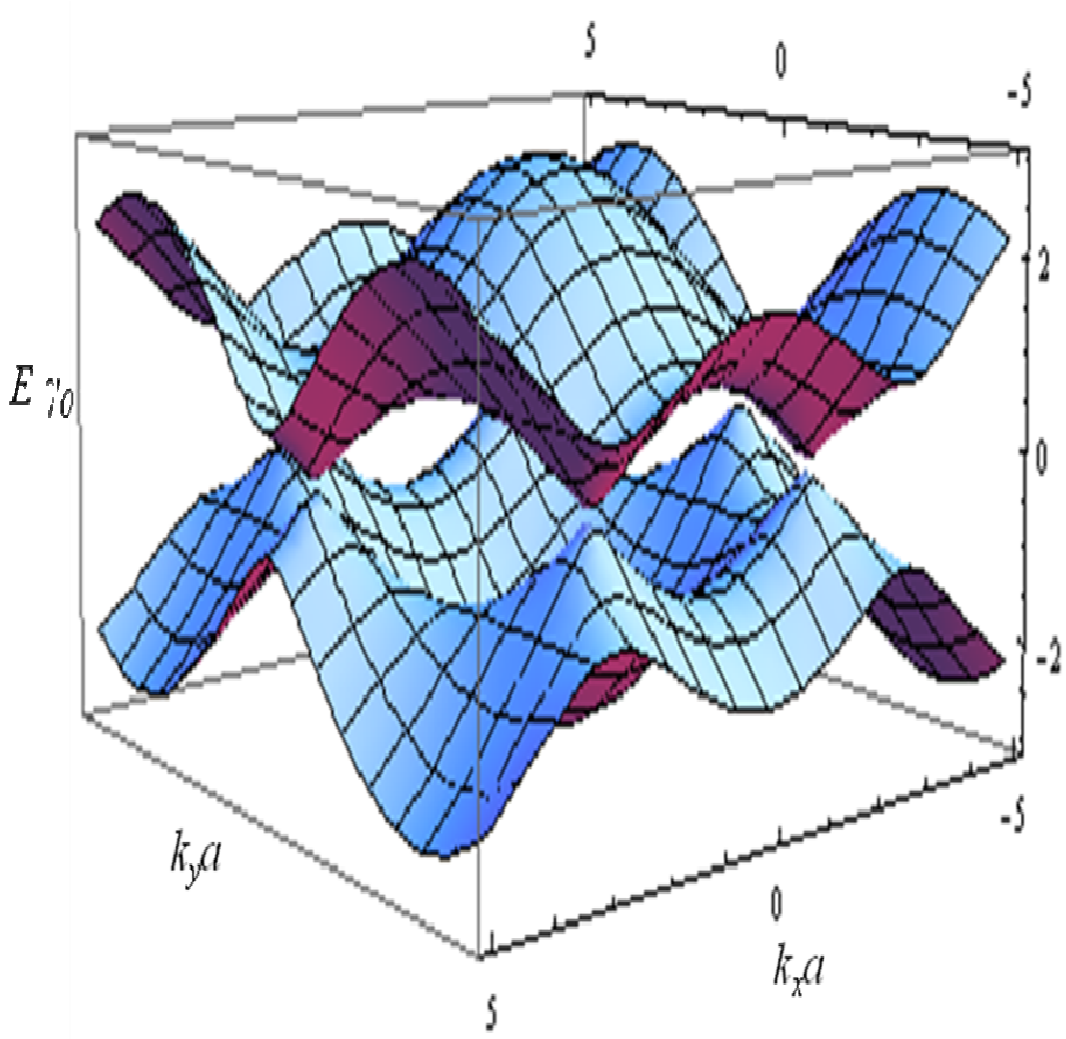

Fig.1.2 plot of graphene band structure calculated by tight binding model (Eqn. 1.17). The π (valence) and π*(conduction) bands touch each other at K and K' points.

The energy dispersion relation (1.17) is plotted in Fig1.2. As discussed earlier, there are two bands; π(valence) and π*(conduction) bands. Since these two bands touch each other at six corners of Brillouin zones,i.e. K and K' points, graphene is semimetal or zero gap semiconductor. Since one carbon atom contributes one π electron, the valence band is completely filled, and thus the Fermi level passes through K and K' points and $E_F = 0$.

1.3 Low Energy Dispersion in Single Layer Graphene – Massless Fermion

In the low energy regime, one only needs to consider the first order expansion near K and K' points. From Fig.1.2 it is obvious that the dispersion relation near K, K' points will be linear. Near the K point, one can write

$$\vec{k} = \Delta\vec{k} + \vec{K} \tag{1.18}$$

$$E(\vec{k}) = E(\Delta\vec{k}) + E(\vec{K}) \tag{1.19}$$

If I expand $f(\vec{k})$ to the first order, equation (1.15) becomes

$$-\frac{\sqrt{3}\gamma_0 a}{2}\begin{pmatrix} 0 & \Delta k_x - i\Delta k_y \\ \Delta k_x + i\Delta k_y & 0 \end{pmatrix}\begin{pmatrix} b_1 \\ b_2 \end{pmatrix} = E(\Delta\vec{k})\begin{pmatrix} b_1 \\ b_2 \end{pmatrix} \tag{1.20}$$

From setting the determinant equal to zero, this equation is reduced to a simple linear dispersion relation,

$$E(\Delta\vec{k}) = \pm \mathrm{h} v_F \,|\, \Delta\vec{k} \,| \tag{1.21}$$

$$v_F = \frac{\sqrt{3}\gamma_0 a}{2\mathrm{h}} \tag{1.22}$$

where $v_F \sim 10^6$m/s is the Fermi velocity. Thus, in the low energy regime near K, K' points, the energy changes linearly with $\Delta\vec{k}$. In other words, the energy dispersion at low energy can be described by two cones touching each other at the apices where Fermi level passes.

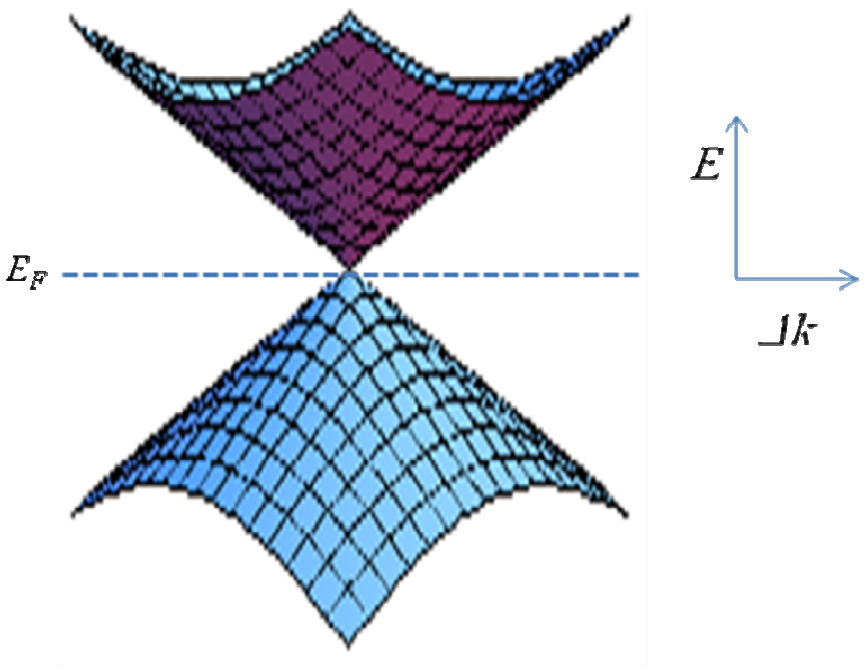

Fig.1.3 Low energy linear energy-momentum dispersion of graphene.

This linear dispersion at low energy gives very interesting properties to graphene since it resembles equations describing massless relativistic particles such as photons. The energy dispersion relation of relativistic particles according to Dirac equation[9]is given by

$$E = \pm\sqrt{c^2 \mathrm{h}^2 k^2 + m^2 c^4} \qquad (1.23)$$

If the mass m is zero, the dispersion relation becomes

$$E = \pm c \mathrm{h} \,|\, \vec{k} \,| \qquad (1.24)$$

which is exactly the same as graphene low energy dispersion equation (1.21) if c is replaced by Fermi velocity v_F. Thus, electrons in graphene are called massless Dirac fermions and the low energy dispersion relation is called Dirac cones.

1.4 Low energy dispersion in Bilayer Graphene - Massive Fermion

In this section, I discuss the electronic dispersion in bilayer graphene with Bernal (AB) stacking (Fig.1.4) since both naturally occurring graphite and mechanically exfoliated bilayer graphene obtained from graphite show this structure[10]In Bernal stacked bilayer graphene, a unit cell is composed of four carbon atoms, i.e. two inequivalent atom A1,B1 in the bottom layer and the other two inequivalent atom A2, B2 in the top layer. A2 in the top layer lies directly above the center of honeycomb of bottom layer and B2 is located directly above A1 as shown in Fig. 1.4a).

The band structure of bilayer graphene can be also calculated using a simple tight binding model[11-16]. The Hamiltonian for Bernal stacked bilayer graphene is a 4x4 matrix instead of 2x2 for single layer graphene. While in single layer one only needs to consider one tight binding parameter γ_0, following the Slonczewski-Weiss-McClure parameterization[17-18] of relevant couplings, I define two more parameters γ_1 and γ_3 as seen in Fig. 1.4b). γ_0 is the in-plane coupling constant between A1 and B1(A2 and B2), γ_1 is the strongest interlayer coupling, between A1 and B2. I also express weaker coupling between A2 and B1 by γ_3. Here I ignore the possibility of layer asymmetry, i.e. a difference in potential between bottom and top layers which may be caused by the environment or intentionally by top-and bottom-gating, and which can have additional interesting effects on bandstructure[19].

The Hamiltonian in the basis of $\Psi = (\phi_{A1}, \phi_{B2}, \phi_{A2}, \phi_{B1})$ near K point ($\Psi = (\phi_{B2}, \phi_{A1}, \phi_{B1}, \phi_{A2})$ near K' point), can be written as

$$H = \zeta \begin{pmatrix} 0 & v_3 p_+ & 0 & v_0 p_- \\ v_3 p_- & 0 & v_0 p_+ & 0 \\ 0 & v_0 p_- & 0 & \zeta\gamma_1 \\ v_0 p_+ & 0 & \zeta\gamma_1 & 0 \end{pmatrix} \qquad (1.25)$$

where

$$v_0 = \frac{\sqrt{3}\gamma_0 a}{2\mathrm{h}} \qquad (1.26)$$

$$v_3 = \frac{\sqrt{3}\gamma_3 a}{2\mathrm{h}} \qquad (1.27)$$

$$p_\pm = p_x \pm i p_y \qquad (1.28)$$

momentum $\mathbf{p}=(p_x,p_y)$ is measured from K,K' points and ζ=1 or -1 corresponds to K or K' points.

By diagonalizing the Hamiltonian (1.25), the energy-momentum dispersion of bilayer graphene can be obtained. While single layer graphene has one conduction and one valence band, bilayer graphene has two conduction and two valence bands since there are four carbon atoms in a unit cell. While two of those four bands, $E^{(1)}$, touch each other, the other two $E^{(2)}$ are separated by $2\gamma_1$. $E^{(1)}$ and $E^{(2)}$ are given by[7]

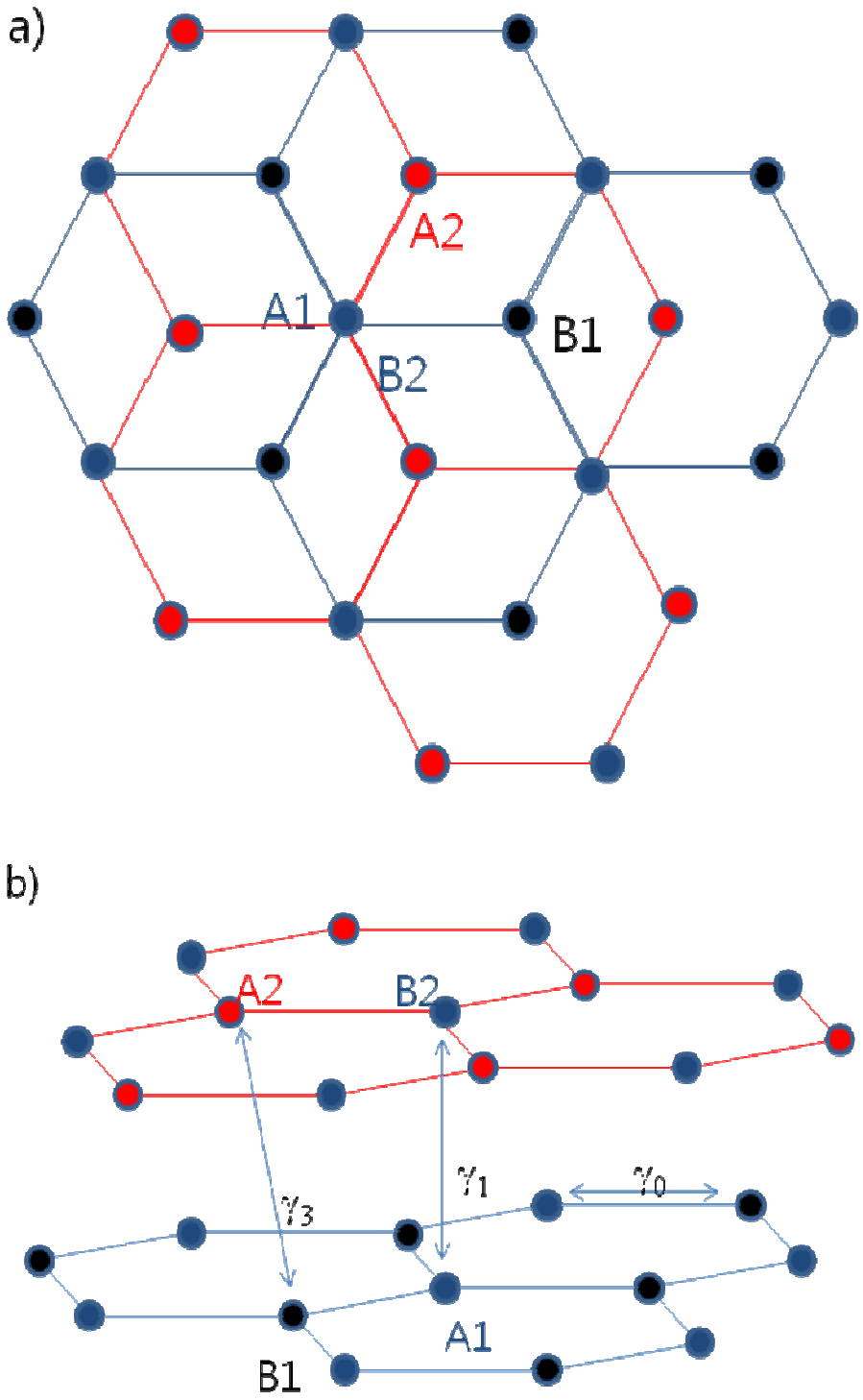

Fig.1.4 Schematics of bilayer graphene lattice structure. a) Planar view of Bernal(AB) stacked bilayer graphene. b) Atoms A1 (blue), B1 (black) are in the bottom layer and A2 (red), B2 (blue) are in the top layer. γ_0, γ_1, γ_3 are tight binding hopping parameters between atoms as illustrated in (b).

$$E^{(a)} = \pm\left[\frac{\gamma_1^2}{2} + \left(v_0^2 + \frac{v_3^2}{2}\right)p^2 + (-1)^a\left[\frac{(\gamma_1^2 - v_3^2 p^2)^2}{4} + v_0^2 p^2[\gamma_1^2 + v_3^2 p^2] + 2\zeta\gamma_1 v_3 v_0^2 p^3 \cos 3\theta\right]^{1/2}\right]^{1/2} \quad (1.29)$$

where $\mathbf{p}=p(\cos\theta,\sin\theta)$ near K point.

$E^{(1)}$ describes dispersion relation in relatively low energy region. In the intermediate energy, $E^{(1)}$ can be approximated[11] as hyperbolic:

$$E^{(1)} \sim \pm\frac{1}{2}\gamma_1\left(\sqrt{1+4v_0^2 p^2/\gamma_1^2} - 1\right) \quad (1.30)$$

The effective mass corresponding to this dispersion relation, $E^{(1)}$, is given by

$$m^* = \frac{p}{\partial E^{(1)}/\partial p} = \left(\gamma_1/2v_0^2\right)\sqrt{1+4\pi \mathrm{h}^2 v_0^2 n/\gamma_1^2} \quad (1.31)$$

Equation 1.29 can be further approximated in two regime; high density and low density regime. At high density regime, energy dispersion becomes linear,

$$E^{(1)} \sim v_0 p \quad (1.32)$$

At low density regime, energy dispersion is quadratic,

$$E^{(1)} \sim \frac{p^2}{2m^*}, m^* = \frac{\gamma_1}{2v_0^2} \quad (1.33)$$

The crossover between these two regimes occurs at carrier density $n^{(1)}$

$$n^{(1)} = \frac{\gamma_1^2}{4\pi \mathrm{h}^2 v_0^2} \quad (1.34)$$

This density can be estimated as $n^{(1)} \sim 4.4 \times 10^{12}\mathrm{cm}^{-2}$ using graphite experimental values[11]. The density where $E^{(2)}$ starts occupied also is

$$n^{(2)} \sim \frac{2\gamma_1^2}{\pi \mathrm{h}^2 v_0^2} \sim 8n^{(1)} \qquad (1.35)$$

and the estimated value is accordingly $n^{(2)}$ ~3.5 x 10^{13}cm^{-2}. At sufficiently low carrier density, the quadratic dispersion (1.33) is a good approximation and in most low energy bilayer experiments, I do not need to take higher density bands $E^{(2)}$ into consideration since they are not occupied.

The low energy dispersion of bilayer near K point is plotted in Fig. 1.5. Comparing Fig.1.5 with Fig. 1.3, the most distinctive point between low energy dispersion of single and bilayer graphene is that dispersion of single layer is massless and dispersion of bilayer is massive.

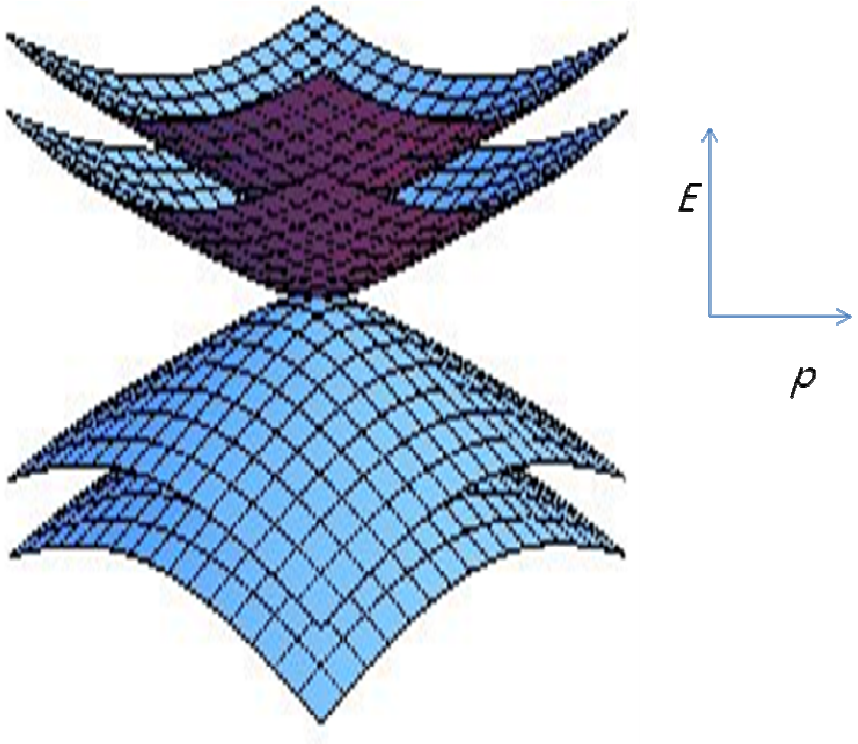

Fig.1.5 Low energy band structure of bilayer graphene (Eqn. 1.29).

1.5 Organization of Thesis

The outline of this thesis is as follows;

In chapter 2, I will describe fabrication and characterization of single and bilayer graphene. Two most common characterization methods will be explained; anomalous quantum hall effect[1, 3, 20] and Raman spectroscopy[21].

In chapter 3, I will demonstrate one of the most basic problems in quantum mechanics; properties of wavelike particles confined in a hard-walled box of single and bilayer graphene. I will show that mesoscopic, ballistic[22] single-layer[2-3] and bi-layer[15, 23] metal-graphene-metal devices act as Fabry-Perot cavities for electrons confined between the atomically-sharp partially-reflective metal leads. Electronic conduction occurs through resonant states of the Fabry-Pérot cavity, which are exactly analogous to the particle-in-a-box states of an electron confined by perfectly reflective walls. $D(n)$ is measured, and the expected dependences on particle number will be verified: $D \sim n^{1/2}$ for massless particles in single-layer graphene, and $D \sim$ constant for massive particles in bi-layer graphene. The results discussed in this chapter are published in *Nano Research*[24].

In chapter 4, I will discuss magnetoresistance of graphene and nature of charge transport near charge neutrality point. I find a large magnetoresistance associated with the minimum conductivity point, which results from the presence of two carrier types (electrons and holes) within the sample. The functional form of the magnetoresistance does not follow a conventional two-fluid model typical of a semimetal, but instead is consistent with effective-medium-theory results for an inhomogenous spatial distribution of regions with equal charge carrier mobility but

opposite charge carrier sign[25]. The results support the picture of charge inhomogeneity dominating the conductivity at the minimum conductivity point in graphene[26-27]. The results discussed in this chapter are published in *Physical Review B Rapid Communications*[28].

In chapter 5, I will talk about spin valve effect in graphene. I observed clear switching of the non-local four-probe resistance of graphene spin-valves due to switching of the magnetization of ferromagnetic spin injector contacts. The spin signal was observable up to room temperature. Interestingly, the spin signal fluctuated with gate voltage, even changing sign. I propose that these fluctuations, in my rather short spin valve devices, are due to Fabry-Perot oscillations as discussed in Chapter 3.The results discussed in this chapter are published in *Applied Physics Letter*[29].

In chapter6, I will introduce my research on insulating behavior in ultra-thin bismuth selenide(Bi_2Se_3) field effect transistors. Bi_2Se_3 is a newly discovered material known as 3D topological insulator. Topological insulators are new class of materials that have a bulk band gap and gapless Dirac surface states which are topologically protected from back scattering or localization by time-reversal symmetry. The existence of surface states in Bi_2Se_3 was observed recently by angle-resolved photoemission spectroscopy (ARPES)[30-32] and scanning tunneling spectroscopy (STS)[33-35]. I will briefly introduce a topological insulator and crossover of it properties from 3D to 2D[36]. Then, I will focus on my experimental result that shows 2D ultrathin film opens an energy gap and becomes trivial trivial insulator. Temperature- and gate-voltage dependent conductance measurements show

that ultrathin Bi_2Se_3 FETs are *n*-type, and have a clear OFF state at negative gate voltage, with activated temperature-dependent conductance and energy barriers up to 250 meV. The results discussed in this chapter are published in *Nano Letters*[37].

Chapter 2. Graphene Fabrication and Characterization

2.1 Graphene Fabrication Method

Since its first discovery[1-3], there have been two categories of graphene fabrication method; top-down and bottom-up. Bottom-up methods start from carbon atoms or carbon-containing molecules or solids and assemble graphene sheets in chemical ways. Epitaxial growth on crystalline silicon carbide surface[23, 38] and chemical vapor deposition growth[39] have been two most successful methods in this category. These methods open up possibility of large-area graphene suitable for applications in electronic industry.

The top-down method starts from bulk graphite(HOPG or natural graphite) and mechanically exfoliates one or several layers of graphene on substrates[1-3]. There had been many unsuccessful attempts to exfoliate a single layer graphene[40-41] until in 2005 a very surprisingly simple and successful way of fabricating a single layer graphene was discovered[2], which is often called the “Scotch tape method”. I used this Scotch tape method to fabricate graphene and thus I will describe “Scotch tape method” in details below.

The Scotch Tape Method is simple and easy. As reported in earlier paper[2], I peel thick layers of graphite from bulk Kish graphite(Toshiba Ceramics) with Scotch tape and rub them against a SiO_2(300nm)/Si surface. During this rubbing, one or two

layers of graphene is often peeled off and attached to the SiO_2 substrate due to Van der Waals force

In next step, I take the graphite-rubbed SiO_2/Si chips to optical microscope. Under optical microscope, graphene on SiO_2(300nm) is clearly visible and somewhat transparent. There is a slight color and contrast shift due to interference[42]. This fabrication method is also applicable to obtain graphene on other substrates such as mica, Sc_2O_3 and STO.

Even though this method seems dirty because of scotch tape, it produces graphene of the highest quality among all fabrication methods with charge carrier mobility greater than $10^4 cm^2/Vs$[28, 39]. While it is not suitable for mass-production, I was able to use the scotch tape method to obtain graphene as large as 100μm x 100μm.

Bi-layer graphene shows slightly darker color and contrast than single layer graphene as seen in Fig.2.1. This is an interference-induced color and contrast change due to a slightly larger thickness of bilayer graphene. I will describe how to characterize single and bilayer graphene in more detail in Section 2.3.

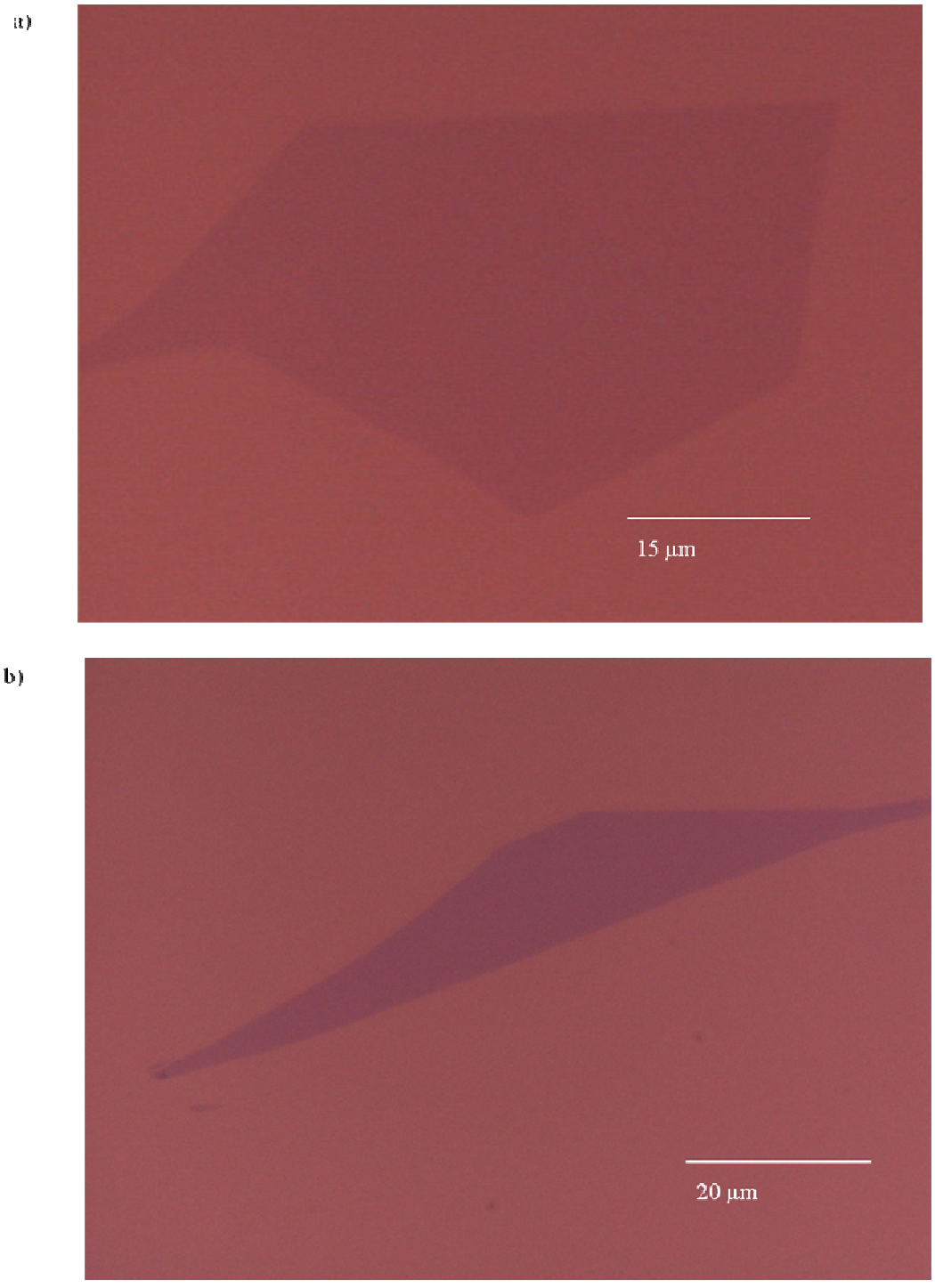

Fig.2.1 Optical images of a) single layer graphene b) bilayer graphene on SiO_2/Si substrates. Graphene is slightly darker than the substrate, and single layer graphene is slightly more transparent than bilayer graphene.

2.2 Gate Tunable Device Fabrication Method

Once graphene is found on the SiO_2/Si chip, I spin two layers of mma/pmma polymer and bake at 150°C for 10 minutes on a hot plate. Then, I use 30kV electron beam to pattern electrodes in electron beam lithography and develop the pattern in MIBK:IPA 3:1 solution. Finally, electrode windows are exposed and I evaporate metal (for normal contacts, Cr/Au=5nm/50nm) in a thermal evaporator at pressure below $2x10^{-6}$ Torr. In the final step, I perform lift-off procedure in acetone for two hours. For quantum hall effect measurement, I choose square shaped graphene piece and deposit Hall bar electrodes without etching graphene as seen in Fig.2.2 since etching normally reduces quality of graphene.

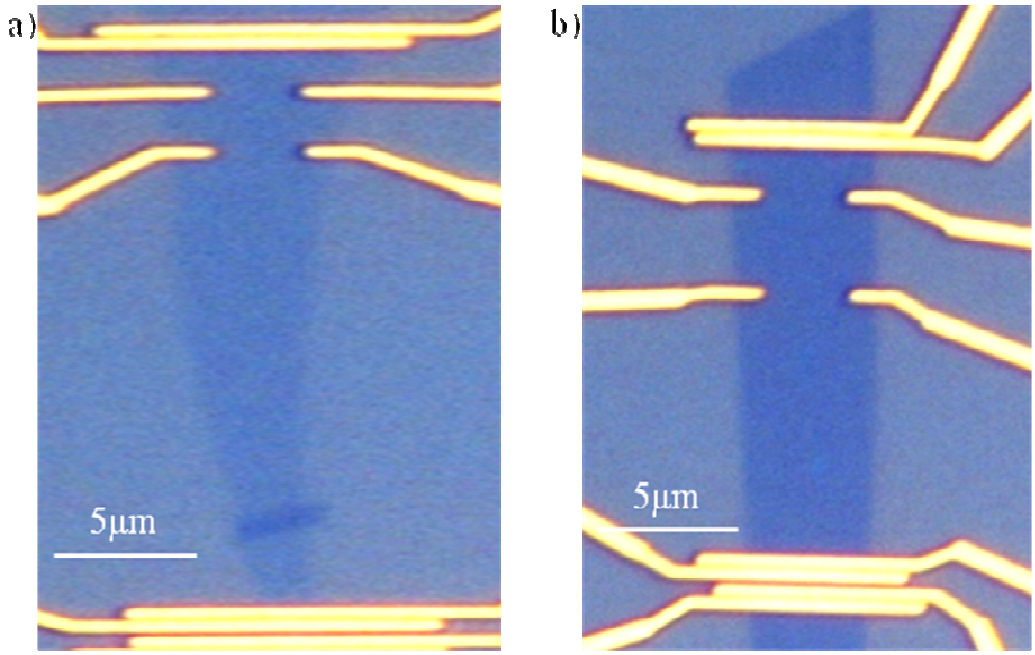

Fig.2.2 optical picture of a) single layer b) bilayer graphene device. Hall bar geometry was made to measure R_{xx} and R_{xy} .

Once I finished fabricating devices as in Fig.2.2, I performed electrical transport measurements in our cryostat in which temperature can be varied from 320K-0.3K.

The heavily doped 300nm thick SiO_2 serves as dielectrics for back gate. By tuning back gate voltage, the carrier density can be modulated in graphene. Fig. 2.3b) shows the conductivity $\sigma_{xx}$of a graphene sample as a function of gate voltage measured at temperature T = 2K. The conductivity curve shows minimum region and it is called “minimum conductivity point”, or “Dirac point” [2-3, 10]; [1, 3, 28] the gate voltage at which the minimum conductivity occurs. In this thesis, I will call it V_D. As more charge (electron or hole) carriers are induced in graphene by increasing V_g, the conductance in graphene increases since density of states increases. Due to electron-hole symmetry in dispersion relation, the conductivity curve is quite symmetric with respect to Dirac point. Since the Fermi level lies at K, K’ points as in Fig. 2.3a), charge-neutral graphene (without tuning carrier density by gate voltage) should have zero carrier density and thus show minimum conductance. . The Fermi level changes with back gate as positive gate voltage increase Fermi level and induces electron carriers in graphene and vice versa. Due to inevitable environmental doping, the Dirac point V_D typically shows small shift from zero gate voltage as in Fig. 2.3 b) ($V_D \neq 0$) and the value of V_D changes from device to device.

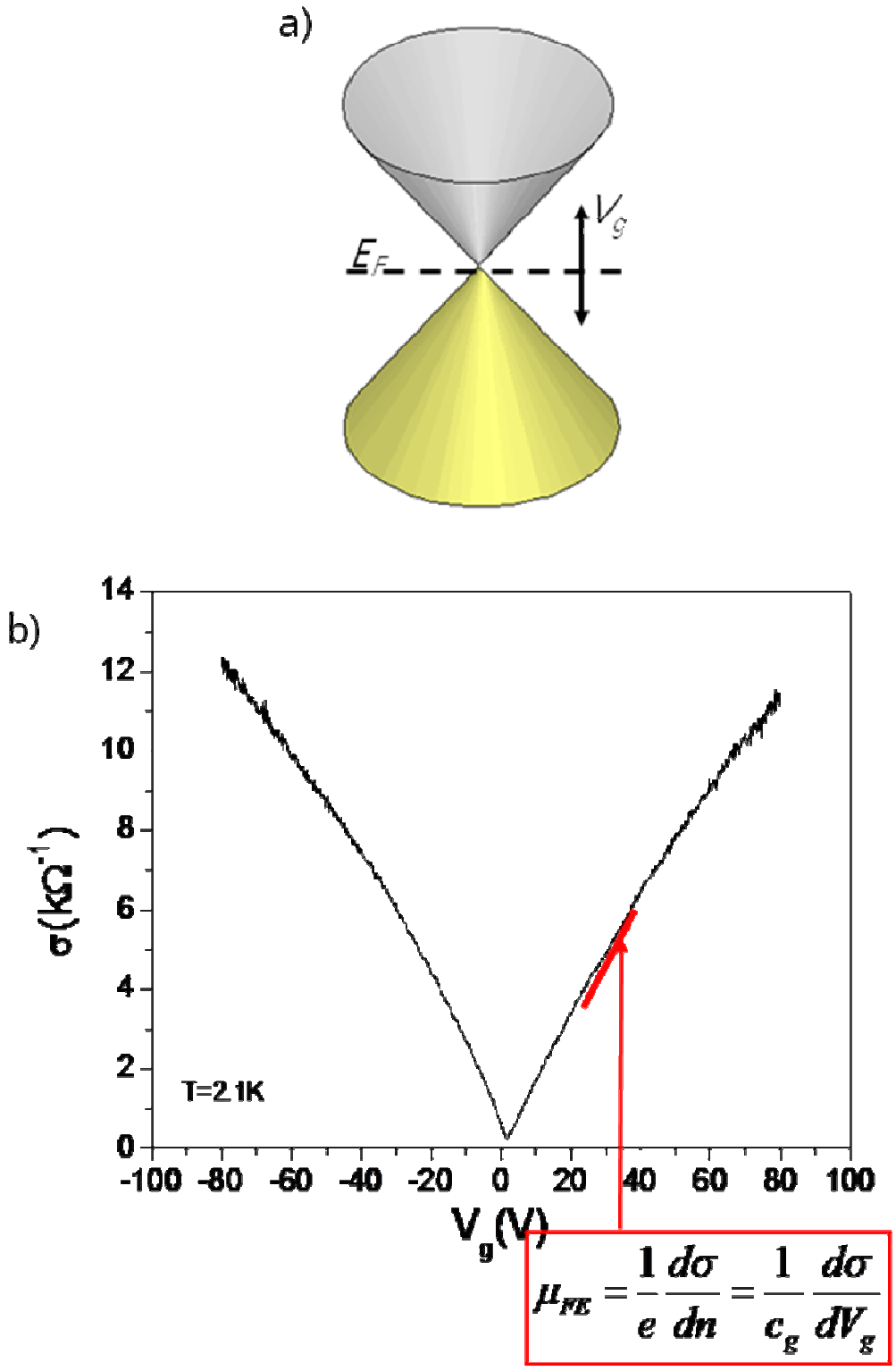

Fig.2.3 a) Low energy dispersion of single layer graphene illustrating the effect of tuning gate voltage. b) Conductivity of graphene σ as a function of gate voltage at a temperature T = 2K.

Fig. 2.3b) shows the conductivity $\sigma_{xx}$of a graphene sample as a function of gate voltage measured at temperature T = 2K. As I induce more charge (electron or hole) carriers in graphene by increasing $|\Delta V_g|=|V_g-V_D|$, the conductance in graphene increases since density of states increases. Due to electron-hole symmetry in dispersion relation, the conductivity curve is quite symmetric with respect to Dirac point, V_D. Even though the density of states at the Dirac point is zero, there is finite minimum conductivity which is observed by several groups to fall in the range ~ 4-10 e^2/h[1, 3]. ; the origin of this finite minimum conductivity will be discussed in more detail in Chapter 4.. The field effect mobility calculated by

$$\mu_{FE} = \frac{1}{e}\frac{d\sigma}{dn} = \frac{1}{c_g}\frac{d\sigma}{dV_g} \qquad (2.1)$$

ranges from 8,000 ~ 20,000 cm^2/Vs in single layer graphene[1, 3, 28].

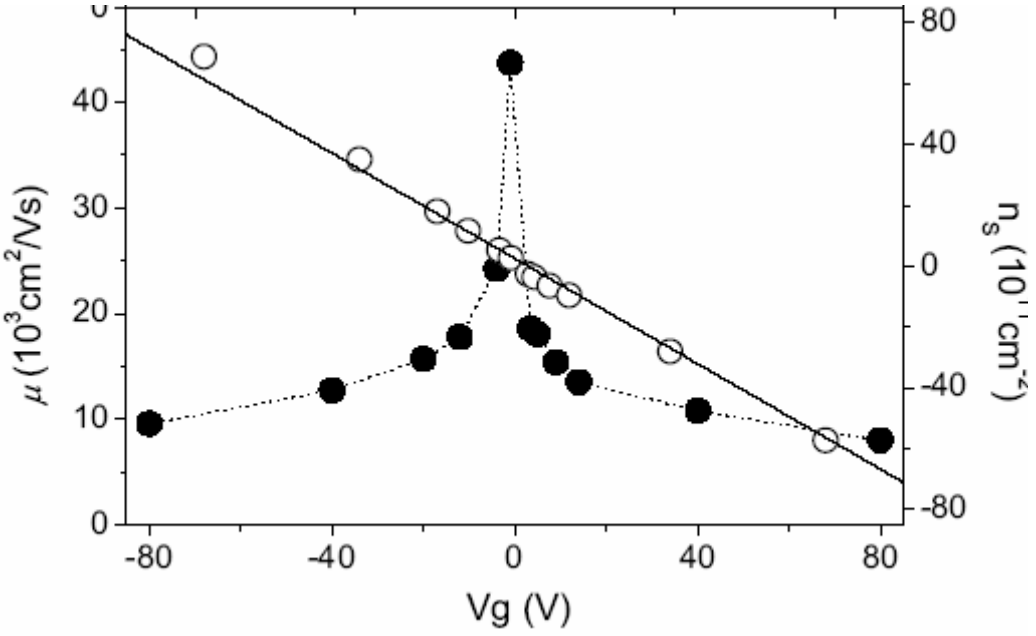

Fig.2.4 Charge carrier density (open circle) and mobility (filled circle) of graphene as a function of gate voltage (Figure from Ref. [3]).

As in Fig. 2.4[3], Hall measurement shows change of sign of carrier density upon V_g passing through Dirac point V_D, which clearly indicates that Fermi level E_F is passing through charge neutrality point.

2.3. Graphene Characterization; Single layer and Bilayer Graphene

In addition to identification by optical contrast, I used two other methods to differentiate single layer and bilayer graphene; the anomalous quantum hall effect[1, 3, 28] and Raman spectroscopy[43]. Either of these measurements enables us to distinguish between single layer and bilayer graphene since they show qualitatively different behaviors.

2.3.1 Anomalous Quantum Hall Effect

One of the most important discoveries in condensed matter experimental physics in the 1980s was the quantum Hall effect by von Klitzing et al[44]. The quantum Hall effect is fascinating in that it enables us to measure hall resistance in quantized units of $h/2e^2$ with an accuracy of one parts per million[reference]. This high accuracy results from a perfect suppression of back scattering in the quantum Hall regime since electron states carrying current in one direction are localized on one edge and the other states carrying current in opposite direction are localized on opposite edge. In a large enough sample, these two states on opposite edges cannot overlap and thus back scattering is truly suppressed over a long distance even with impurities present in the sample.

High mobility graphene samples also enables us to observe the quantum Hall effect as in Fig 2.5b)[1, 3, 28]. To measure quantum Hall effect in graphene, I usually fixed the magnetic field *B* at a high value (in Fig.2.5b) B ~ 8 T), and sweep gate voltage to tune E_F. At high magnetic field, quasi-discrete Landau levels are formed in graphene. The density of states of these Landau levels are shown in Fig.2.5a). As Fermi level moves from one Landau level to next one, R_{xx} shows an oscillation. When the Fermi level lies between successive Landau levels, σ_{xy} shows plateaus while R_{xx} becomes zero due to ballistic transport of edge states as in Fig. 2.5b). As I sweep gate voltage from negative to positive, carriers from electrons to holes successively fill Landau levels and σ_{xy} changes its sign. The most striking fact is that the quantized quantum Hall conductivity in graphene shows different values from that in conventional 2DEG. In conventional 2DEG, the quantized Hall conductivity is

$$\sigma_{xy} = \pm gn\frac{e^2}{h} \qquad (2.2)$$

where *g* is the total degeneracy (valley degeneracy times spin degeneracy), and *n* is an integer. The factor *gn* is called the "filling factor" and indicates the number of filled Landau levels, or number of conducting edge modes. In contrast, in single layer graphene the filling factor is not g n , but g (n+1/2), which is half integer shifted as in Fig.2.5b). Thus, the quantized Hall conductivity is observed to be

$$\sigma_{xy} = \pm g\left(n+\frac{1}{2}\right)\frac{e^2}{h} \qquad (2.3)$$

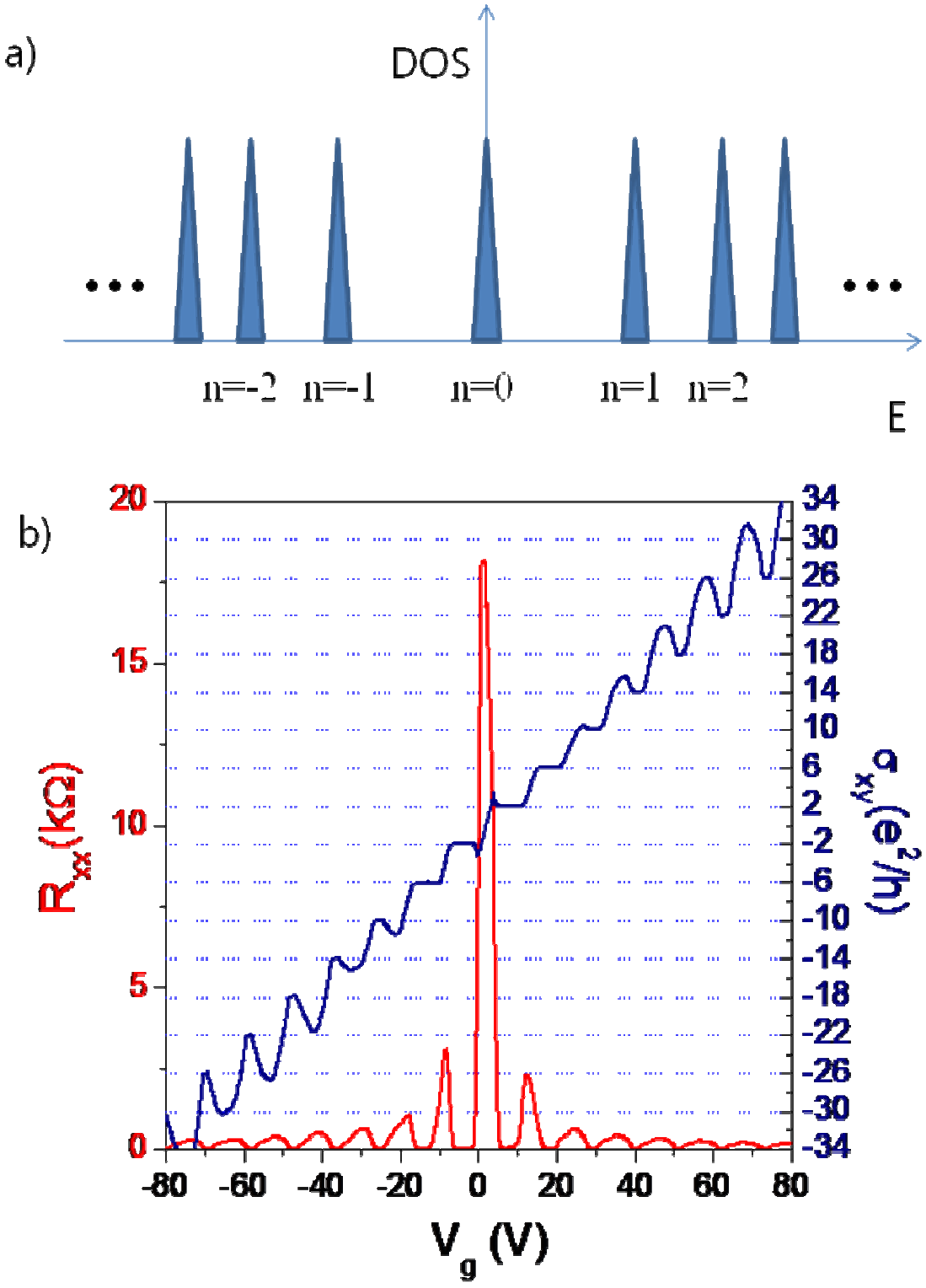

Fig.2.5 half integer quantum Hall effect in single layer graphene measured at T=2.3K and B=7.94T.

The half-integer in filling factor originates from π Berry phase in graphene[1, 3]. Degeneracy g in graphene corresponds to 4 since there are is spin degeneracy of 2, and 2 “valleys” (K and K’).

On the other hand, in bilayer graphene, the filling factor is g n as seen in Fig. 2.6 similar to conventional 2DEG since Berry phase of bilayer graphene is also 2π [20]. Thus, the quantized Hall conductivity in bilayer graphene is given as equation 2.2. The degeneracy g is 8 at zero energy and 4 at all other landau levels.

Since the quantized hall conductivities of single layer and bilayer graphene shows different filling factors, quantum hall measurement can be used as a characterization tool to distinguish between single and bilayer graphene. In fact, I measured quantum hall effect to confirm number of graphene layers in Fabry-Perot interference experiment, which will be discussed in next chapter.

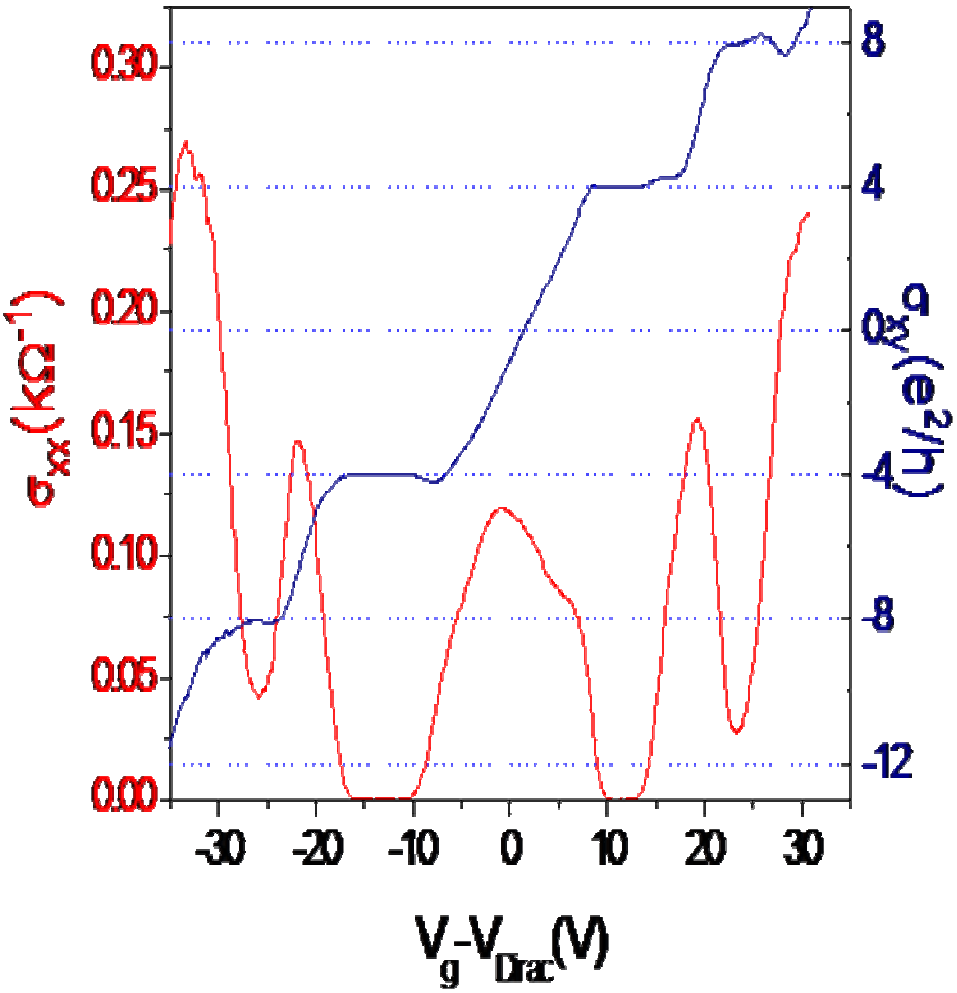

Fig.2.6 Integer quantum Hall effect in bilayer graphene measured at T=1.35K and B=9T

2.3.2 Raman Spectra of Graphene

Raman scattering involves inelastic scattering processes of photons. Generally speaking, Raman scattering occurs in the following way in solids. First, when a laser beam is shone on a sample, an electron in the sample is excited from valence to conduction band by absorbing an incident photon. Second, the excited electron is scattered by emitting or absorbing phonons. Third, the electron relaxes to valence band by emitting a photon. Since the scattered photon loses energy to phonon, it has energy smaller than the incident photon by phonon energy. The Raman spectra I observe is the intensity of the scattered photons as a function of frequency downshift (energy loss).

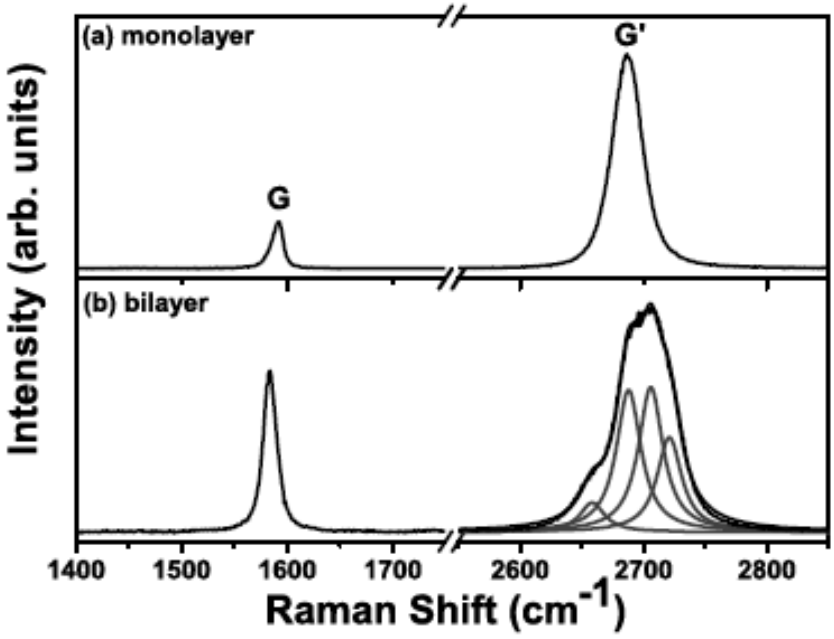

Fig. 2.7 Raman Spectrum of a) single layer graphene and b) bilayer graphene. (Figure from Ref,[45])

Raman spectroscopy serves as a strong tool to characterize number of layers in graphene[43, 45]. Here, I will focus on single and bilayer graphene. As in Fig. 2.7, there are two most prominent peaks in the Raman spectrum of graphene, the G peak near 1600cm^{-1} and the G' (or 2D) peak near 2700cm^{-1}. Ferrari et al, showed that the G' peak in Raman spectrum can be used to distinguish between single and bilayer graphene. As in Fig. 2.7, while the G' peak of single layer graphene is fit to one Lorentz peak, G' peak of bilayer graphene is fit to four Lorentz peaks.

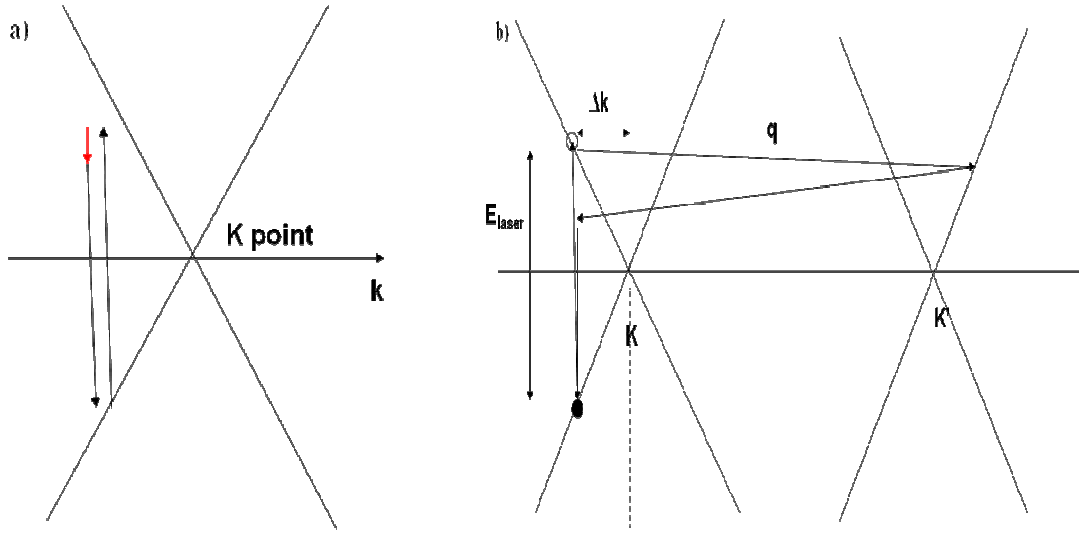

Fig. 2.8. a) First Order(G peak) b) second order(G' peak) Raman scattering process in single layer graphene

As shown in Fig. 2.8 a), Raman scattering for the G peak in graphene involves one optical phonon at q = 0, and thus it is called first-order Raman scattering. On the other hand, Raman scattering for the G' peak involves two optical phonons with opposite momentum ($q \neq 0$) as shown in Fig. 2.8b). During this second order process, an electron is excited by a photon at Δk state, scatters to Δk+q state by a phonon q, scatters back to Δk state by a phonon –q, and then emits a photon by

recombining with a hole at Δk state. Since these two phonons have the same momenta and hence the same frequencies in single layer graphene, they produce only one Lorentz component in the G' peak.

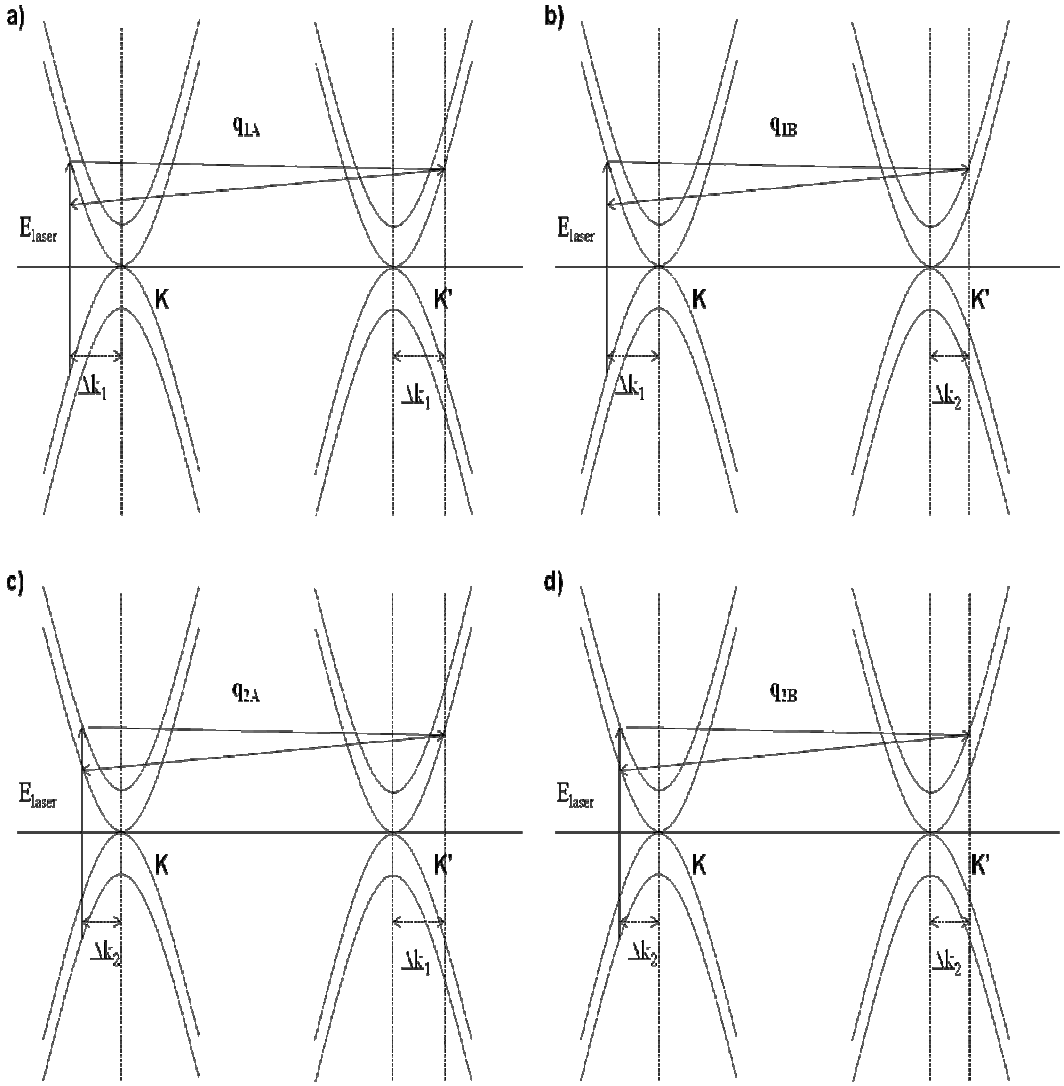

Fig. 2.9 Raman scattering process for G' peak in bilayer graphene

Since there are two conduction and two valence bands in Bernal stacked bilayer graphene, there are four possible transitions of electrons from valence to conduction band when sample is illuminated by laser beam. Density functional theory

shows that incident photons couple more strongly with two transitions shown in Fig. 2.9[43]. Thus, there are four possible intervalley scattering processes involving phonons of four momenta $q_{1A,}$ $q_{1B,}$ $q_{2A,}$ q_{2B} as in Fig. 2.9a)~d). The zone-boundary phonon is strongly dispersive due to a Kohn anomaly, hence the four allowed scattering momenta have discernibly different frequencies, and result in four Lorentz components in the G' peak of bilayer graphene as shown in Fig. 2.7b).

In conclusion, the lineshape of the G' Raman peak in graphene can distinguish whether the sample is single or bilayer graphene.

Chapter 3. Massless and Massive Particle-in-a-box States In Single and Bilayer Graphene

The problem of a wavelike particle confined to a hard-walled box is one of the most basic problems in quantum mechanics. The spectra of the particle-in-a-box are strikingly different for massive and massless particles: massless particles (e.g. photons) have energies which depend linearly on quantum number, while the energies of massive particles (e.g. free electrons) depend quadratically on quantum number. For Fermions in two dimensions (2d), this leads to a density of single-particle states $D \equiv dn/dE$, where E is the particle energy and n the particle density, which varies as the square root of particle density, i.e. $D(n) \sim n^{1/2}$, for massless particles, and is independent of particle density for massive particles, i.e. $D(n) \sim$ constant.

In this chapter, I will demonstrate this basic physics using electrons in single- and bilayer graphene as examples of massless and massive 2d Fermions, respectively. I show that mesoscopic, ballistic[46] single-layer[2, 47] and bi-layer[23, 48] metal-graphene-metal devices act as Fabry-Perot cavities for electrons confined between the atomically-sharp partially-reflective metal leads. Electronic conduction occurs through resonant states of the Fabry-Pérot cavity, which are exactly analogous to the particle-in-a-box states of an electron confined by perfectly reflective walls. $D(n)$ is measured, and the expected dependences on particle number are verified: $D \sim n^{1/2}$ for massless particles in single-layer graphene, and $D \sim$ constant for massive particles in bi-layer graphene. $D(n)$ is used to extract the single constants in the dispersion relations: the Fermi velocity $v_F = 1.09 \times 10^6$ m/s for massless particles in single-layer

graphene[2, 47], and the effective mass $m^* = 0.032\ m_e$, where m_e is the electron mass, for massive particles in bilayer graphene[23, 49] in excellent agreement with theoretical expectations[48-52] and other experimental results[2, 47, 53-55]. The results discussed in this chapter are published in *Nano Research*[24].

3.1. Density of States in Single and Bilayer Graphene

I first review the results of the two-dimension particle-in-a-box problem. Figs. 3.1A and 3.1B illustrate the massless and massive dispersion relations respectively. As shown in Chapter 1, the low energy dispersions for massless and massive Dirac Fermions in single and bilayer graphenes are:

$$E = \eta v_F |\boldsymbol{k}| \text{ (massless)} \quad (3.1a) \qquad E = \frac{\eta^2 k^2}{2m^*} \text{ (massive)} \quad (3.1b)$$

where $\hbar = h/2\pi$, and h is Planck's constant; each dispersion relation is characterized by a single parameter, m^* for the massive dispersion, and v_F for the massless dispersion. For particles confined to a 2-dimensional box of width W and length L the hard-wall boundary condition quantizes the wavevector $\mathbf{k} = (k_x, k_y) = \left(p\frac{\pi}{L}, q\frac{\pi}{W} \right)$ resulting in two positive quantum numbers p, q. Figs. 3.1C and 1D illustrate this quantization, where each point represents an allowed wavevector. Then the energies in terms of quantum numbers are given by the familiar relations $E = \mathrm{h} v_F \pi \sqrt{\left(\frac{p}{W}\right)^2 + \left(\frac{q}{L}\right)^2}$ (massless) and $E = \frac{h^2}{8m}\left\{\left(\frac{p}{W}\right)^2 + \left(\frac{q}{L}\right)^2\right\}$ (massive). For Fermions at zero temperature, the occupancy of particle-in-a-box state will be the degeneracy of individual states g for state of energy $E < E_F$ (Fermi energy)

and zero for states $E > E_F$. The number of states with $E < E_F$ is given by $N = gk_F^2 WL/4\pi$, where $k_F \equiv k(E_F)$ is the Fermi wavevector. Figs. 3.1C and 3.1D illustrate the occupied states included for equally-spaced values of E_F, and Figs. 3.1E and 3.1F show the energies of the particle-in-a-box states as a function of particle number N for massless and massive 2d Fermions respectively. The linear and square-root dependences of $E(N)$ for massless and massive 2d Fermions respectively are evident in Figs. 3.1E and 3.1F. Using the areal density of particles $n = \frac{N}{WL} = \frac{gk_F^2}{4\pi}$ I then have the following relations for the dependences of the Fermi energy E_F and density of states D on density:

$$E_F = \eta v_F \sqrt{\pi n} \text{ (massless) (3.2a)} \quad E_F = \frac{\pi \eta^2 n}{2m^*} \text{ (massive) (3.2b)}$$

$$D = \frac{1}{\eta v_F}\sqrt{\frac{gn}{\pi}} \text{ (massless) (3.3a)} \quad D = \frac{gm^*}{2\pi\eta^2} \text{ (massive) (3.3b)}$$

Thus the measurement of D as a function of n distinguishes massive and massless particles, and (given knowledge of the degeneracy g) also determines the constants of the dispersion relations v_F and m^*.

Single and bilayer graphene may be used to realize the dispersion relations in Equations 3.3a and 3.3b as follows. Single layer graphene is well-described by a tight-binding model considering only π orbitals at each atomic site as described in Chapter 1. At zero doping, the π and π* bands meet at two points in the Brillouin zone with wavevector **K**. This crossing is preserved as long as the two atoms A and B in the unit cell are equivalent. Taking $E(\mathbf{K}) = 0$, and measuring k away from the **K**

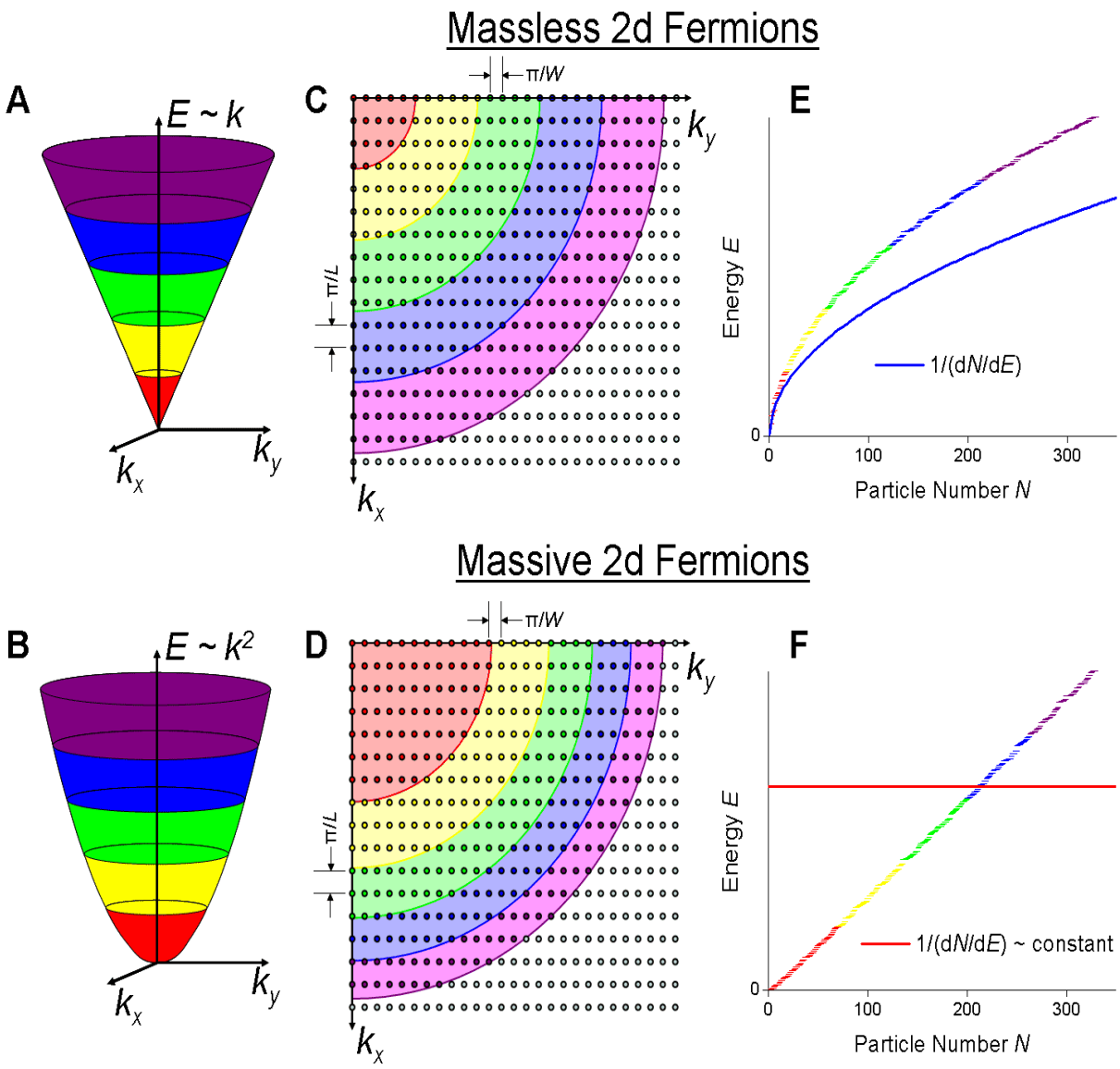

Fig. 3.1. (A) Massless dispersion and (B) massive dispersion relations in two dimensions. (C-D) Allowed wavenumbers for particle in a box of aspect ratio W/L = 1.6. Solid lines are contours of equal energy for massless dispersion relation (C) and massive dispersion relation (D). (E-F) Particle energy as a function of particle number in a box with W/L = 1.6 for massless dispersion relation (E) and for massive dispersion relation (F).

point, the band structure is well-approximated by Eqn. 1a, with $v_F = \left(\sqrt{3}/2\right)a\gamma_0/\eta \approx$ 1.0 x 10^6 m/s where a = 2.46 Å is the graphene lattice constant and $\gamma_0 \approx 3.16$ eV[56] is the nearest-neighbor hopping parameter. In Bernal-stacked bi-layer graphene[23,

48-49, 51-52], atom A in one layer is stacked above atom B' in the 2nd layer, and this A-B' coupling breaks the AB equivalency of the graphene unit cell and results in two bands which may be approximated as hyperbolic:

$E_{\pm}(k) = \pm\left[\sqrt{(\eta v_F k)^2 + \frac{\gamma_1^2}{4}} - \frac{\gamma_1}{2}\right]$ [49], where $\gamma_1 \approx 0.4$ eV[57] is the inter-layer (A-B') hopping parameter. At $k = 0$ the effective mass is given by $m^* = \gamma_1 / 2v_F^2 \approx 0.03\, m_e$. In both single- and bilayer graphene the degeneracy $g = 4$, due to the two-fold spin degeneracy and the two-fold valley degeneracy (presence of two **K** points).

3.2 Sample Preparation and Characterization

I now discuss the graphene samples used in this study. As described in Chapter 2, I mechanically exfoliated Kish graphite on 300nm SiO_2/Si substrates to obtain single and bilayer graphene[2, 23, 47]. Single layer graphene is more transparent than two or more layer graphene under optical microscope as seen in Fig. 3.2A and 3.2B. After locating graphene flakes, Cr/Au(5nm/50nm) were thermally deposited for electrical contacts. The channel lengths L for Fabry-Perot interference measurement are 200nm - 300nm and measured by scanning electron microscope. The maximum field-effect mobilities at low temperature estimated from the four - probe resistivity of the adjacent graphene sections are 15,000 cm^2/Vs and 4,000 cm^2/Vs for single- and bilayer graphene respectively.

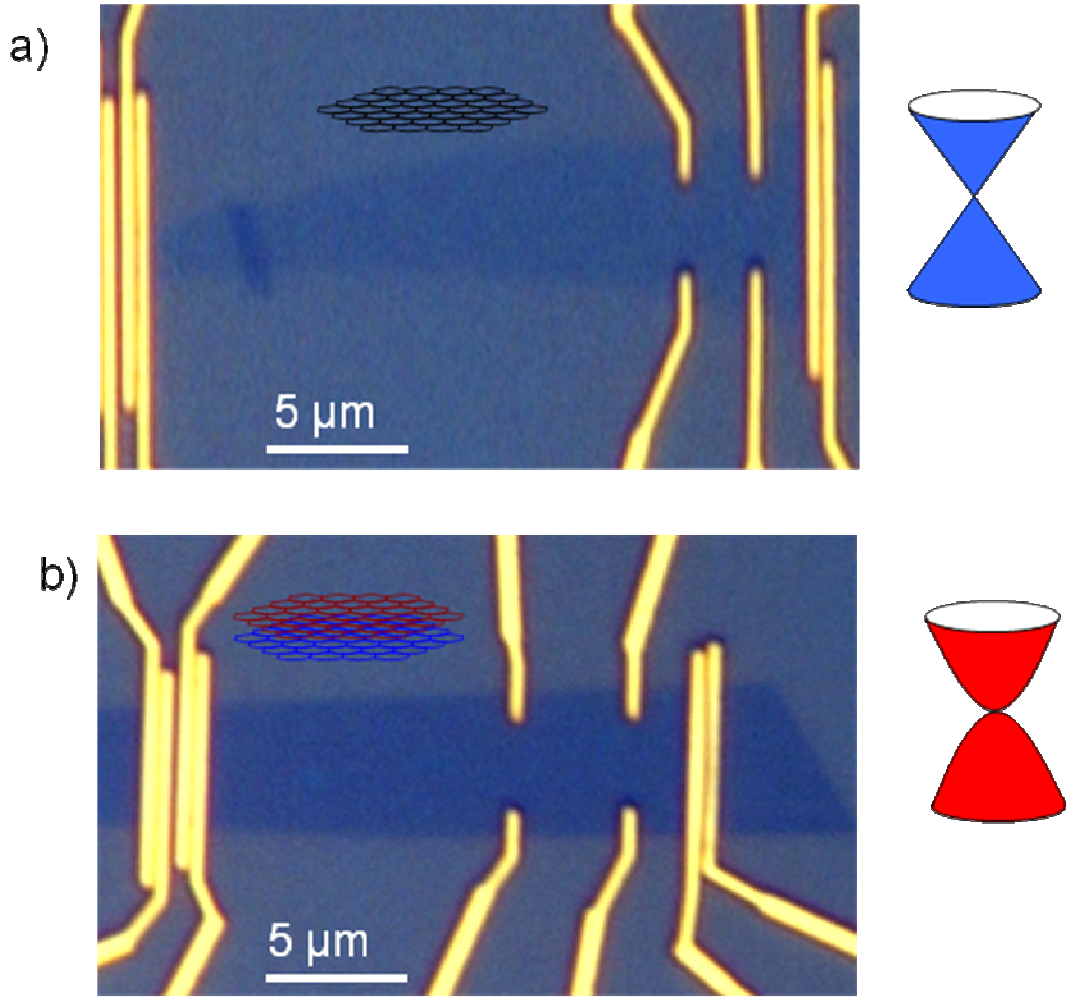

Fig. 3.2. Optical micrographs of single-layer graphene device (a) and bilayer graphene device (b).

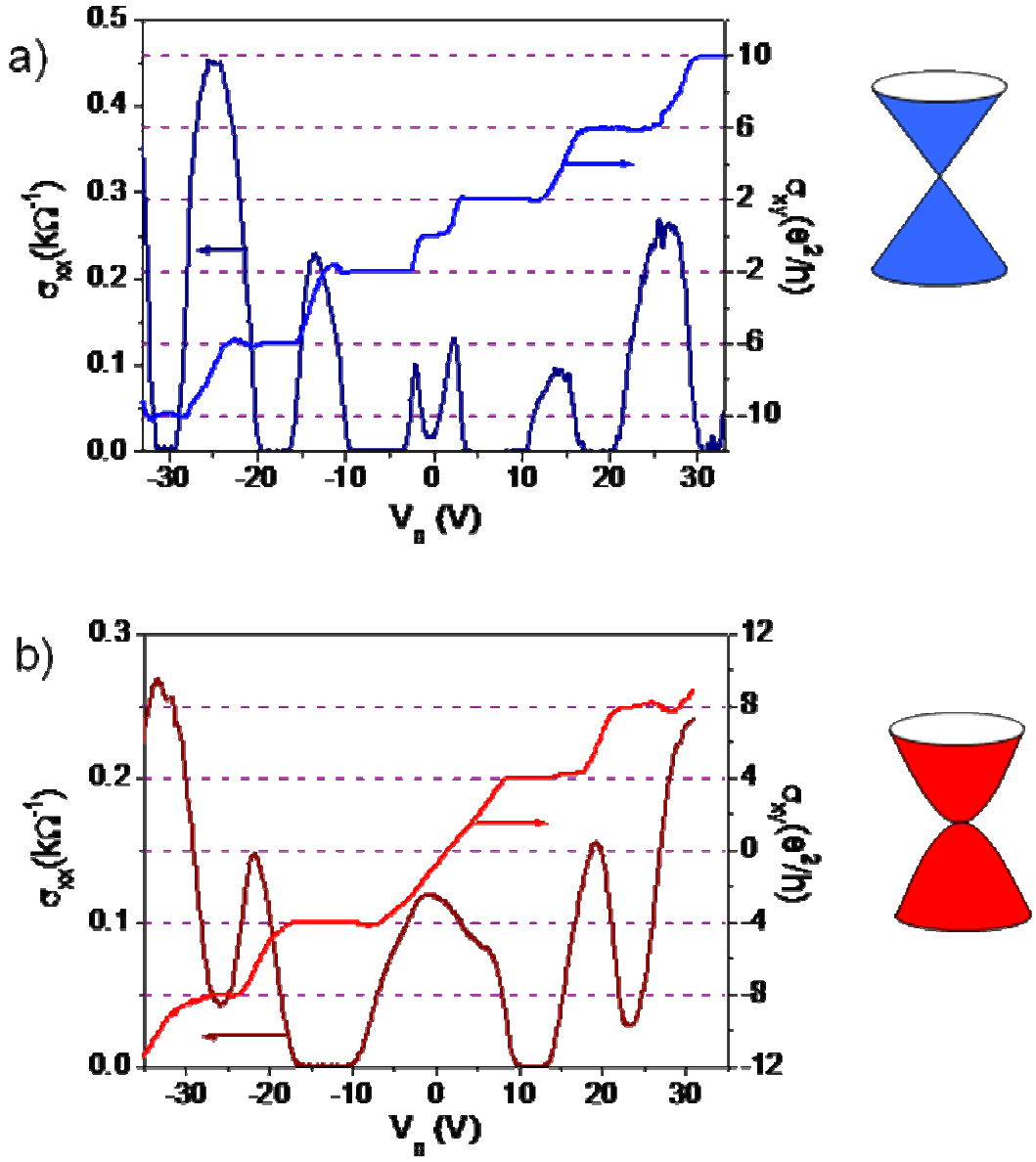

Fig. 3.3 Longitudinal and Hall conductivity as a function of gate voltage at magnetic field of 9 T and temperature of 1.3 K for single-layer graphene device (a) and bilayer graphene device (b).

Figs. 3.2a) and 3.2b) show completed single- and bilayer graphene devices respectively. Electrodes are patterned on each graphene flakes to form a large-area Hall-bar arrangement for characterizing the longitudinal and Hall conductivities (σ_{xx} and σ_{xy}) of the sample. In addition, pairs of closely-spaced (150-300 nm) electrodes act as Fabry-Pérot cavities on the same sample.

Figs. 3.3a) and 3.3b) show σ_{xx} and σ_{xy} for the single- and bi-layer graphene devices shown in Figures 3.1a) and 3.1b), respectively, measured in high magnetic field (9 T) and as a function of back-gate voltage V_g, which controls the carrier density $n = c_g V_g/e$, where $c_g = 1.1 \times 10^{-8}$ F/m, and e is the electronic charge. The quantized Hall effect (QHE) is evident as plateaux with $\sigma_{xy} = \nu e^2/h$, and corresponding minima in σ_{xx}. As discussed in Chapter 2, Berry's phases of π and 2π lead to QHE in single- and bi-layer graphene at filling factors $\nu = 4(i+1/2)$ and $4(i+1)$, where i is an integer[2, 23, 47], thus our observations of the half-integer QHE, and full-integer QHE with the missing $\nu = 0$ plateau, confirm the identification of these samples as single- and bi-layer graphene respectively.

Figs. 3.4a) and 3.4b) show the two-probe conductances as a function of gate voltage $G(V_g)$ for Fabry-Pérot cavities on the single- and bi-layer devices, respectively, at zero magnetic field. I shift the curves horizontally by an amount V_D which I identify as the gate voltage at which the Fermi level lies closest to the Dirac point. The conductance rises away from $V_g - V_D = 0$ as observed by previously[2, 23, 47]. Small reproducible fluctuations of the conductance with magnitude of order e^2/h can be seen (see insets to Figs. 3.4a) and 3.4b)); these fluctuations are not universal

conductance fluctuations (UCF) but, as argued below, result from the interference of ballistic electron waves in the Fabry-Pérot cavity[46].

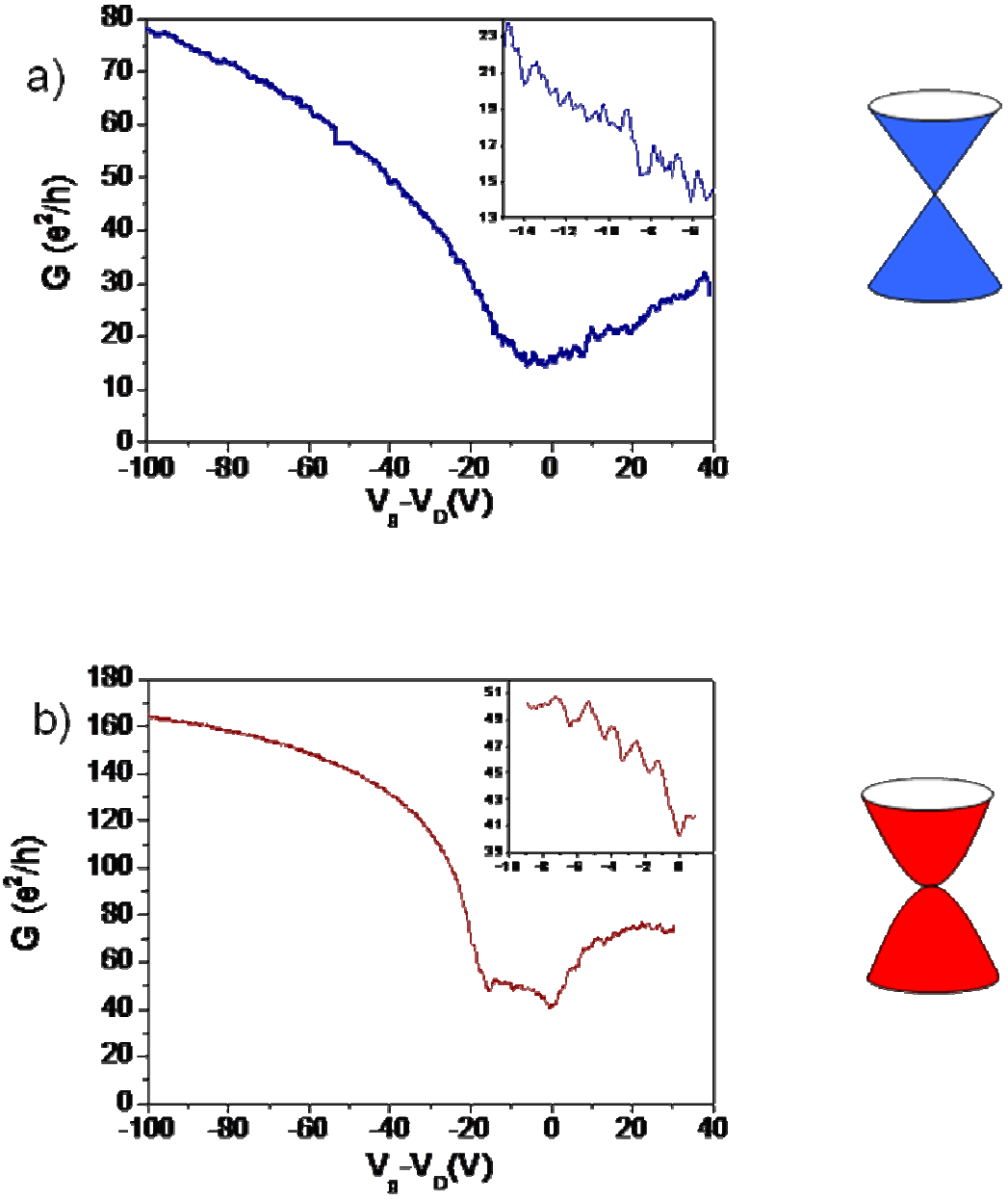

Fig. 3.4 Two-probe conductance as a function of gate voltage at zero magnetic field and temperature of 1.3 K for single-layer graphene device (a) and bilayer graphene device (b)

3.3 Fabry-Pérot Interference Measurement and Discussion

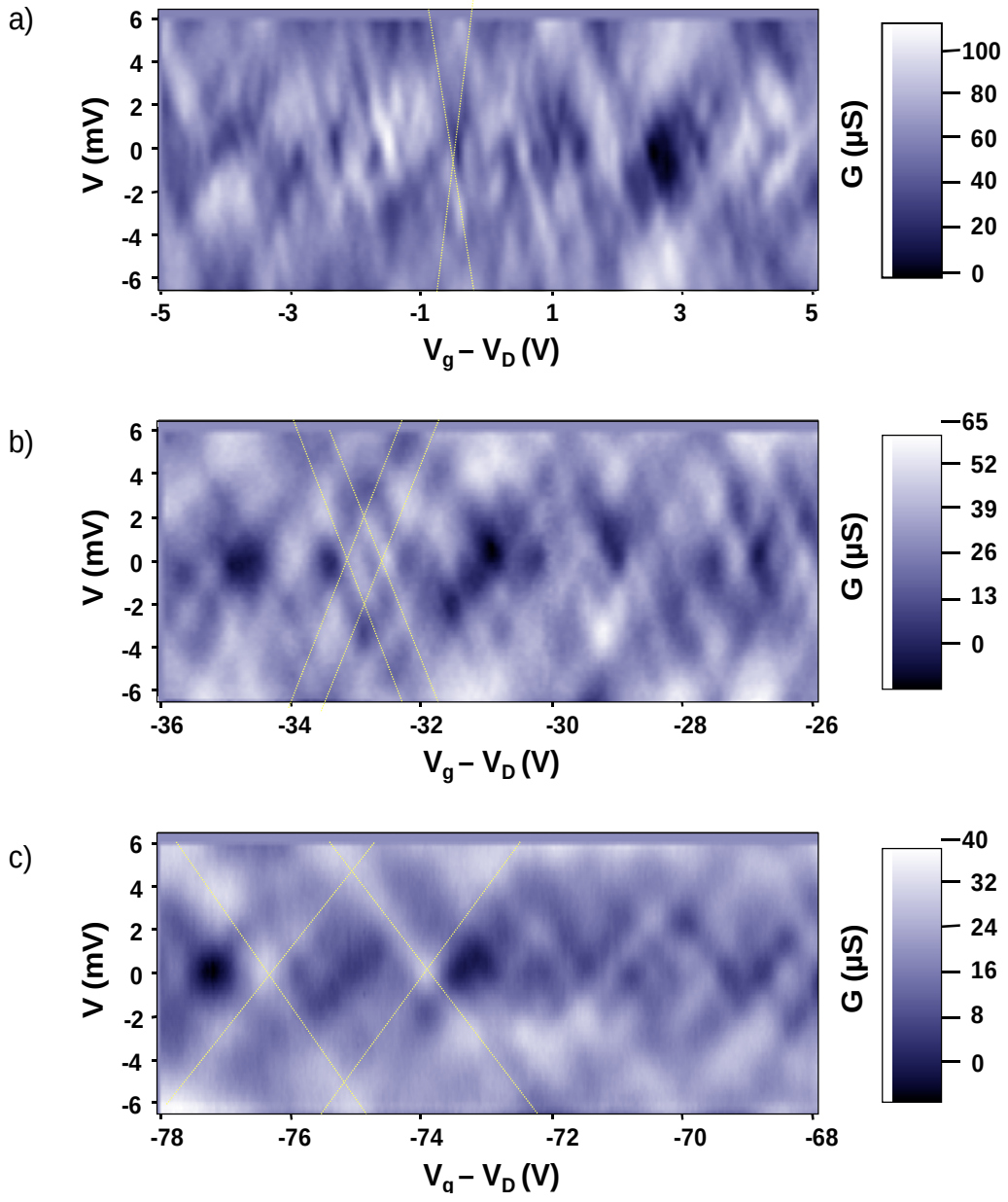

Fig. 3.5. Color-scale two-dimensional plots of differential conductance $G = dI/dV$ as a function of bias voltage V and gate voltage V_g measured in single graphene at temperature T = 1.3K. A smooth background conductance was subtracted to enhance the patterns. The sample dimensions are 1.5μm(W) x 0.3μm(L). Yellow lines illustrate the slope of the Fabry-Pérot resonances

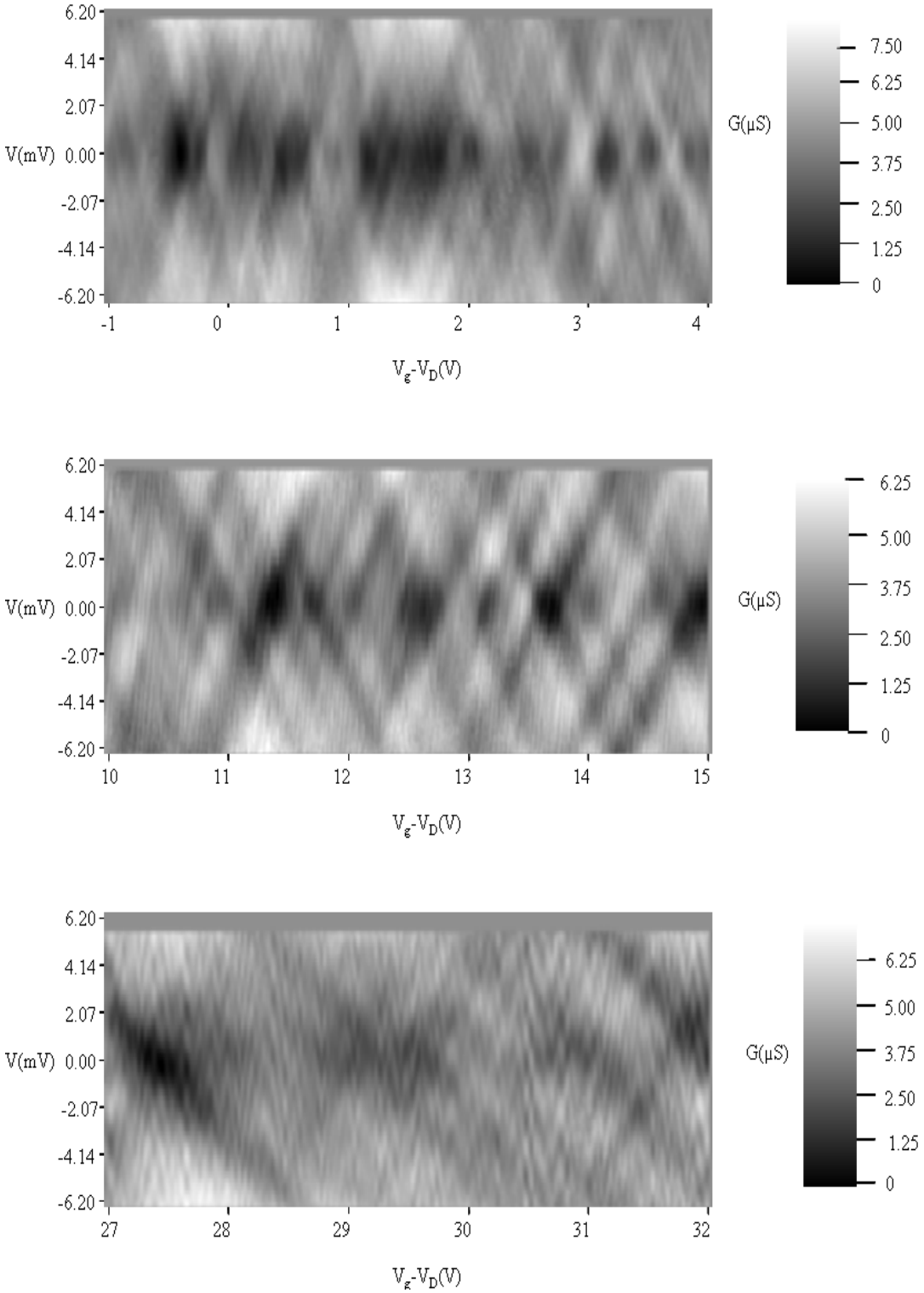

Fig. 3.6 Fabry-Perot interference data (similar to Fig. 3.5) taken on an additional single-layer graphene sample with ferromagnetic electrodes, of dimensions 350nm(*W*) x 200nm(*L*). Data were taken at temperature T = 1.3K. A smooth background conductance was subtracted to enhance the patterns.

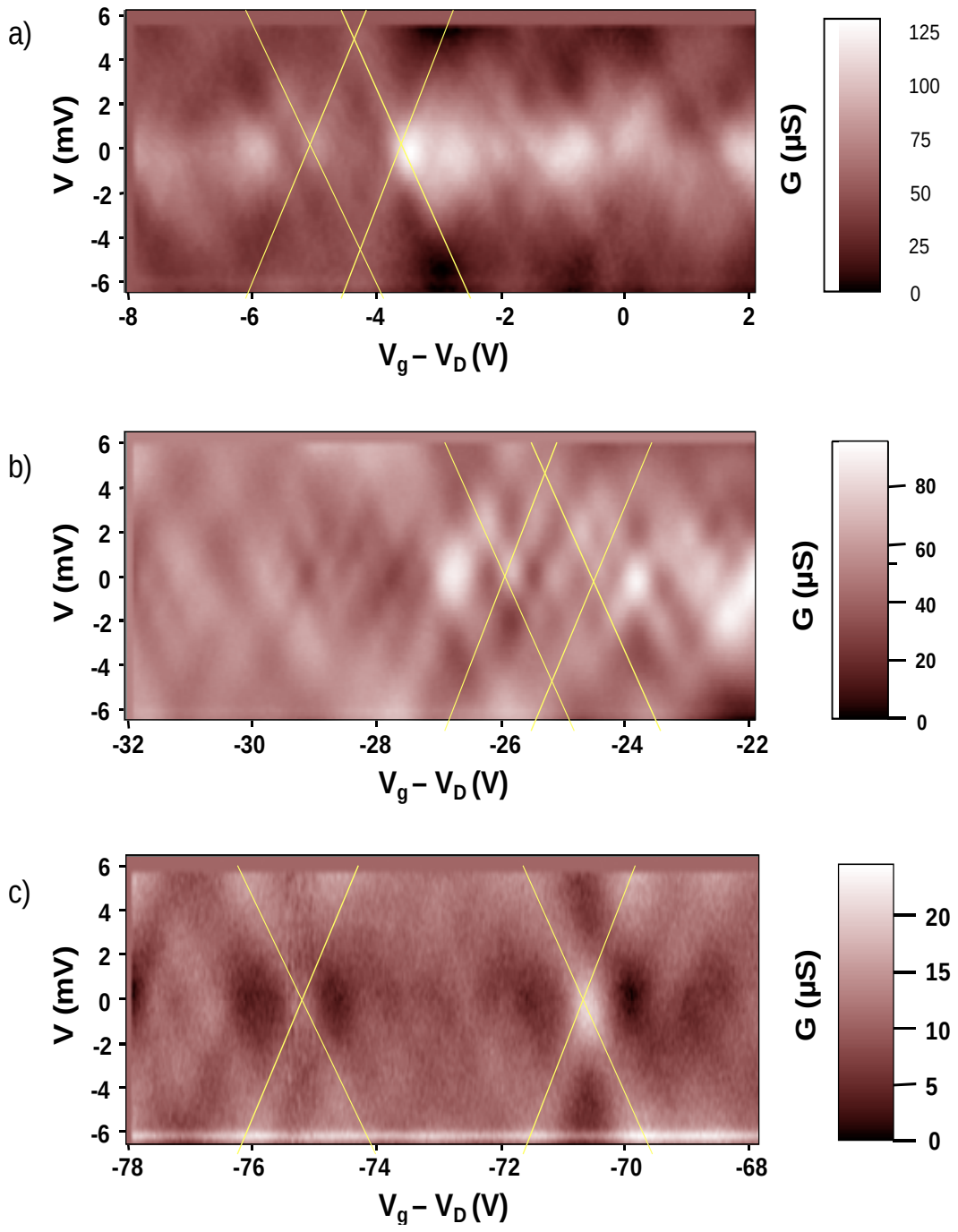

Fig. 3.7. Color-scale two-dimensional plots of differential conductance $G = dI/dV$ as a function of bias voltage V and gate voltage V_g measured in single (A-C) and bilayer (D-F) graphene at temperature T = 1.3K. A smooth background conductance was subtracted to enhance the patterns. The sample dimensions are 1.5μm(W) x 0.3μm(L) for single layer graphene and 4.3μm(W) x 0.2μm(L) for bilayer graphene. Yellow lines illustrate the slope of the Fabry-Pérot resonances

Figs 3.5 ~ 3.7 show color-scale maps of the differential conductance dI/dV as a function of bias voltage V applied between the two electrical contacts and gate voltage V_g for the single- and bi-layer devices shown in Fig 3.2. A pattern of diagonal lines of increased conductance is evident; this pattern is the signature of Fabry-Pérot interference in a mesoscopic device[46, 58]. Neighboring diagonal lines have similar slopes, and diagonal line of similar positive and negative slope are found in each V_g region. Each individual diagonal line results from the enhancement in conductance when a particle-in-a-box resonance, or a group of constructively-interfering resonances, is aligned with the source electrode (+V) or drain electrode (-V); the symmetry about $V = 0$ reflects the source-drain symmetry of the device. Note that the pattern is inconsistent with Coulomb blockade; there are no diamond-shaped low conductance regions around $V = 0$, and the overall conductance > e^2/h excludes Coulomb blockade.

Resonant transmission through a Fabry-Pérot cavity has been reported previously for carbon nanotubes (CNTs)[58-59] and graphene [46]. In the case of CNTs, there is a single path length L connecting the electrodes, and the resonances are evenly spaced in V and V_g. In graphene [46], the resonances are randomly spaced, which may result from a spread of path lengths due to non-parallel electrodes or electron paths which are not perpendicular to the electrode-graphene interfaces. However, important information can be gained by analyzing the *slope* $\Delta V/\Delta V_g$ of the resonant lines in Fig. 3.5~3.7. Briefly, the slope measures the change in energy $\Delta E = e\Delta V/2$ (the factor of two results from the potentials $+\Delta V/2$ and $-\Delta V/2$ applied to the two electrodes relative to the graphene in a ballistic device) of the resonance as the

particle number $dn = c_g \Delta V_g / e$ is changed. The slope is then equal to $\Delta V / \Delta V_g = (2c_g/e^2)\Delta E/\Delta n = (2c_g/e^2)D^{-1}$; i.e. the slope is inversely proportional to the density of states (see Methods for a more rigorous derivation of the same result). From Eqns. 3.3a and 3.3b above, I expect that $\Delta V/\Delta V_g \sim n^{-1/2} \sim |V_g - V_D|^{-1/2}$ for the single-layer (massless dispersion) sample, and $\Delta V/\Delta V_g \sim$ *constant* for the bi-layer (massive dispersion) sample. Figs. 3.5 and 3.6 show that the slope indeed varies significantly with gate voltage (electron density) for the single-layer graphene sample, with the highest slope occurring near $V_g - V_D = 0$. The slope is nearly constant in the bi-layer graphene sample as seen in Fig 3.7.

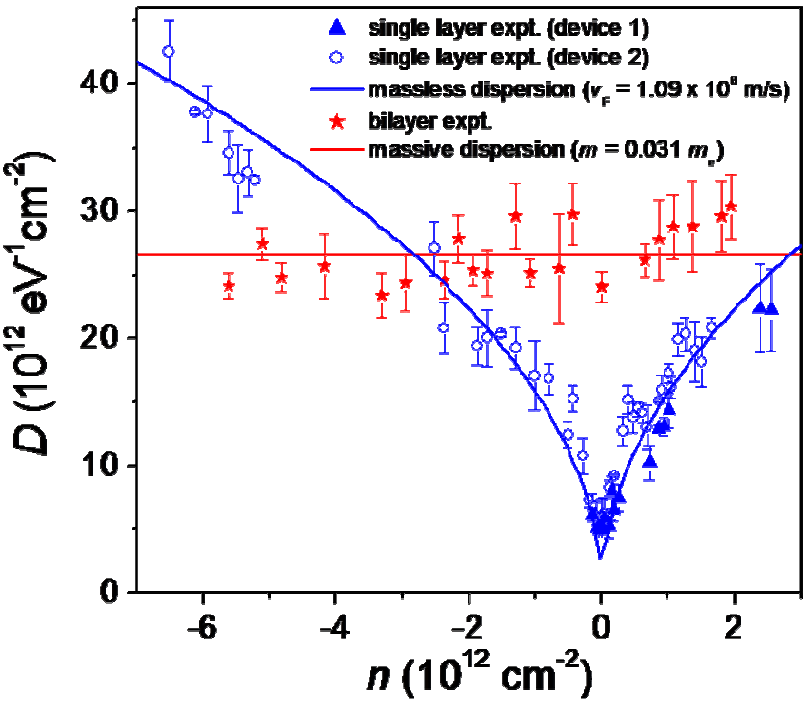

Fig. 3.8. Density of states of single-layer graphene (blue symbols; data from two devices shown) and bilayer graphene (red symbols, data from one device shown) as a function of particle density. Solid lines are fits to Eqn. 3a (blue) with v_F = 1.09 x 10^6 m/s and Eqn. 3b (red) with m^* = 0.032 m_e.

Fig. 3.8 plots the density of states $D = (e^2/2c_g)(\Delta V/\Delta V_g)^{-1}$ for the single- and bi-layer graphene samples extracted from Figs. 3.5 ~3.7 as a function of electron density $n = c_g(V_g - V_D)/e$. Solid lines are fits to Eqns. 3a and 3b for the single-layer and bi-layer data respectively. The expected dependences on particle number are verified: $D \sim n^{1/2}$ for massless particles in single-layer graphene (Eqn. 3.3a), and $D \sim$ *constant* for massive particles in bi-layer graphene (Eqn. 3.3b). Only a single fitting parameter is used in each fit, $v_F = (1.09 \pm 0.01) \times 10^6 m/s$ for massless particles in single-layer graphene and $m^* = (0.0315 \pm 0.0001) m_e$ for massive particles in bi-layer graphene. As discussed in detail below, the parameters are in excellent agreement with theoretical and other experimental results.

I now discuss the detailed dependence of the density of states on particle number in single- and bi-layer graphene, and the implications of the results for understanding the electronic structure of these materials. From the fit to Eqn. 3.3a in Fig.3.8, I determine a Fermi velocity for single-layer graphene of $v_F = (1.09 \pm 0.01) \times 10^6 m/s$. A tight-binding model of graphene[60] gives $v_F = \left(\sqrt{3}/2\right) a\gamma_0 / \eta \approx 1.0 \times 10^6$ m/s where $a = 2.46$ Å is the graphene lattice constant and $\gamma_0 \approx 3.16$ eV[56] is the nearest-neighbor hopping parameter. The inclusion of electron-electron interactions will renormalize the Fermi velocity slightly[50], and the slightly higher v_F observed here is consistent with other experiments on graphene[2, 47, 61-62].

The density of states in single-layer graphene remains finite as $n \rightarrow 0$ due to charge inhomogeneity caused by charged impurities near the graphene, as has been observed previously. The minimum density of states D on order 2×10^{12} $eV^{-1}cm^{-2}$

corresponds to a charge density n on order 10^{11} cm^{-2}, in agreement with theoretical[63] and experimental expectations[64-65] for the minimum charge density at the Dirac point in the presence of charged impurity disorder due to the SiO_2 substrate.

I now discuss bilayer graphene. From the fit to Eqn. 3.3b in Figure 3.8, I determine $m^* = 0.032m_e$. Assuming $v_F = 1.09 \times 10^6$ m/s I have $\gamma_1 = 0.40$ eV, in excellent agreement with the experimental values for graphite of 0.39 ± 0.01 eV [66] and with other experiments on bilayer graphene[53-54]. Because the bands are not strictly parabolic, the density of states should depend on particle density, increasing with increasing particle density. The hyperbolic nature of the bands becomes important for particle densities roughly greater than $\gamma_1^2/(4\pi\hbar^2 v_F^2) \approx 3 \times 10^{12}$ cm^{-2}. Experimentally, I see little variation in the density of states for particle densities up to 6×10^{12} cm^{-2}, indicating a wider range of validity of the parabolic spectrum than expected. I do not currently understand this discrepancy, but I note that electron-electron interactions should again be important, as was pointed out previously in the failure of the single-particle picture to quantitatively explain the cyclotron resonance spectrum in bilayer graphene[54].

3.4 Conclusion

In conclusion, I have probed the density of particle-in-a-box states as a function of particle number for massless 2d Fermions (single-layer graphene) and massive 2d Fermions (bi-layer graphene) in a phase-coherent measurement. The density of states varies as the square-root of particle number for massless 2d

Fermions, and is constant for massive 2d Fermions. The single parameters in the dispersion relations are extracted; the Fermi velocity $v_F = (1.09 \pm 0.01) \times 10^6 m/s$ for massless particles in single-layer graphene and $m^* = (0.0315 \pm 0.0001) m_e$ for massive particles in bi-layer graphene, in excellent agreement with theoretical expectations and other experimental observations.

Understanding coherent transport in graphene is an essential step to realize other interesting experiments in graphene such as a negative-index Veselago lens for electrons, Klein tunneling, and graphene superlattice[67-70]. Since this work, Fabry-Perot oscillations in metal-graphene-metal structures have been used to measure the *g*-factor of graphene electrons[71], and Fabry-Perot oscillations in graphene p-n-p junctions have been used to probe Klein tunneling physics[72-74].

Chapter. 4 Charge Transport and Inhomogeneity near the Minimum Conductivity Point in Graphene

In this chapter I use magnetotransport in graphene to study the nature of charge transport at the minimum conductivity point. I find a large magnetoresistance associated with the minimum conductivity point, which results from the presence of two carrier types (electrons and holes) within the sample. The functional form of the magnetoresistance does not follow a conventional two-fluid model typical of a semimetal, but instead is consistent with effective-medium-theory results for an inhomogenous spatial distribution of regions with equal charge carrier mobility but opposite charge carrier sign[25]. The results support the picture of charge inhomogeneity dominating the conductivity at the minimum conductivity point in graphene[26-27]. The results discussed in this chapter are published in *Physical Review B Rapid Communications*[75].

4.1 Minimum Conductivity and Electron-Hole Puddles in Graphene

One of the most fascinating aspects of graphene is that the quasiparticle Hamiltonian is identical to that of massless Dirac fermions, exhibiting a “Dirac point”

at which the density of states vanishes linearly without the presence of an energy gap as discussed in previous chapters. A striking aspect of experiments is that a finite conductivity is observed in graphene for all charge densities[1], with a minimum conductivity $\sigma_{xx,min}$ on order of $4e^2/h$ (but sometimes significantly smaller[76] or larger[26, 77]) occurring at the minimum conductivity point (MCP; in the absence of disorder, the MCP and Dirac point are identical, but in the presence of disorder, they are slightly different[26, 78]). The observation of a finite minimum conductivity has sparked significant theoretical interest. Models invoking only short-range scattering[79-80] give $\sigma_{xx,min} = 4e^2/\pi h$ only exactly at the MCP, and fail to reproduce the linear gate-voltage dependence of the conductivity $\sigma_{xx}(V_g)$. Other attempts[81] using the Landauer formalism also obtain $\sigma_{xx} \sim 4e^2/\pi h$ which depends weakly on aspect ratio, but such models are only expected to be valid in the ballistic limit for wide samples, $l < L < W$, where l is the mean free path, L the sample length, W the sample width. Some experiments have probed this limit[76], but many do not.

In this chapter, I will show that the conductivity near the MCP is dominated by charge disorder[78, 80, 82], i.e. spatially distinct regions, or "puddles" of electrons and holes. Because of the Klein paradox, the junctions between *p* and *n* regions in graphene are transparent to electrons, and the minimum conductivity of graphene…

The imaging of electron and hole puddles in graphene was reported[27] and is shown in Fig. 4.1. The image in Fig. 4.1 is underresolved, but analysis of the potential fluctuations in [9], and higher-resolution imaging by other groups[ref Crommie, Leroy] indicate that the length scale of puddles in graphene is approximately 30nm.

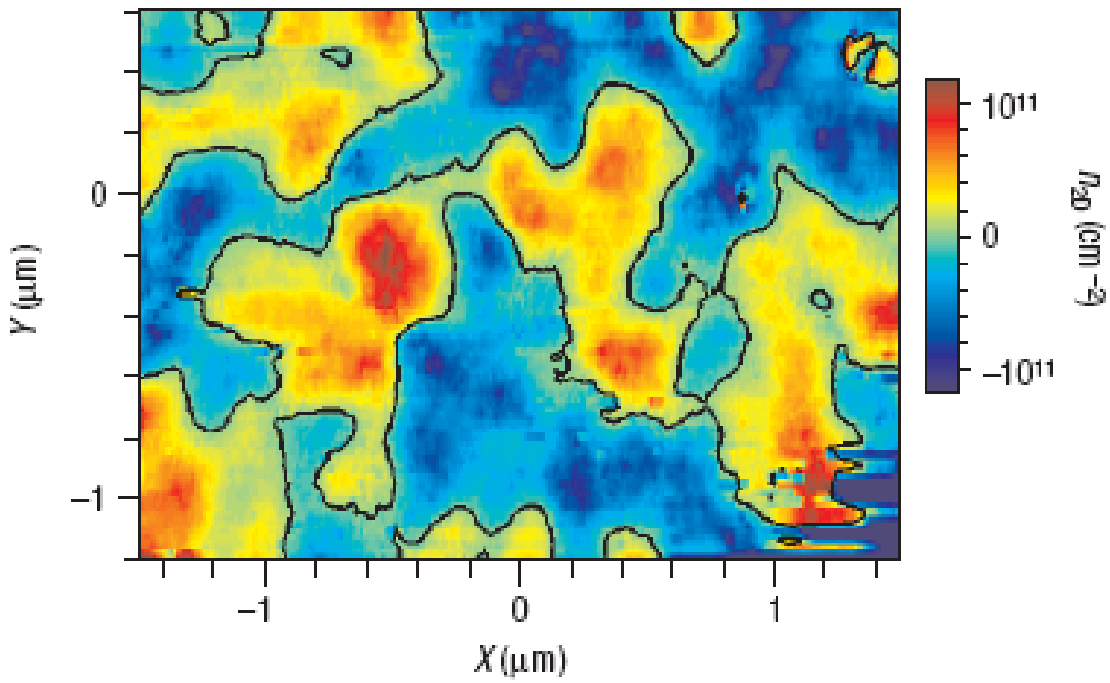

Fig. 4.1. Spatial density variations in single layer graphene extracted from surface potential measurements when the average carrier density is zero. The blue regions correspond to holes and the red regions to electrons. The black contour indicates the zero density contour[27].

4.2. Device Characterization(FE mobility and QHE)

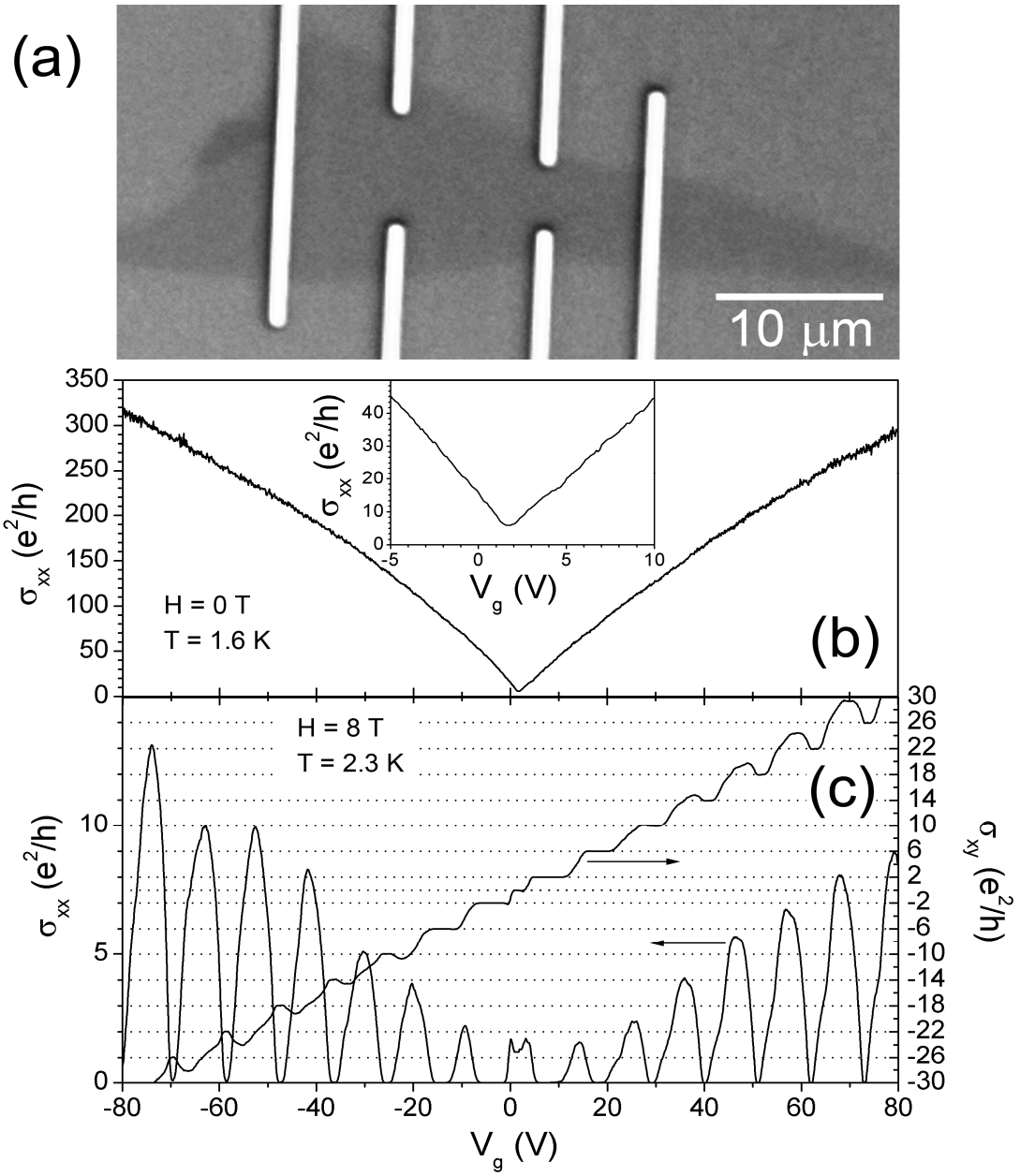

Fig. 4.2 (a) Optical micrograph of graphene device. Contrast is enhanced to show graphene more clearly. White vertical lines are Cr/Au electrodes, graphene is visible as slightly darker region compared to background SiO_2/Si substrate. (b) Longitudinal conductivity σ_{xx} as a function of gate voltage V_g at zero magnetic field and temperature of 1.6 K. (c) σ_{xx} and Hall conductivity σ_{xy} as a function of V_g at magnetic field of 8 T and temperature of 2.3 K.

The device was fabricated following the method described in chapter 2[83].

Figure 4.2a shows an optical micrograph of a completed device; all the data in this

chapter are from this device. I first characterized the carrier density dependence of the conductivity of this device at zero and high magnetic field. Figure 4.2b shows the longitudinal conductivity σ_{xx} as a function of gate voltage V_g. The MCP occurs at $V_{g,MCP} = 1.7$ V. Away from the MCP, the conductivity increases linearly. The field effect mobility $\mu_{FE} = (1/c_g)d\sigma_{xx}/dV_g$ is 1.6 m^2/Vs and 2.0 m^2/Vs for electrons and holes respectively, where $c_g = 1.15 \times 10^{-4}$ F/m^2, as determined from the Hall effect at high density.

Figure 4.2c shows σ_{xx} and the Hall conductivity σ_{xy} as a function of gate voltage at a magnetic field of 8 T[84]. The Hall conductivity shows the half-integer quantized plateaux that are a signature of graphene[1, 85]: $\sigma_{xy} = ve^2/h$, with $v = 4(n + 1/2)$ and n an integer, e the electronic charge, and h Planck's constant. The plateau-like region $\sigma_{xy} \approx 0$ is also evident[86-88].

4.3 Magnetoresistivity near Minimum Conductivity Point(MCP)

I now discuss the magnetoresistivity $\rho_{xx}(B)$ near the MCP. Figure 4.3 shows $\rho_{xx}(B)$ at $V_g = 1.7$V and temperatures from 1.6 K to room temperature. At low fields the magnetoresistivity is roughly temperature independent. At higher fields the resistivity tends to saturate at a value ~$0.4h/e^2$ at low temperatures, and increases with no saturation for $B < 8$ T at room temperature. Figure 4.4 shows the gate voltage dependence of the low-field magnetoresistivity, characterized by the curvature $d^2\rho_{xx}(B)/dB^2$ obtained by

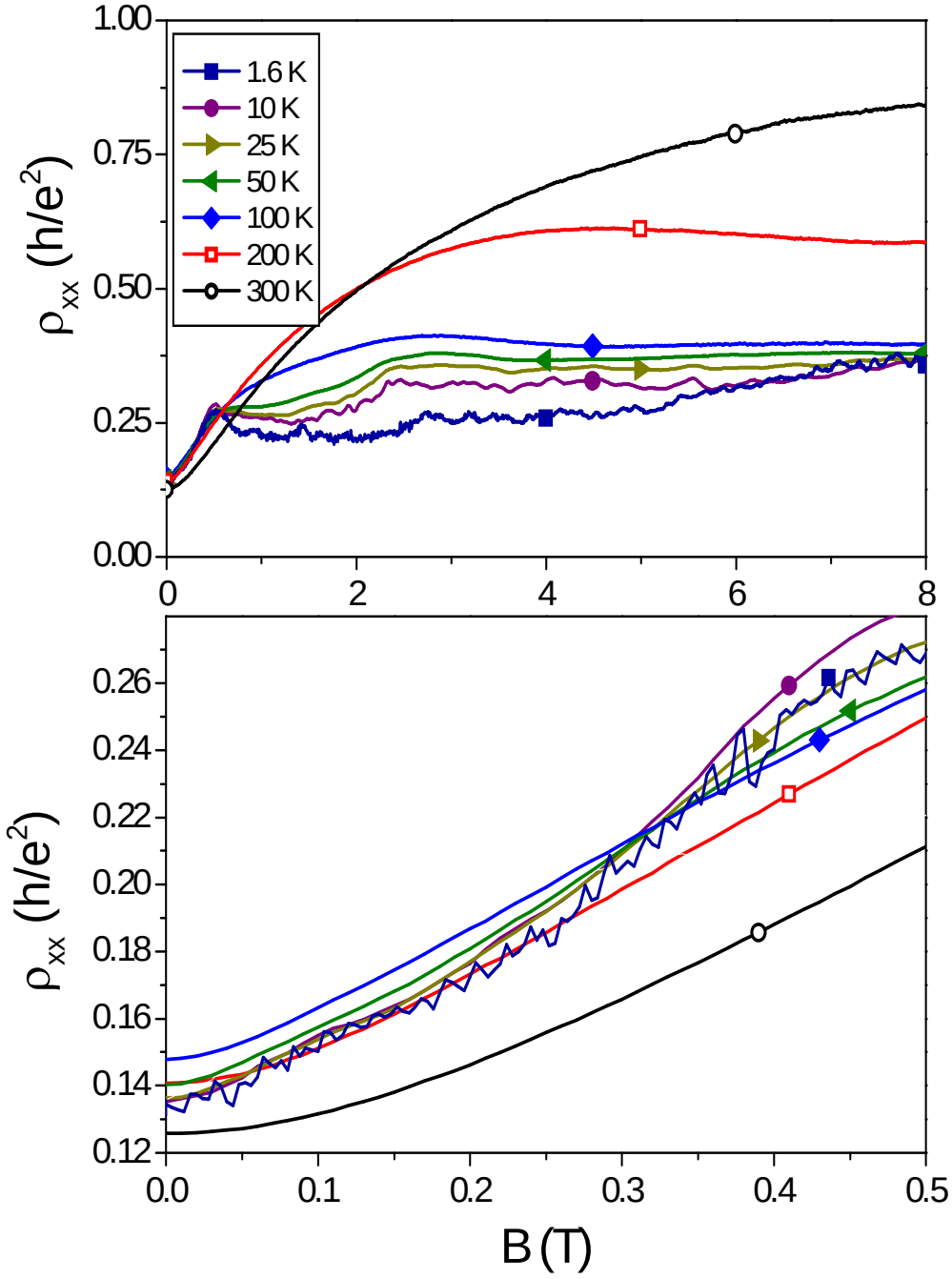

Fig. 4.3. Longitudinal resistivity ρ_{xx} as a function of magnetic field *B* at various temperatures, and a gate voltage of 1.7 V (the point of maximum longitudinal resistivity at zero field). Data are taken on warming from low temperature.

fitting $\rho_{xx}(B)$ to a quadratic over the range -0.2 T < B < 0.2 T. The magnetoresistivity has a sharp peak at the MCP, and falls to near zero at gate voltages more than a few volts from the MCP (at V_g = 10V, the curvature is already 300x lower than at the MCP).

I now discuss the possible origins of the positive magnetoresistivity. Weak antilocalization is possible in graphene[89], and results in a positive magnetoresistivity. However, this effect should saturate at a small magnetic field scale roughly set by the coherence length squared, and should be strongly temperature dependent. Also, consistent with an earlier report[90], I observe no weak localization or anti-localization at larger gate voltages. Hence I conclude that the magnetoresistivity does not result from weak (anti-)localization.

Within the Drude model, a two-dimensional conductor with a single carrier type (e.g. pristine graphene at zero temperature) exhibits no transverse magnetoresistivity, because the force exerted by the Hall field cancels the Lorentz force, and the drift current and resistive voltage are in the same direction. However, a conductor with electrons and holes may exhibit large transverse magnetoresistivity, because the electrons and holes develop components of drift velocity perpendicular to the current which cancel to give zero net transverse current. Both holes and electrons are present at zero temperature in semimetallic graphite, and at finite temperature in graphene. Such a two-fluid model has indeed been proposed to explain the gate voltage dependence of the Hall conductivity in few-layer[91] and single-layer graphene[92]. For a conductor with electrons and holes of concentrations n and p and

of equal mobility $\mu, \sigma_{xx}^{n,p}(B) = \frac{\sigma_{xx}^{n,p}(0)}{1+(\mu B)^2}$ and $\sigma_{xy}^{n,p}(B) = \pm\frac{\sigma_{xx}^{n,p}(0)\mu B}{1+(\mu B)^2}$ where the

positive sign is for electrons, negative for holes, and

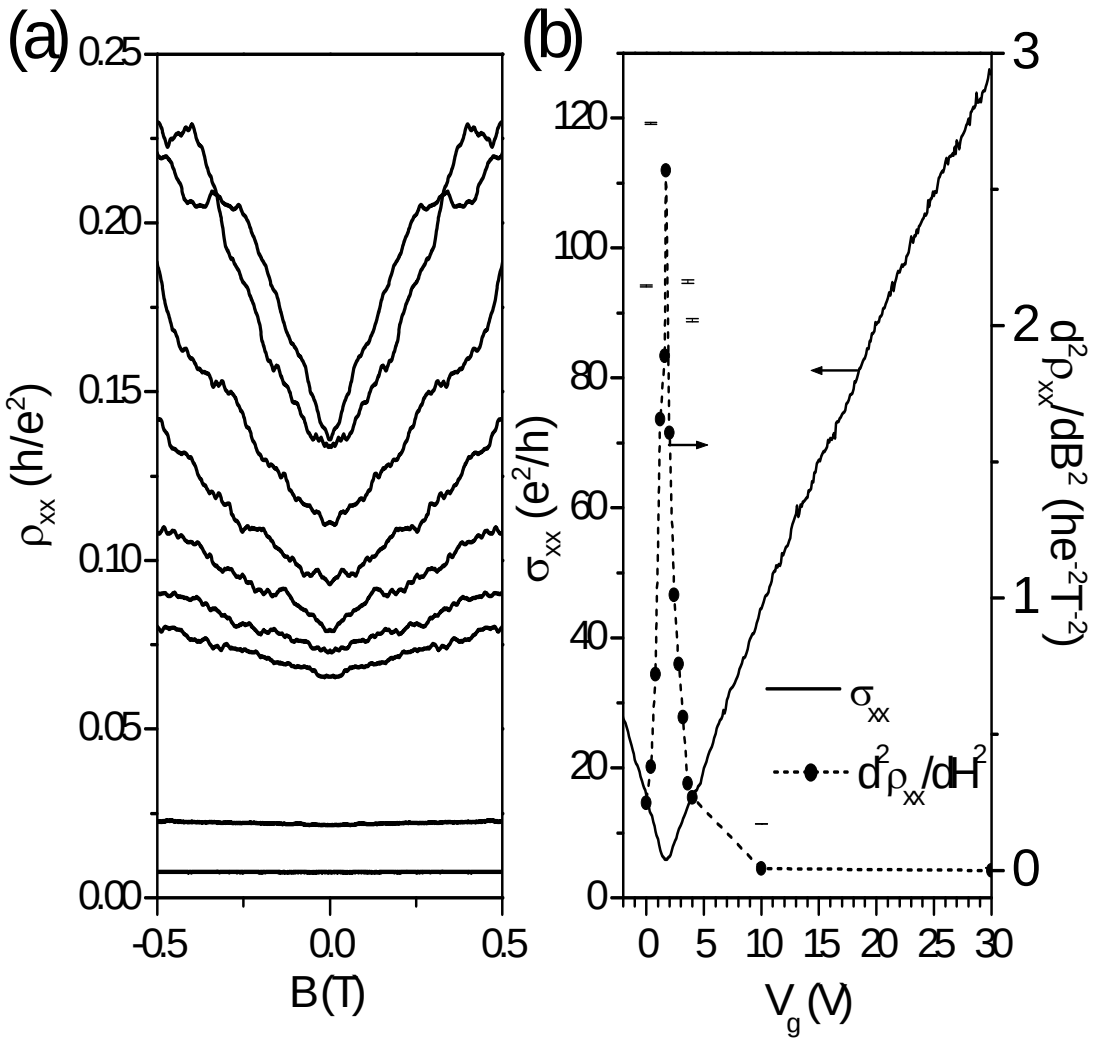

Fig. 4.4. (a) Longitudinal resistivity ρ_{xx} as a function of magnetic field B at various gate voltages. From top to bottom, curves correspond to gate voltages of 1.7, 2.0, 2.4, 2.8, 3.2, 3.6, 4.0, 10, and 30 V. (b) Longitudinal conductivity σ_{xx} (black line, left axis) and the second derivative of the longitudinal resistivity vs. magnetic field $d^2\rho_{xx}/dB^2$ at small B (filled circles, right axis) as a function of gate voltage V_g at a temperature of 1.6 K. Dotted line extrapolates between filled circles.

$\sigma_{xx}^{n,p}(0) = (n, p)e\mu$. Then the resistivity components are:

$$\rho_{xx}(B) = \rho_{xx}(0)\frac{1+(\mu B)^2}{1+(\alpha\mu B)^2} \qquad \rho_{xy}(B) = \alpha\mu B\rho_{xx}(B) \tag{4.1}$$

where $\alpha = (p-n)/(p+n)$. At the MCP, $\alpha = 0$, and $\rho_{xx}(B) \propto 1 + (\mu B)^2$ and $\rho_{xy} = 0$. Far from the MCP, I expect that $|\alpha| \rightarrow 1$, and $\rho_{xx}(B) \approx \rho_{xx}(0)$. This model thus explains *qualitatively* the sharp peak in $\rho_{xx}(B)$ at the MCP (Fig. 4.4). However, it does not explain the functional form of $\rho_{xx}(B)$; Fig. 4.5 shows $\rho_{xx}(B)$ at $T = 300$ K, open circles are the experimental data, while the dotted and dash-dot lines are fits to Eqn. 4.1 with $\mu = 1.9$ m^2/Vs and $\alpha = 0$, and $\mu = 2.3$ m^2/Vs and $\alpha = 0.4$ ($\rho_{xx}(0) = 0.125$ in both cases). In each case μ is chosen to match the low-B curvature of the resistivity $d^2\rho_{xx}(B)/dB^2 = 2\mu/(1-\alpha^2)$ as determined by a fit to the experimental data for -0.2 T < B < 0.2 T (Fig. 4.5b). The fits are poor outside the low-B region. The two-fluid model fails quantitatively in other respects: The near-absence of temperature dependence of ρ_{xx} is not explained; at the MCP, $n = p \approx 0.52(kT/\hbar v_F)^2$, so I expect $\sigma_{xx}(0) = (n + p)e\mu$ to depend quadratically on temperature. At $T = 1.6$ K, $n = p \approx 2.3 \times 10^6$ cm^{-2}, and the peak in V_g should have a width less than 1 mV, not ~2 V as observed in Fig 4.4. As discussed previously, another mechanism is already needed to explain the finite conductivity on order e^2/h at the MCP. My data puts a further constraint on this mechanism: it must also explain the magnetoresistivity at the MCP.

The finite conductivity and the large magnetoresistivity at the MCP together do suggest $p+n$ remains finite while $p-n \rightarrow 0$. There is another scenario in which this is possible: as discussed above, Adam et al[78]. propose that local potential

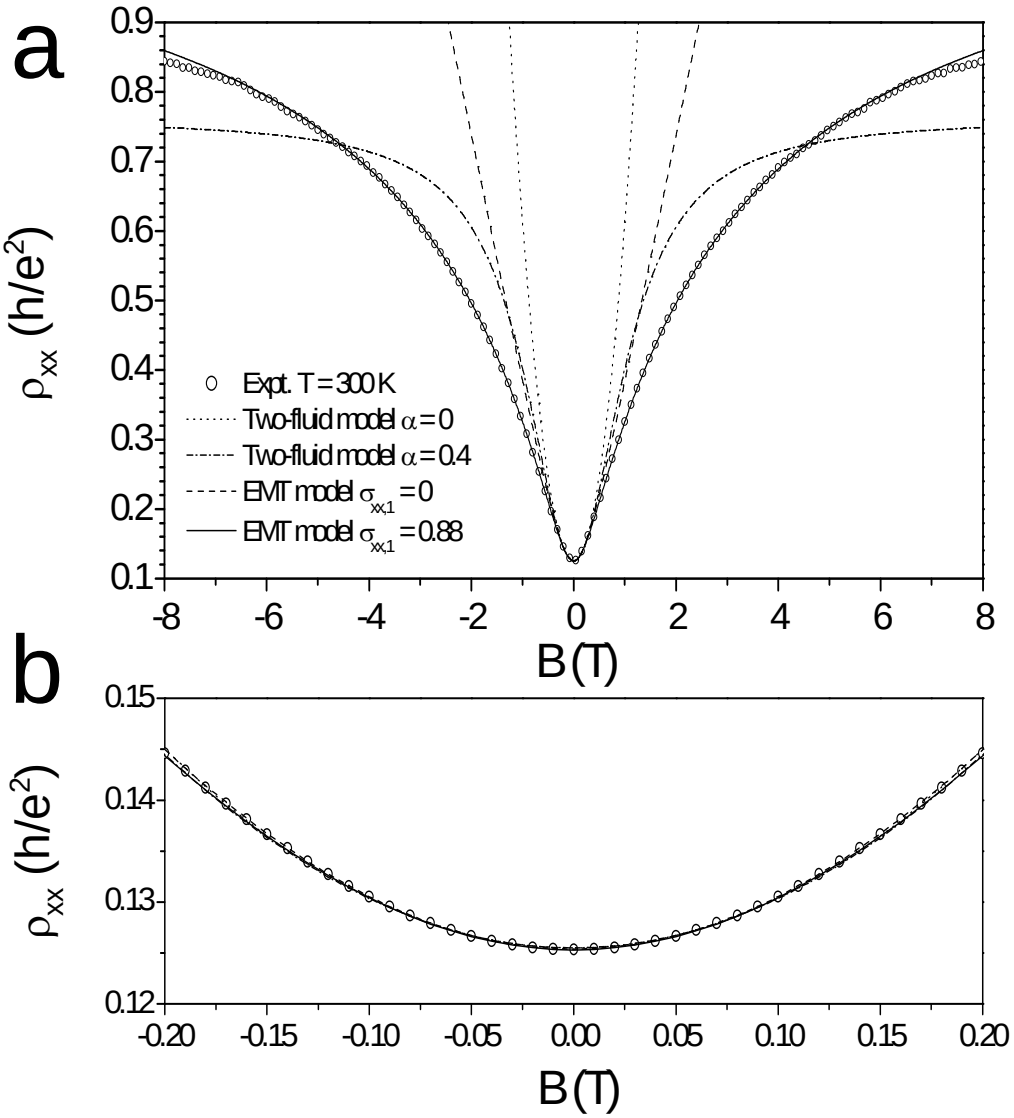

Fig. 4.5. Longitudinal resistivity ρ_{xx} as a function of magnetic field B at a temperature of 300 K. (a) Open circles are experimental data, dotted line is a fit to the two-fluid model (Eqn. 1 in text) with $\alpha = 0$, dash-dot line is a fit to the two-fluid model with $\alpha = 0.4$. Dashed line is a fit to the inhomogeneous model (Eqn. 2 in text), and solid line is a fit the the inhomogeneous model with an additional parallel conductivity (Eqn. 3 in text), with $\sigma_{xx,1} = 0.88\ e^2/h$. In all fits, the zero-field resistivity $\rho_{xx}(0)$ and the low-field curvature $d^2\rho_{xx}(B)/dB^2$ are the same, determined by fits to the experimental data at -0.2 T < B < 0.2 T, as shown in (b).

fluctuations may induce electron and hole "puddles" in a nominally neutral graphene sheet. Individual graphene samples are characterized by a single parameter, the density of Coulomb impurities n_{imp}, which accurately predicts the minimum conductivity, the carrier density at which the MCP appears, and the field effect mobility. (An additional parameter, the distance of impurities from the graphene sheet, is determined to be 1 nm from the global fit to data from several research groups.) Within this model, the impurity density is given by $n_{imp} = (5 \times 10^{15}\ V^{-1}s^{-1})\mu^{-1} \approx 2.8 \times 10^{15}\ m^{-2}$ for our sample (using $\mu = 1.8\ m^2/Vs$, the average field-effect mobility for electrons and holes). At the MCP, the current is carried by an effective carrier density $n^* \approx 1.1 \times 10^{15}\ m^{-2}$, the minimum conductivity is given by $\sigma_{xx,min} = (20e^2/h)(n^*/n_{imp}) \approx 7.8e^2/h$, the MCP occurs at a gate voltage $V_{g,MCP} \approx \bar{n}e/c_g = (n_{imp}^2/4n^*)e/c_g = 2.5$ V, while the spatial charge inhomogeneity is expected to be important in a region of width $\Delta V_g = 2n^*e/c_g = 3.0$ V around the MCP. These values are in good agreement with the experimental values $\sigma_{xx,min} = 5.9e^2/h$, and $V_{g,MCP} = 1.7$ V. ΔV_g agrees well with both the width of the peak in magnetoresistivity vs. V_g in Fig 4.4, and the width of the plateau where $\sigma_{xy} \approx 0$ in Figure 4.2b (~2.1 V). The effective carrier density $n^* \approx 1.1 \times 10^{15}\ m^{-2}$ is larger than the thermally excited carrier density at room temperature $0.8 \times 10^{15}\ m^{-2}$ (see above), so I expect temperature dependence to be small at least up to around room temperature, as observed.

I now discuss the expected magnetoresistivity for the model of Adam, et al[78]. While the general problem of magnetoresistivity in a spatially inhomogeneous conductor is complex[93], the magnetoresistivity of an inhomogeneous distribution of

electrons and holes with equal mobility and equal concentrations has been solved exactly[25], and has a simple analytical form:

$$\sigma_{xx}(B) = \sigma_{xx}(0)\left(1+(\mu B)^2\right)^{-1/2} \qquad \sigma_{xy}(B) = 0. \tag{4.2}$$

Equation 4.2 predicts a magnetoresistivity which is linear in B at high fields, as shown by the dashed line in Fig. 4.5, with $\sigma_{xx}(0) = 8.0\ e^2/h$ and $\mu = 2.9\ \mathrm{m}^2/\mathrm{Vs}$. The low-field

behavior is consistent with Eqn. 4.2. I find however, that the fit is greatly improved if Eqn. 4.2 is modified to the following phenomenological form:

$$\rho_{xx}(B) = \left(\sigma_{xx,1} + \frac{\sigma_{xx,0}}{\left(1+(\mu B)^2\right)^{1/2}}\right)^{-1}. \tag{4.3}$$

In Fig. 4.5, I plot the experimental data (open circles) and a fit to Eqn. 4.3 (solid line) with $\sigma_{xx,0} = 7.1\ e^2/h$, $\sigma_{xx,1} = 0.88\ e^2/h$, and $\mu = 3.1\ \mathrm{m}^2/\mathrm{Vs}$. The fit is excellent. Again, $\rho_{xx}(0)$ and $d^2\rho_{xx}(B)/dB^2 = \mu/(1 + \sigma_{xx,1}/\sigma_{xx,0})$ are determined by the low-B data alone, leaving only one additional degree of freedom to fit the high-B data.

In proposing Eq. 4.3, I did not have a physical origin for the extra conductivity term. However, it is reasonable to expect deviation from Eqn. 4.2 for several reasons: the electron and hole concentration are not perfectly balanced, the electron and hole mobilities are not equal[26], and the sample geometry is far from the ideal Hall bar (some current must flow through the electrodes). Subsequent theoretical work using effective medium theory has obtained very good agreement

with our experimental results, taking into account a small imbalance of mobilities or carrier concentrations for electrons and holes.

From the conductivity and mobility obtained from the fit to Eqn. 4.2 I can obtain a carrier density $n^*_{exp} = \sigma_{xx}(0)/\mu e = 6.6 \times 10^{14}$ m^{-2}. This density is about half the predicted $n^* \approx 1.1 \times 10^{15}$ m^{-2}. Overall the data suggest that the mobility near the minimum conductivity point is greater than the field-effect mobility; this is consistent with the experimental observation[26] and theoretical prediction of a residual conductivity at the Dirac point[94].

At low temperatures and high magnetic fields, $\rho_{xx}(B)$ saturates to a constant value ~$0.4h/e^2$. Additionally, a plateau-like region of $\sigma_{xy} \approx 0$ is evident in $\sigma_{xy}(V_g)$. This latter feature has been interpreted as an integer quantum Hall effect (QHE) state arising either from the splitting of the valley degeneracy in the $n = 0$ Landau level (LL)[88], or due to spin splitting of the 0th LL resulting in counter-propagating spin polarized edge states[86]. The latter model gives rise to a dissipative QHE state, in which σ_{xy} is only approximately quantized, and ρ_{xx} is finite. Such a dissipative QHE state would also be expected in spatially inhomogeneous graphene, in which the 0th LL lies below or above the Fermi level in electron or hole regions respectively. The bulk then would consist of incompressible electron and hole QHE liquids, separated by regions in which the $n = 0$ LL crosses the Fermi level, i.e. fourfold degenerate edge states with counter-propagating modes. From $\mu = 2.9$ m^2/Vs and $n^*_{exp} = 6.6 \times 10^{14}$ cm^{-2}, I estimate the scattering time $\tau = 87$ fs, and the LL broadening $\Gamma \approx \hbar/\tau = 7.6$ meV. For $B = 8$ T the spacing between the 0th and 1st LL is ~100 meV, the Zeeman energy is $g\mu_B B = 0.9$ meV assuming $g = 2$. The average density n^*_{exp} gives a LL

filling factor $\nu = 2$ at $B = 1.4$ T, and 0.34 at $B = 8$ T. Of course, the maximum density within the puddle must be greater than the average density n^*, and the QHE occurs over a broad range around the quantized filling factor (for example, the $\nu = +2$ plateau occurs from $\nu = 1.1$ - 3.3), so it is plausible that the puddles could be in the $\nu = \pm 2$ QHE states. The imaging of electron and hole puddles in graphene was reported[27], and the puddle diameter estimated to be ~30 nm. I then expect that quantum effects should be important when the magnetic length is less than the puddle diameter, i.e. $B > 0.8$ T, and the temperature is less than $E_F(n^*)$, i.e. T < 350 K. This is in qualitative agreement with Fig4.3 where significant deviation of $\rho_{xx}(B)$ from Eqn. 4.3 occurs at temperatures $T \leq 100$K and $B \geq 0.8$ T, but, since Ref[80]. is inadequate to predict the behavior in the quantum regime, more work is needed to understand the high-field, low-temperature behavior near the MCP.

4.4 Conclusion

In conclusion, I have measured the magnetic field-dependent longitudinal and Hall components of the resistivity $\rho_{xx}(H)$ and $\rho_{xy}(H)$ in graphene on silicon dioxide substrates at temperatures 1.6 K $\leq T \leq$ 300 K. At charge densities near the minimum conductivity point $\rho_{xx}(H)$ is strongly enhanced and $\rho_{xy}(H)$ is suppressed, indicating nearly equal electron and hole contributions to the current. The data are inconsistent with the standard two-fluid model but consistent with the prediction for inhomogeneously distributed electron and hole regions of equal mobility. At low T and high H, $\rho_{xx}(H)$ saturates to a value $\sim h/e^2$, with Hall conductivity $<< e^2/h$, which may indicate a regime of localized $\nu = 2$ and $\nu = -2$ quantum Hall puddles.

Chapter 5. Gate Tunable Graphene Spin Valve

5.1 Why Graphene for Spintronics?

Graphitic carbon nanostructures, e.g. carbon nanotubes (CNT) and graphene, have been proposed as ideal materials for spin conduction[95-101] for several reasons. First, suppression of backscattering[102] allows them to have long electronic mean free paths[103-104]. Second, spin-orbit interaction is very small due to relatively low atomic weight of carbon[105-106]. Spin-orbit coupling allows spin relaxation due to the transformation of intrinsic electric fields in a solid into magnetic fields in electron's reference frame, and spin-orbit effects increase rapidly with atomic number. A theoretical estimation shows that spin-orbit coupling in graphene is negligible even for disordered graphene [107]. Third, since 99% of natural carbon consists of zero-spin isotope ^{12}C, carbon nanostructures have very weak hyperfine interaction, which is another mechanism of spin relaxation[108]. Therefore, it is predicted that graphene will have a long spin life time on the order of μs.

In this chapter I discuss my efforts to inject and detect spin currents in graphene devices. I was able to observe clear switching of the non-local four-probe resistance of graphene spin-valves due to switching of the magnetization of ferromagnetic spin injector contacts. The spin signal was observable up to room temperature. Interestingly, the spin signal fluctuated with gate voltage, even changing sign. I propose that these fluctuations, in my rather short spin valve devices, are due to Fabry-Perot oscillations as discussed in Chapter 3.

Demonstration of spin injection and detection in graphene opens new opportunities to study spin-dependent transport in exotic electronic states such as the quantum Hall[109-110] and quantum spin Hall[105] states, and proposed spin-polarized edge states[111] in graphene ribbons.

5.2 Nonlocal spin valve effect

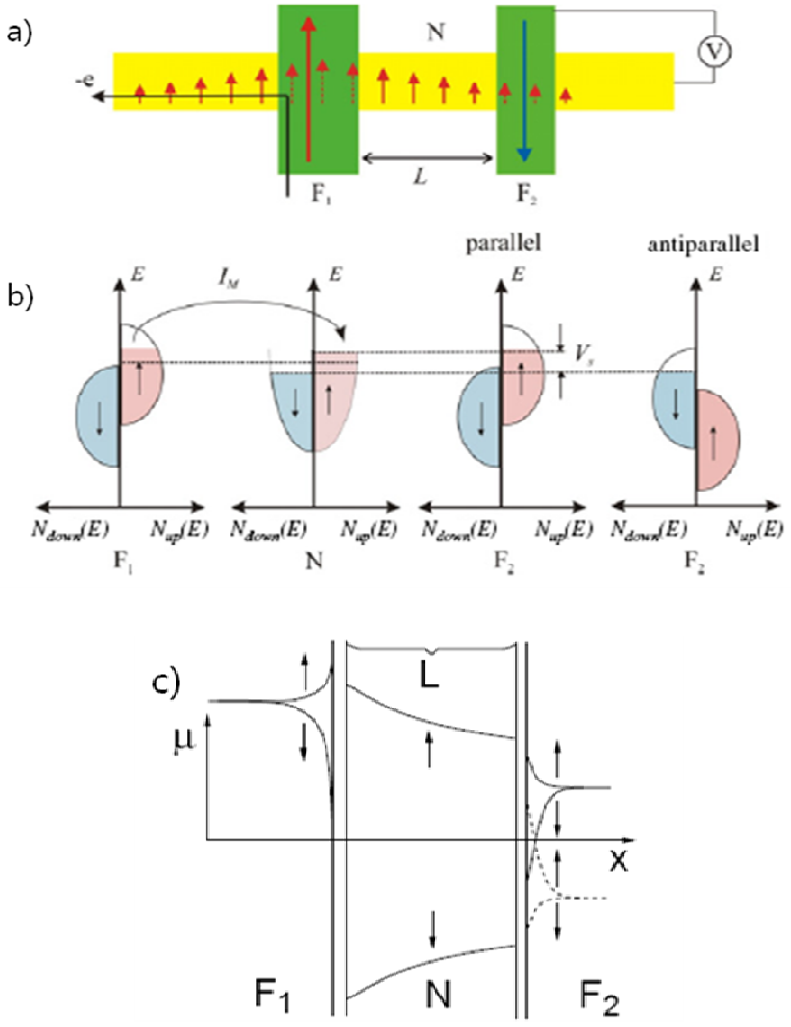

Fig. 5.1 a) A schematic of nonlocal spin valve device consisting of two ferromagnetic contact F_1 and F_2 and a normal conductor N. large arrows in F_1 and F_2 indicate directions of magnetization and small arrows in N indicate spin polarizations of electrons b) Band structure illustration of spin injection and spin detection. c) Electrochemical potentials for spin up (↑) and spin down (↓) as a function of position in F_1, N, and F_2. Figures are from ref[112-113].

A nonlocal spin valve device consists of two lateral ferromagnetic contacts (F_1 and F_2) laterally separated on a nonmagnetic conductor N. Fig. 5.1(b) shows band structures of F_1, N and F_2. To measure nonlocal spin valve signal, charge current is injected from F_1 to left end of N (opposite to F_2), and voltage is measured between F_2 and right end of N. In the absence of charge current flow from F_1 and N, the electrochemical potentials of spin- up and spin-down electrons in N are the same. When a charge current is injected from F_1 to N, the majority of electrons at the Fermi level are spin-up since the density of states for spin-up electrons at the Fermi level is higher than spin-down electrons in F_1 as in Fig.5.1(b). This leads to spin accumulation in N near F_1 as in Fig. 5.1(a). Spin accumulation in N acts as a spin electromotive force which produces a voltage $V \square (\mu_\uparrow - \mu_\downarrow)$, where $\mu_\uparrow$ and $\mu_\downarrow$ are the chemical potentials for up and down spins, respectively. This voltage can be measured at the interface F_2 and N as in Fig.5.1.a) and c). As electron spins can be flipped by different mechanisms such as spin-orbit coupling or magnetic impurity scattering, this voltage $V \square (\mu_\uparrow - \mu_\downarrow)$ decreases as the distance L between F_1 and F_2 increases as shown in Fig.5.1c). The characteristic length defining how long the spin polarization can be preserved is called spin diffusion length. Even if the charge current flows only from F_1 to N, spin polarization diffuses in both directions towards left and right side of N. The advantage of the nonlocal spin valve geometry comes from the decoupling of charge current and spin current. In the direction from F_1 to right side of N, there is no charge current, but only net spin polarization occurs. Thus this geometry excludes the possibility of a voltage signal V arising from AMR (anisotropic magnetoresistance) or Hall effect from ferromagnetic electrodes, which

would require a charge current in the voltage detection portion of the device[113].

5.3 Fabrication and Characterization

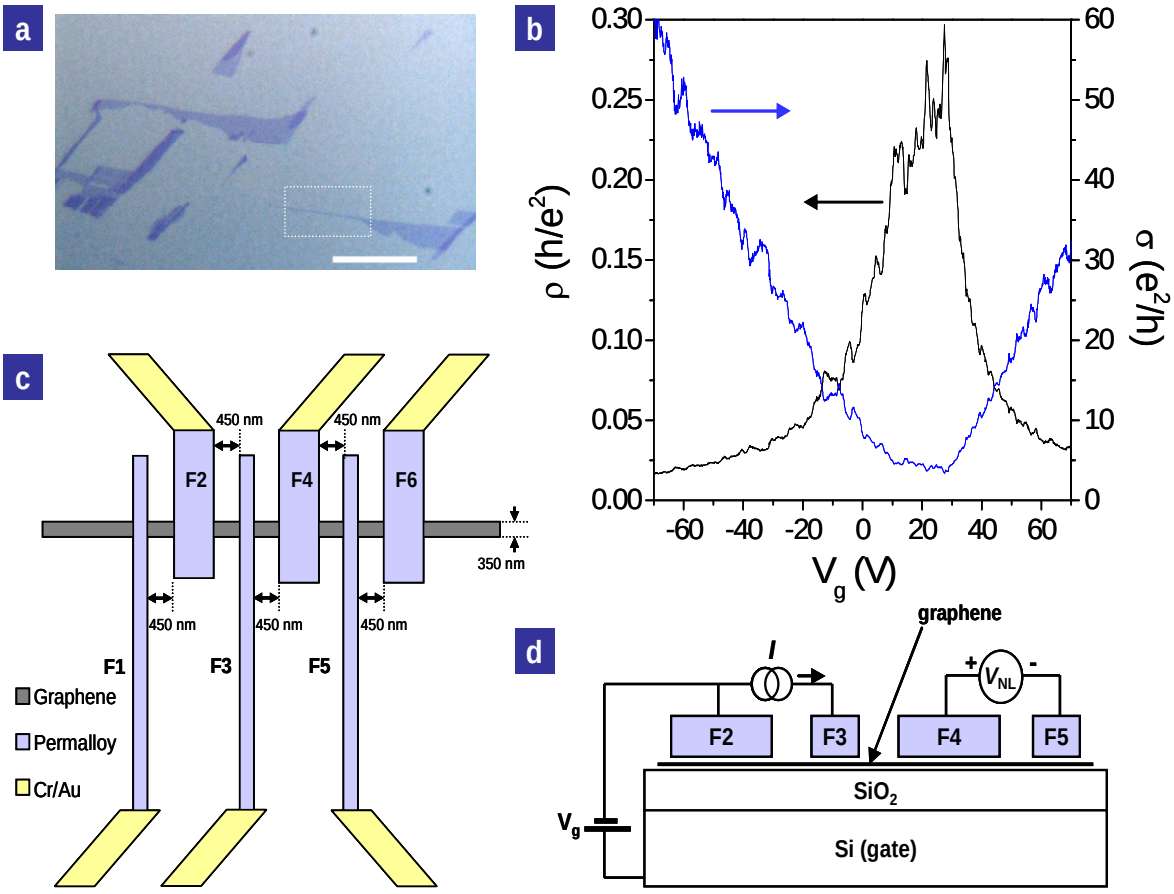

Fig. 5.2 Graphene spin-valve device. a, Optical micrograph of graphene on SiO_2/Si substrate. Scale bar is 10 microns, white box shows graphene flake used in this study, which has similar contrast to other graphene samples for which half-integer quantum Hall effect was measured. b, Gate voltage (V_g) dependence of four-probe resistivity ρ (black, left scale) and conductivity σ (blue, right scale) at a temperature of 1.25 K. The field-effect mobility $\mu_{FE} = (1/c_g)|d\sigma/dV_g|$ is approximately 2500 cm^2/Vs, where c_g = 1.15 x 10^{-4} F/m^2 is the gate capacitance. In this local resistivity measurement, electrodes F4 and F5 were used as voltage probes, and the current contacts were F3 and F6. c,d, Schematics of device layout. c, Plan view. d, Side view, showing setup for non-local resistance measurement. Six ferromagnetic Permalloy electrodes F1-F6 were deposited on top of graphene strip. To give different coercive fields, F1, F3, F5 have dimensions 1.0 μm x 3 μm, and F2, F4, F6 are 0.4 μm x 15 μm. Spaces between all the electrodes are 450nm.

The graphene device studied here was fabricated in a similar method described in Chapter 2. Once the most transparent graphene flake is exfoliated and identified on 300nm SiO2/Si substrate as in Fig. 5.2a), ferromagnetic permalloy electrodes are formed by electron-beam lithography (EBL) followed by thermal evaporation as in Fig.5.2b); a second EBL step establishes contact to the Permalloy via normal Cr/Au electrodes. As described in Fig. 5.2b), six ferromagnetic Permalloy electrodes F1-F6 were deposited on top of graphene strip. To give different coercive fields of magnetization, F1, F3, F5 have dimensions 1.0 μm x 3 μm, and F2, F4, F6 are 0.4 μm x 15 μm. (Higher aspect ratio produces higher coercive fields of the magnetic electrodes.) Spaces between all the electrodes are 450nm. Once device fabrication is completed, I mounted it in our ^{4}He cryostat system. I tried not to spend long time before cooling down the samples since often I observed contact resistance increases to order of MΩ in 24 hours at room temperature. I believe that a moderate increase in contact resistance before measurement establishes a tunnel barrier between graphene and the ferromagnetic electrod, which improves spin injection and allows me to observe an increased spin valve signal[114-118] although it can also increase signal to noise ratio.

Fig. 5.2b) shows the gate voltage (V_g) dependence of the four probe resistivity ρ and conductivity σ measured at the base temperature, T=1.25K in our ^{4}He cryostat. Similar to other single- and bi-layer graphene devices[109, 119] σ(V_g) shows a broad minimum around $4e^2/h$, where e is the electronic charge and h Planck's constant, increasing linearly with V_g away from the minimum at V_{cnp} (the charge neutrality point, CNP). The σ(Vg) curve shows a relatively broad plateau region at the

minimum conductivity, which indicates that this device has large amount of charged impurities[120-121].

5.4 Gate-Modulated Spin Valve Measurement

I performed non-local spin valve measurement by using four ferromagnetic electrodes[114-116]. As described in Fig.5.2d), I inject spin current into graphene by flowing charge current from F3 to F2. Then, ideally, excess spin diffuses through channel from F3 to F4 and F5, with no accompanying charge current. I detect this spin diffusion by a voltage established between electrodes F4 and F5, which are ferromagnetic and therefore preferentially sensitive to one spin potential. This non-local spin valve measurement scheme excludes any unintended signals from ferromagnetic electrodes such as anomalous Hall effect and anisotropic magnetoresistance (AMR) by separating spin and charge current. It also excludes the sheet resistance of graphene due to absence of charge flowing through the graphene channel.

Fig. 5.3a) shows the four-probe non-local resistance $R_{nl} = V_{nl}/I$ (see Fig. 5.2c and d) as a function of magnetic field B at V_g = +70 V at T=20K with current I=100nA. R_{nl} is positive at large B. As B is swept to negative, R_{nl} remains positive as B crosses zero, then switches to a negative value at $B \approx$ -150 G before returning positive at $B \approx$ -250 G. Upon sweeping B positive, switching occurs at B = +150 G and +250 G. This behavior is very similar to that observed in all-metal[114-116, 122] and CNT[117] non-local spin-valves, particularly the sign change of R_{nl} when the current and voltage circuits are separated[117, 122]. Hence we identify these two magnetic fields as the coercive fields of F4 and F3 respectively. The switching

behavior may then be explained as follows: at high *B*, F3 preferentially injects its majority spin which diffuses to F4 and is detected as an increase in the chemical potential of F4's majority spin (since the magnetizations of F3 and F4 are

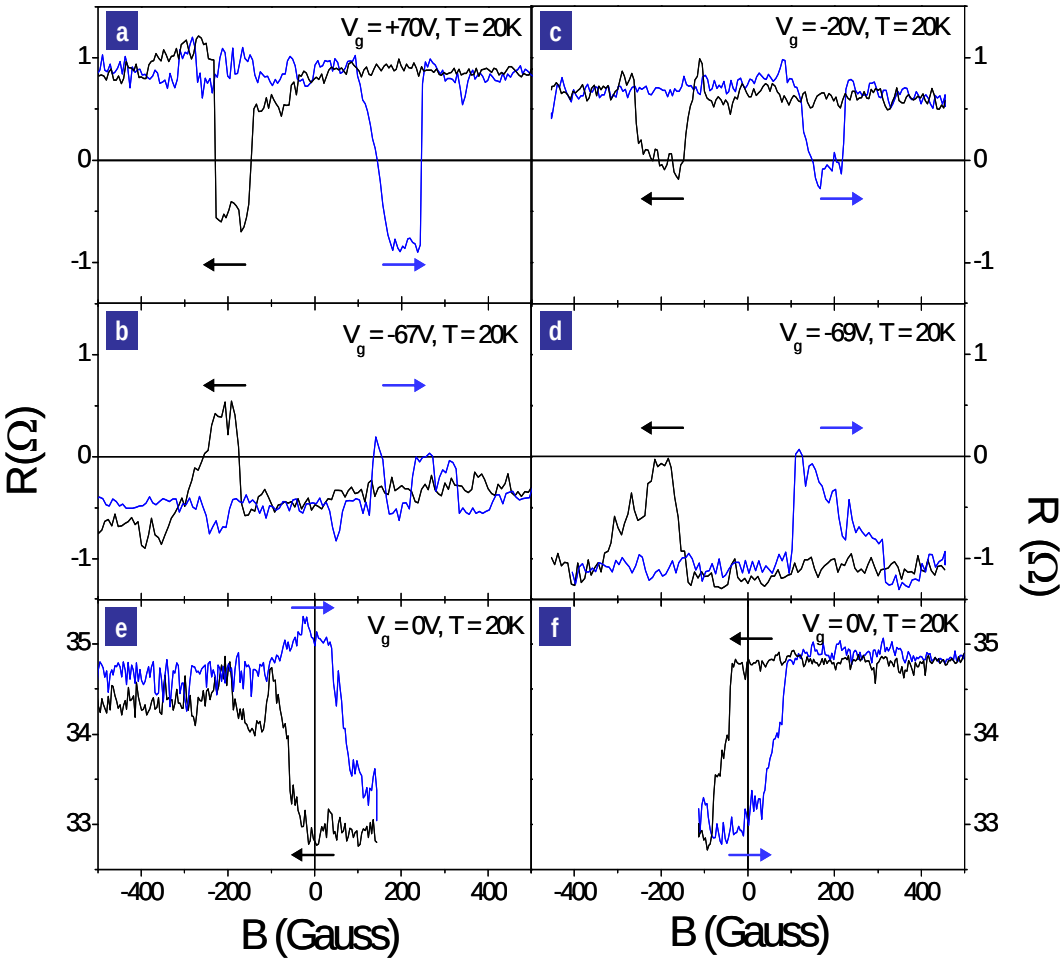

Fig.5.3. Non-local spin-valve effect in graphene. a,b, Nonlocal resistance R_{nl} (see Fig. 5.2d) as a function of magnetic field measured at temperature T = 20K with current I = 100 nA. a,b F2, F3 as current leads; F4, F5 voltage leads. c,d F4, F5 as current leads; F2, F3 voltage leads. a, Gate voltage V_g = +70 V. b, V_g = -67 V. c, Gate voltage V_g = -20 V. d, V_g = -69 V. The non-local resistance switches sign upon sweeping magnetic field, which indicates that a spin current flows from electrodes F3 to F4 (see Fig. 5.2c,d). The reversal of sign of the non-local resistance with gate voltage (a vs. b and c vs. d) is discussed in the text and in Fig. 5.4. e,f, Memory effect measured at T = 20 K, I = 100 nA, V_g = 0 V. F1, F2 are current leads; F3, F4

are voltage leads. In a-f, blue curves correspond to positive sweep direction of magnetic field; black curves, negative sweep direction.

parallel) resulting in positive R_{nl}. When F3 and F4 are antiparallel, the voltage reverses, and R_{nl} is negative.

Fig. 5.3b)-d) show the same measurement performed at different gate voltages and different electrode arrangements. In Fig. 5.3b) and 5.3d), the high-B value is negative, and R_{nl} switches to near zero (or slightly positive) for B between the two coercive fields. The sign change is discussed further below. Fig. 5.3e) and 5.3f) show the memory effect: by reversing the field sweep direction after flipping the magnetization of F4 but before flipping the magnetization of F3, two R_{nl} states can be observed at $B = 0$, corresponding to the two possible magnetization states of F4.

First we discuss whether R_{nl} arises due to charge current or spin current flowing between F3 and F4. Ideally, as mentioned earlier in this chapter, charge current would flow only between F3 and F2, eliminating contributions to the R_{nl} from magnetoresistance of the ferromagnetic electrodes, the channel, or the electrode-channel interface. However, because R_{nl} is ~3 orders of magnitude smaller than the device resistance, it is possible that some charge current flows through a tortuous path from F3 to F4 and F5. We investigate this by measuring the gate voltage and temperature dependence of R_{nl}.

Fig. 5.4a) shows the gate voltage dependence of R_{nl} in the parallel and antiparallel state, $R_{nl,p}$ and $R_{nl,ap}$, as well as their average value. Fig. 5.4b) shows the non-local spin-valve signal ΔR. R_{avg}, $R_{nl,p}$ and $R_{nl,ap}$ all show a peak near the CNP (10 V < V_g < 30 V), while ΔR is near zero in this region. Well outside this region (V_g < -

20 or V_g > 40 V), $R_{nl,p}$ and $R_{nl,ap}$ have nearly equal magnitude and opposite sign (R_{avg} is near zero) and ΔR is larger and shows quasi-periodic oscillations with V_g. The peak in $R_{avg}(V_g)$ near the CNP suggests that charge current *does* flow in the region between F3 and F4 for these gate to voltages. However, $R_{avg}(V_g)$ is not simply proportional to

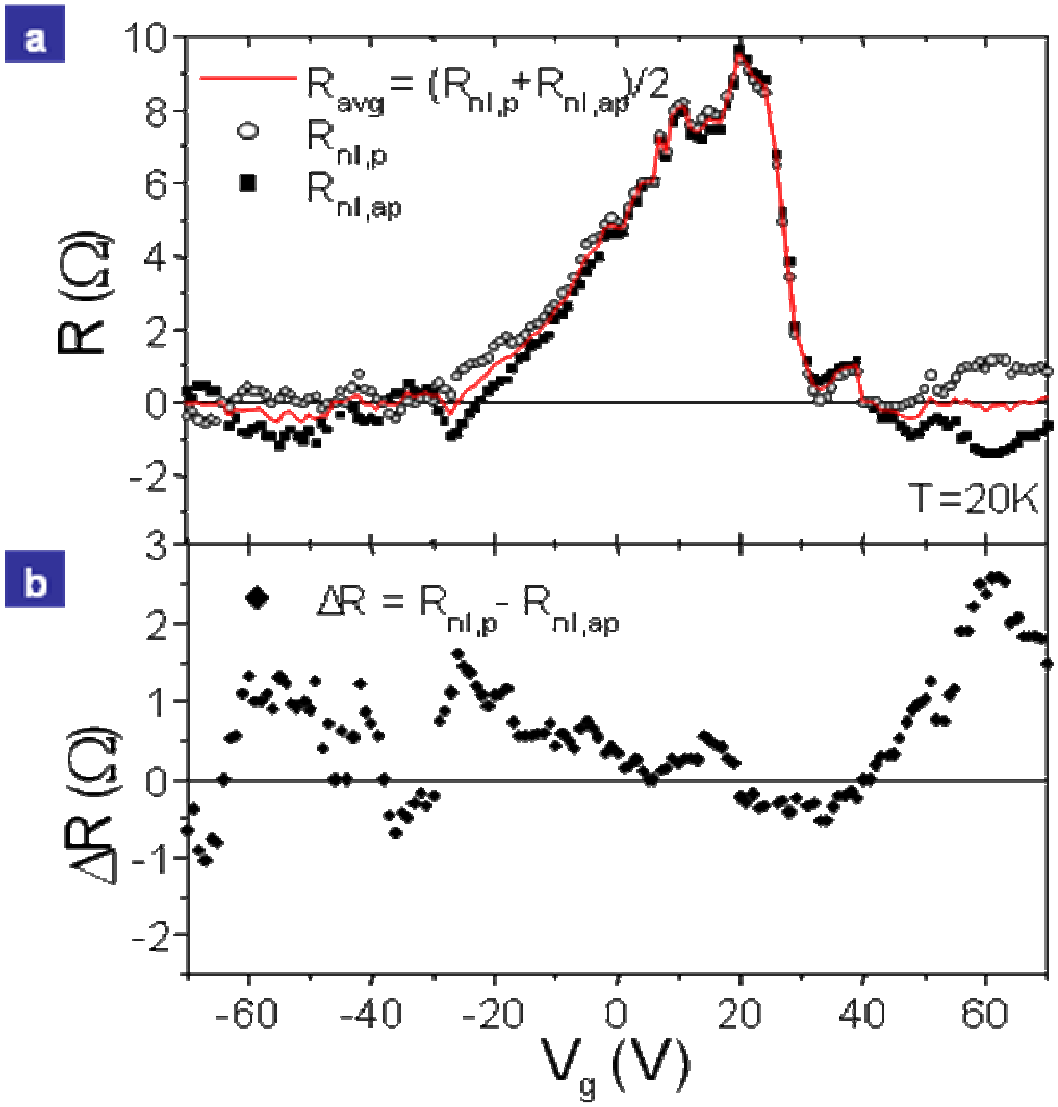

Fig. 5.4 Gate-voltage dependence of spin-valve signal. a,b, The same electrode configuration is used as for Fig. 5.3a,b. a, Resistance as a function of gate voltage for electrodes with magnetizations parallel ($R_{nl,p}$), antiparallel ($R_{nl,ap}$), and their average $R_{avg} = (R_{nl,p} + R_{nl,ap})/2$. b, The spin valve signal $\Delta R = R_{nl,p} - R_{nl,ap}$ as a function of gate voltage.

$\rho(V_g)$ but rather drops near zero at large V_g while $\rho(V_g)$ remains finite. Thus the finite $R_{avg}(V_g)$ near the CNP is likely due to the inhomogenous nature of graphene near the CNP[120, 123] (see Chapter 4); here percolating electron and hole regions may cause a tortuous current path.

Away from the CNP, $R_{avg}(V_g)$ drops to near zero, indicating small charge current. Yet $R_{nl,p}$ and $R_{nl,ap}$ remain finite, with near equal magnitude and opposite sign. This is as expected for a pure spin current flowing from F3 to F4, and cannot be explained by a magnetoresistive signal arising from any charge current between F4 and F5. The Hall effect is another possible source of V_{nl}, however, the Hall voltage would be expected to grow large and switch sign near the CNP, rather than showing a peak.

Fig. 5.5 shows the temperature dependence of R_{avg} and ΔR for $V_g = 0$. Here R_{avg} is finite similar to Fig 5.4, but somewhat larger for this electrode configuration. The spin-valve signal ΔR is seen to drop with temperature approximately as $\Delta R \propto T^{-1}$, while R_{avg} is much more weakly temperature dependent; again indicating a different origin for ΔR and R_{avg}. The inset shows a measurement at 300 K performed at higher current; the spin-valve signal can still be observed, confirming expectations of reduced spin scattering in graphene even to high temperature.

We now discuss the magnitude of the spin-valve signal ΔR. For an Ohmically-contacted spin-valve device, the non-local signal may be estimated using $\Delta R = 2\alpha_F^2 \lambda_F^2 R_W^{F2} / (1-\alpha_F^2)^2 L w R_W^N$ (where α_F^2 is spin polarization, λ_F is spin diffusion length in ferromagnet, R_W^F and R_W^N are square resistance of ferromagnetic and non-magnetic material respectively, L and w are length and width of channel) [116]. We

estimate in this case the signal should be on order 10^{-5} Ω. However, we observe finite contact resistance of order 10 kΩ per electrode as estimated from the difference between two-probe and four-probe resistance measurements. In the limit of highly resistive contacts, we would expect the non-local resistance to be given by;

$R_{NL} = \pm \rho_N \lambda_N \exp(-L/\lambda_N) P_1 P_2 / 2A_N$ (where ρ_N is bulk resistivity of nonmagnetic material, λ_N is spin diffusion length in nonmagnetic material, A is cross-sectional area, P_i are the single F/N interface polarizations of the current at the contacts Fi/Ni) [122]. R_{NL}, for long spin-scattering lengths, is on the order of the channel resistance (1-10 kΩ). Our intermediate contact resistance, finite spin-scattering length, and finite polarization of the electrodes will give a lower value of ΔR, similar to the observation of $\Delta R \sim 20$ Ω for a channel resistance 10 kΩ and contact resistance of a few tens of kΩ in a CNT device[117].

I now discuss the origins of the quasi-periodic oscillations of the non-local spin-valve signal $\Delta R(V_g)$. Oscillation of the spin-valve signal with V_g due to spin-orbit coupling has been proposed as the basis of a spin transistor[124]. However, the spin-orbit coupling in graphene is expected to be very small[105], and this effect should not be observable[125]. Oscillations and sign changes of the spin-valve signal have also been observed when the spin current flows through a resonant quantum state, either due to Coulomb blockade[126] or Fabry-Pérot interference [100]. It is evident from Fig. 5.2b) that the sample is not in the Coulomb blockade regime, however $\rho(V_g)$ shows quasi-periodic oscillations. Such oscillations were studied in detail in Chapter 3, and attributed to Fabry-Pérot interference of electronic states reflected from the electrodes[100, 127-128]. I examined similar oscillations in another graphene sample

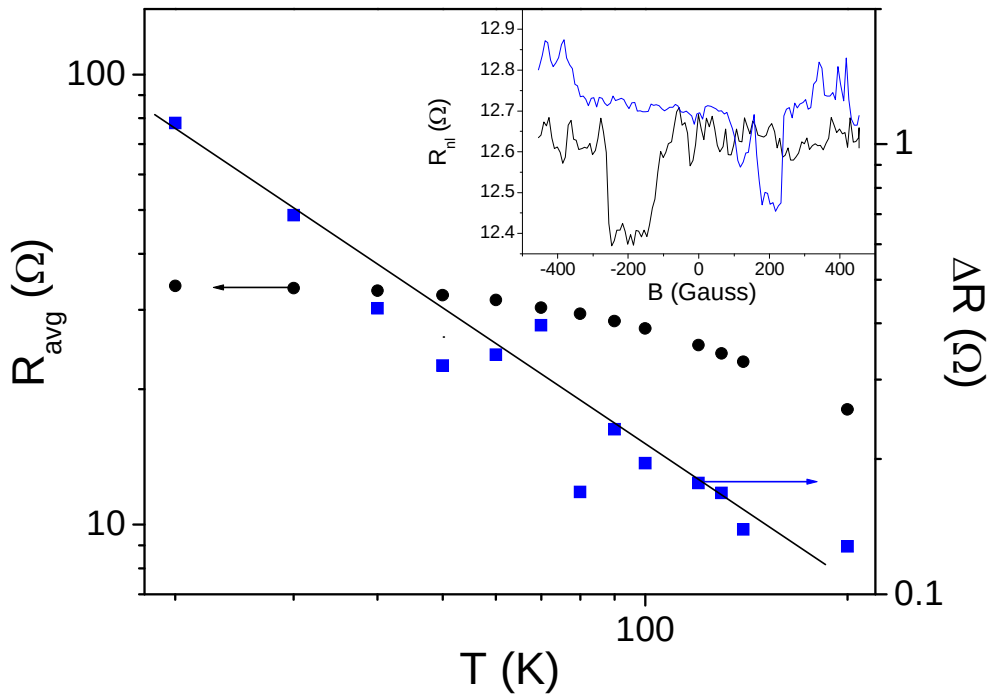

Fig. 5.5. Temperature dependence of spin-valve signal. The average resistance R_{avg} (black circles) and spin valve signal ΔR (blue squares) as a function of temperature at V_g = 0 V and I = 100 nA. The temperature dependence of the spin-valve signal ΔR is much stronger than that of R_{avg} (which likely arises from the charge-current resistance). The solid line shows a power law with exponent -1. Inset shows the non-local resistance R_{nl} as a function of field at T = 300 K and I = 3 μA. Blue curve is positive sweep direction of magnetic field; black curve, negative sweep direction. The spin-valve effect is still observable. The electrodes used for the spin-valve data in main panel and inset are the same as for Fig. 5.3e,f.

in a two-probe geometry (Fig 5.6). In the color-scale plot of differential conductance vs. V_g and drain voltage V, conductance maxima and minima occur along diagonal lines. As discussed in Chapter 3, the change in electron phase due to round trip through graphene channel results in a Fabry-Pérot oscillation pattern (Fig.5.6) with a period in gate voltage $\Delta V_g = \frac{2}{L}\left(\frac{\pi e V_g'}{c_g}\right)^{1/2}$ and in drain voltage

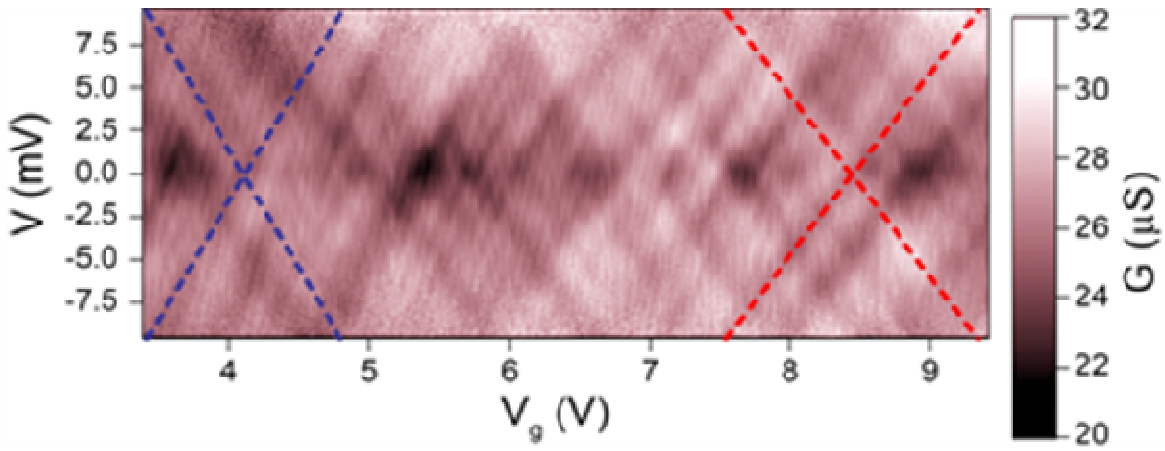

Fig.5.6 Color-scale plot of two-probe differential conductance as a function of gate voltage V_g and drain voltage V for a similar graphene sample contacted by Permalloy electrodes with a spacing 200 nm. The blue and red dashed lines have slopes of ±0.013 and ±0.010 respectively.

$\Delta V = \frac{h v_F}{eL}$. The slope of the lines is $\frac{\Delta V}{\Delta V_g} = \frac{2c_g}{e^2}\frac{1}{D(E)} = h v_F \left(\frac{c_g}{4\pi e^3 V_g'} \right)^{1/2}$, where v_F = 1 x 10^6 m/s is the Fermi velocity, and $V_g' = |V_g - V_{cnp}|$. For the device in Fig. 5.6, L = 200 nm, $V_{cnp} \approx$ -6 V, giving ΔV = 20 mV. For V_g' = 10-15 V, we find ΔV_g = 2.0-2.5 V, and the slope varies from 0.013 to 0.010. The most prominent minima in conductivity at V = 0 occur with spacing ΔV_g = 1.5-2.5 V, however additional features are observed more closely spaced in V and V_g than expected from above. This is not surprising due to the two-dimensional nature of graphene: our analysis includes only the *k*-states perpendicular to the electrodes, undercounting the states involved in transport (the slope is independent of the path length L). The spin-valve sample also shows oscillations of $\sigma(V_g)$ in Fig. 5.2b). For this sample L = 450 nm, and we would expect ΔV_g = 2.8 V at V_g' = 90 V (i.e. V_g = -70 V) which agrees reasonably well with the observed spacing of dips $\Delta V_g \sim$ 6 V at large negative V_g in Fig. 5.2b). The four-probe geometry is significantly more complicated than the two-probe analysis of

Fabry-Pérot interference above, since there are multiple interfaces which could give rise to interference. Still it is reasonable that quantum interference effects are responsible for the oscillations in the four-probe resistivity (Fig. 5.2b), and for the observed changes in magnitude and sign of the spin-valve signal with gate voltage (Fig. 5.4b).

5.5 Conclusion

In conclusion, we have observed the non-local resistance arising from a spin current in graphene in a non-local four-probe measurement. The spin-valve signal varies with gate voltage in magnitude and sign due to interference arising from the quantum-coherent transport through graphene, which is also evidenced by Fabry-Pérot-like interference patterns observed in a similar sample, and oscillations in the four-probe resistivity of the spin-valve sample. The magnitude of the spin-valve signal is roughly inversely proportional to temperature, and is observable at room temperature. Injection and detection of pure spin currents in graphene opens possibilities to examine theoretically predicted new phenomena such as the spin Hall effect[105] and half-metallicity[111] in graphene ribbons. Because of the high current-carrying capability and long mean-free path at room temperature, graphene is also an excellent candidate for room-temperature spintronics applications.

The results of this chapter are published in Applied Physics Letters[129]. After submission of our results[130], another group [118] published non-local four-

probe spin-valve experiments in graphene, submitted earlier than our work. Ref. 15 showed that spin relaxation time in graphene is quite short and only up to a few hundred *ps*. The origin of unexpected such a short spin relaxation time in graphene is still unknown, and is a subject of significant theoretical[131-132] and experimental [117-118, 133]work. One of the possible reasons is momentum relaxation due to charged impurity scattering, but a recent report[133] shows that charged impurity scattering is not the primary source of spin relaxation in graphene.

Chapter 6. Insulating Behavior in Ultra-thin Bismuth Selenide Field Effect Transistors

6.1 Introduction to Topological Insulator

Three-dimensional(3D) topological insulator is a new class of material that has a bulk band gap and two-dimensional gapless surface states on every surface. The surface state has a Dirac spectrum like graphene, but is singly-degenerate; there is a single Dirac cone which is singly spin-degenerate. The real electron spin plays the role of the pseudospin in graphene, and the surface state exhibits spin-momentum locking and absence of back scattering or localization by time-reversal symmetric disorder[30-32, 34-35, 134].

The existence of surface states in topological insulator Bi_2Se_3 was predicted theoretically [2] and observed recently by angle-resolved photoemission spectroscopy (ARPES)[30-32] and scanning tunneling spectroscopy (STS)[33-35] (see Figure 6.1). ARPES measurements indicate Bi_2Se_3 has a single Dirac cone, gapless surface state in the bulk gap. Bi_2Se_3 seems to be one of the most promising in applications in that it has a large bulk band gap ~ 0.3 eV, corresponding to 3600K and could therefore behave as a topological insulator up to high temperatures. However there has been a big obstacle to achieving electronic transport experiments which are dominated by surface state transport [135-138]: in typical samples the Fermi level in Bi_2Se_3 is not located inside the bulk gap, but in the conduction band. Due to high n-doping,

metallic bulk conduction dominates electronic transport in Bi_2Se_3 and makes it difficult to observe the novel properties of surface states[139-141]. An increase in the Fermi level with time has been observed even at low temperature and in ultra-high vacuum (UHV) in ARPES measurements [30-32], but the origin of high n-doping is not clear at this time.

One strategy to reduce the contribution of bulk conduction is to fabricate very thin Bi_2Se_3 layers, and some electronic transport experiments on thin Bi_2Se_3 films[139-140] and crystals[141-142] have been reported. An interesting question is: How thin can Bi_2Se_3 be while retaining its three dimensional topological insulator character? The thinnest layer that maintains a 2:3 Bi:Se stoichiometry is the quintuple layer (QL)_of 5 alternating Se and Bi planes, while the thinnest slab which retains the symmetry of bulk Bi_2Se_3 is one unit cell, or three QL units, thick.

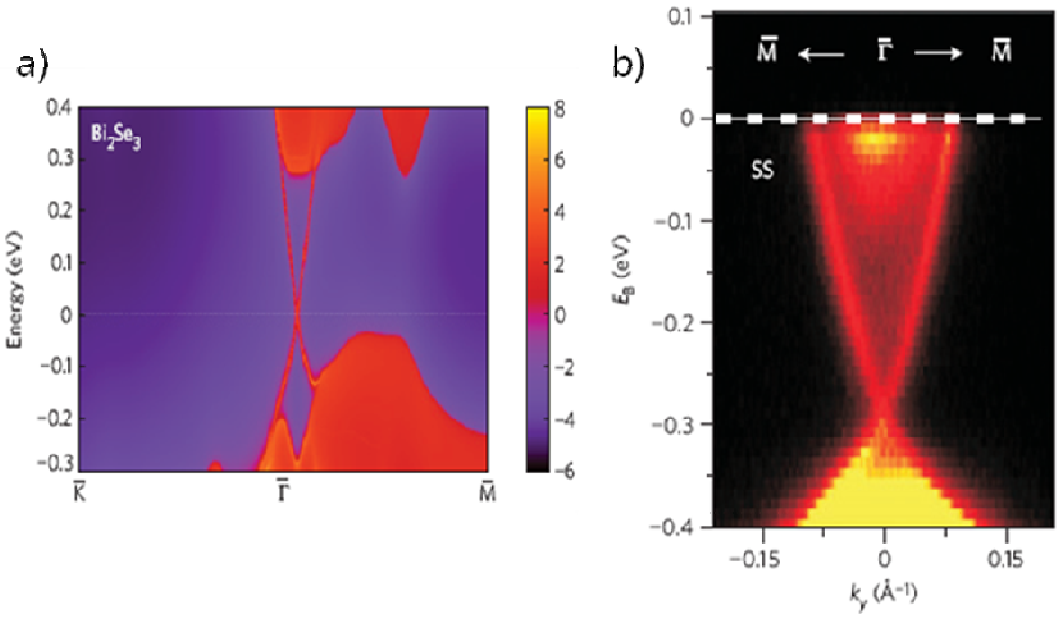

Fig. 6.1. a) Energy and momentum dependence of the LDOS b) ARPES spectra of Bi_2Se_3. Figures are from references [32, 134]

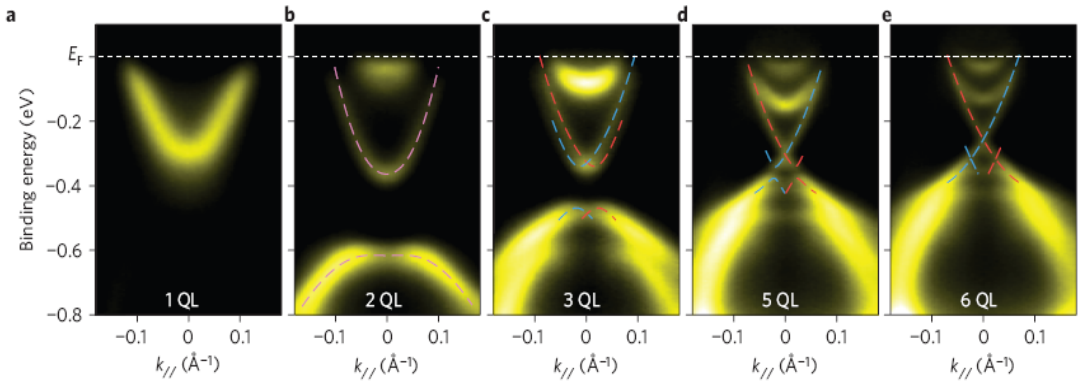

Fig. 6.2. ARPES spectra of 1~6 QLs measured at room temperature. Figure is from a reference [36].

In reference[36], Zhang et al, reported ARPES measurement in 1~6 QL Bi_2Se_3 films as seen in Fig. 6.2. They observed opening an energy gap of surface states in films of thickness below 6 QLs and reported that the gap size increases with decreased number of QLs as in Fig.6.2. Opening of an energy gap indicates that ultrathin Bi_2Se_3 films of thickness below 6 QL are not three-dimensional topological insulators. However, there has been much theoretical work on ultrathin topological insulator films especially about whether they are topologically trivial or nontrivial, in other words, whether they are conventional insulators or two dimensional topological insulators with gapless spin-full one-dimensional edge states (which cannot be observed with ARPES technique). Several theoretical works[143-145] explain that in few-QL Bi_2Se_3, since overlapping between wavefunctions of two surface states is non-negligible, the surface states may hybridize and open a bulk energy gap, resulting in either a two-dimensional insulator or a quantum spin Hall system with insulating bulk and conducting chiral one-dimensional edge modes[146-149].

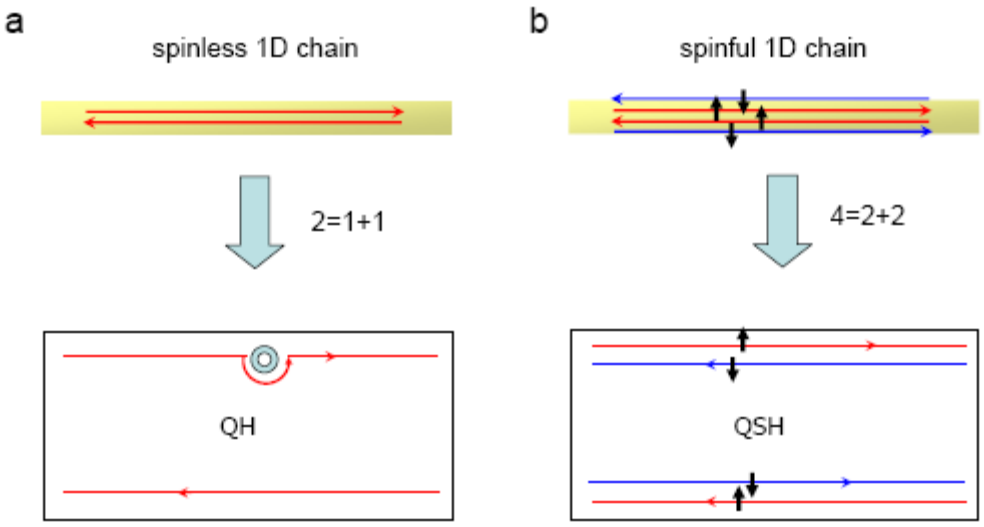

Fig. 6.3. a) spinless b) spin-full 1D chiral edge states in a) quantum Hall states and b) quantum spin Hall states in 2D topological insulator. Figure is from a reference [149].

2D topological insulators are similar to 3D topological insulators, but the difference is that the boundary is edge instead of surface. Instead of momentum-locked two-dimensional surface states, the chiral 1D edge states in 2D topological insulators are spin-momentum locked; i.e. spin-up propagates only one direction, and spin down the opposite direction. 2D topological insulators are also similar to quantum Hall insulators in that both have edge states topologically protected from local perturbation as shown in Fig. 6.3, but the difference is that in 2D topological insulators time reversal symmetry is conserved and edge states come in spin-momentum locked pairs, preserving time-reversal symmetry[149]. 2D topological insulator was predicted theoretically in 2006[150] and realized experimentally next year in HgTe quantum well[151]. König *et al* measured a quantized conductance ~ $2e^2/h$, indicating ballistic transport through two edge modes, similar to the quantum Hall effect without external magnetic field as in Fig. 6.4[149, 151].

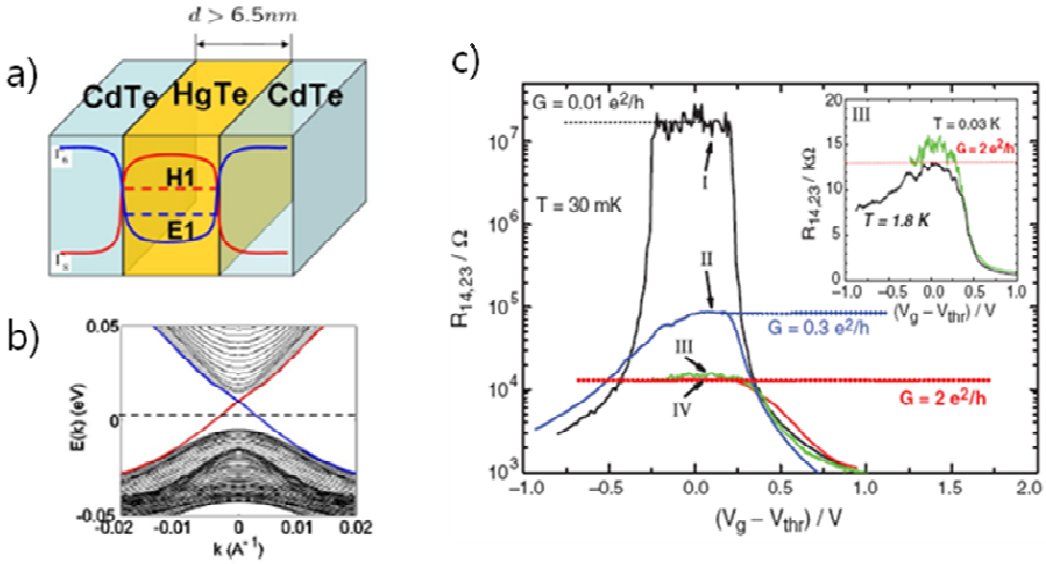

Fig. 6.4. a) schematic figure of HgTe quantum well, b) calculated band structure of HgTe quantum well c) 4 probe resistance measured at T=30mK in HgTe quantum well devices with various d. Devices III and IV corresponds to d=7.3nm and show quantized conductance G~$2e^2/h$. Figures are from references [149, 151].

In the following sections, I will discuss electronic transport measurement conducted in ultrathin Bi_2Se_3 devices consisting of three quintiple layers (1 unit cell) as a function of gate voltage and temperature. I observed clear insulating behavior beyond a threshold gate voltage, with activated energy gaps up to 250 meV. The results indicate that 3 QL Bi_2Se_3 crystals are conventional insulators with energy gaps exceeding 250 meV rather than 2D topological insulator with gapless edge states. This work is published in Ref [152].

6.2 Sample Fabrication and Characterization

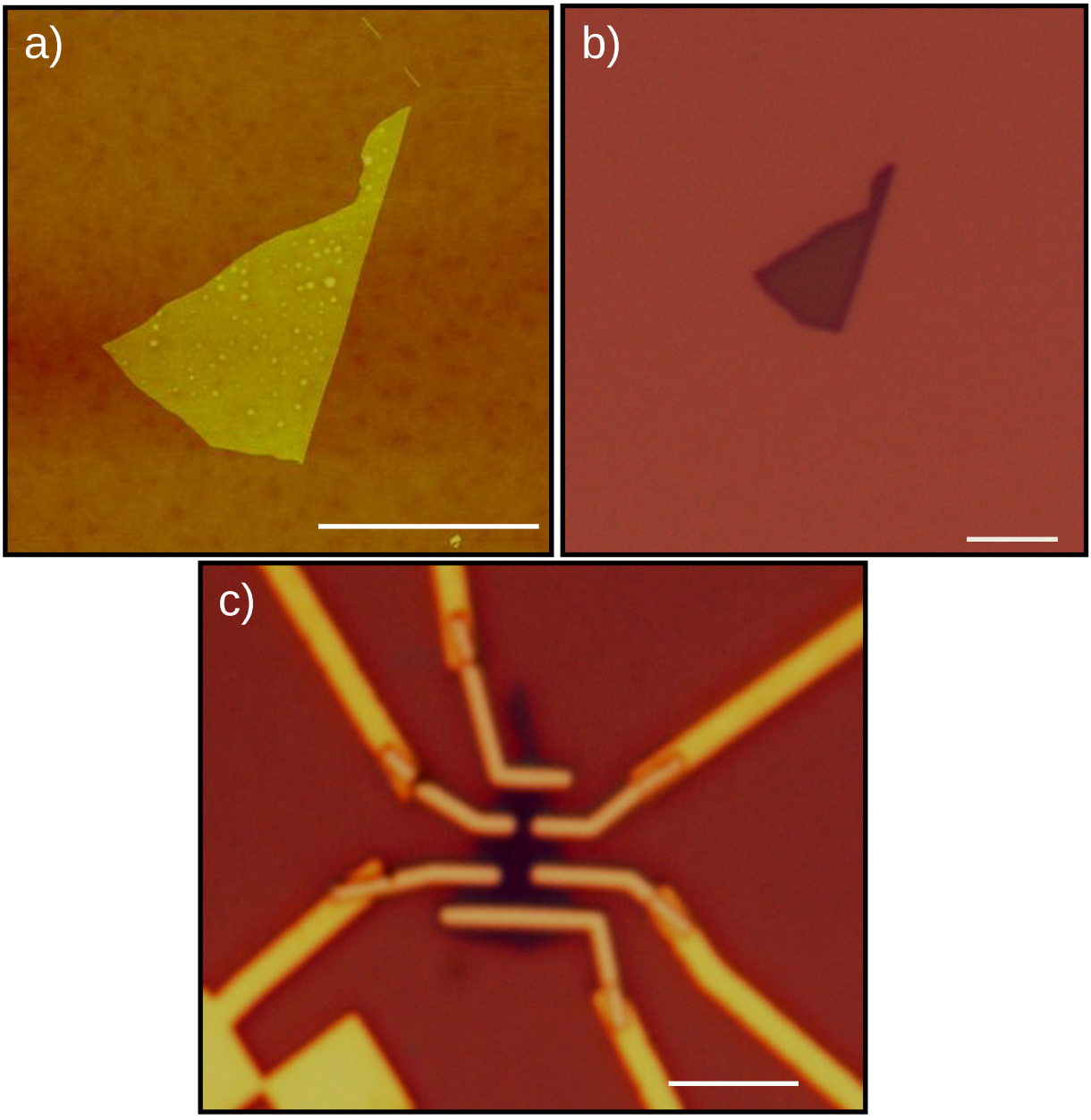

Fig. 6.5. Atomic force micrograph (a) and optical micrographs (b-c) of a 3.5 nm thick exfoliated Bi_2Se_3 sample on SiO_2/Si substrate. Panel (c) shows the completed device with Pd electrodes contacting the device and larger Cr/Au electrodes leading to bonding pads. Scale bars in (a-c) are 4 microns.

Bi_2Se_3 crystals were prepared as described in Reference[135]. Bulk carrier concentrations (*n*-type) were in the range of 2-4x10^{18} cm^{-3}. Bi_2Se_3 was mechanically exfoliated on substrate of 300nm SiO_2 over a conducting Si back gate using a "Scotch tape" method similar to that used for graphene[153]. Fig. 6.5a shows an optical micrograph of a typical mechanically exfoliated Bi_2Se_3 crystal on SiO_2/Si. Crystals of thickness 3.5nm-30nm were found, and could be differentiated by color contrast similar to few-layer graphene[154]. The thickness of the samples was measured by atomic force microscopy (AFM), which may overestimate the true thickness of the crystal as is observed for graphene on SiO_2[154]. The thinnest samples (thickness t = 3.5nm, corresponding to ~3 QLs) were chosen for this study. Electron beam lithography was used to define Pd electrodes; Fig.6.5b shows the completed device. No adhesion layer was used; I found that using Cr or Ti as an adhesion layer makes contact resistance increase rapidly with time, which might be related to oxidation of adhesion layer.

6.3 Electrical Measurement and Discussion

Fig. 6.6 shows the gate-voltage (V_g) dependent transport properties of four Bi_2Se_3 transistors of various thicknesses. For thicker samples (Sample 1, t = 14 nm; and Sample 2, t = 6.5 nm), the sheet conductivity measured in a four-probe configuration is shown. For the thinnest samples (Samples 3 and 4, t = 3.5 nm) the two-probe conductance is shown as a function of V_g. Because of the high sample resistance at low temperatures and negative V_g, I was unable to perform four-probe measurements on the thinnest samples. I always observe *n*-type doping in exfoliated

Bi_2Se_3, and for Samples 1 and 2 the carrier density n determined by Hall effect at V_g = 0, n = 1.5 x 10^{13} cm^{-2} for Sample 1, and n = 2.5 x 10^{13} cm^{-2} for Sample 2, exceeds the density of the surface state at the conduction band edge (~5 x 10^{12} cm^{-2} for one surface, or 1 x 10^{13} cm^{-2} for top and bottom surfaces[30, 32]) indicating that the bulk conduction band must also be populated. The Hall mobility is 1200 cm^2/Vs and 300 cm^2/Vs for Samples 1 and 2 respectively at V_g = 0. The gate-voltage-dependent transport in

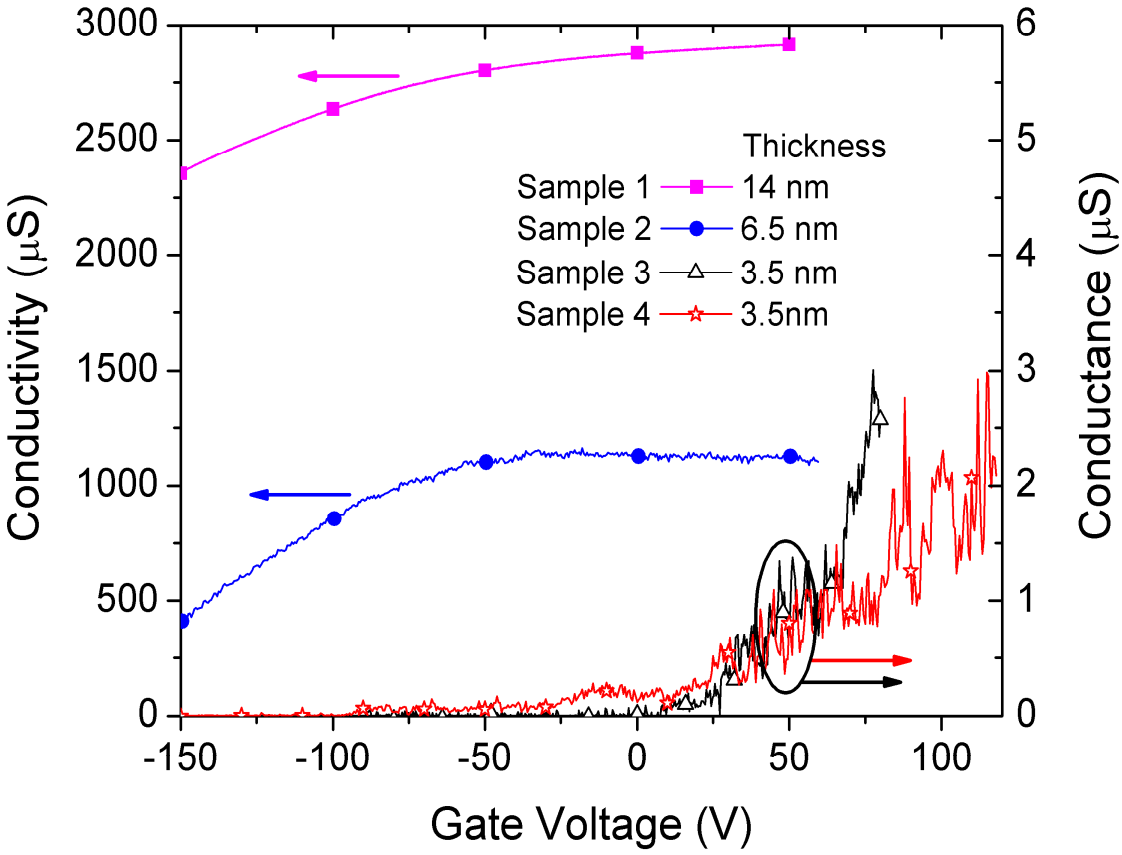

Fig. 6.6. Gate-voltage dependent transport in four exfoliated Bi_2Se_3 samples. For thicker Samples 1 and 2, the four-probe conductivity (left axis) as a function of gate voltage is shown. For thinner Sample 3 and 4, the two-probe conductance (right axis) as a function of gate voltage is shown.

Sample 1 and 2 is qualitatively similar to that observed by other groups for thicker exfoliated crystals[141-142] and films[139]. While weakly (logarithmically) insulating behavior has been observed in thin Bi_2Se_3 films[139, 155], the observation here of transistor-like behavior and a strong (exponentially) insulating state in the thinnest samples is novel, and below I will focus on this behavior in more detail.

Figures 6.7a and 6.7b shows the two-probe conductance of Sample 3 as a function of gate voltage $G(V_g)$ at various temperatures,T showing n-type field effect behavior. (Similar results were obtained for Sample 4). At high T (245 K – 320 K, Fig. 6.7a) I observe that for positive (negative) V_g, the conductance increases (decreases) with decreasing temperature, indicating metallic (insulating) behavior. At lower temperatures (Fig. 6.7b) the conductance decreases with decreasing temperature at all gate voltages. The maximum field effect mobility is ~10 cm^2/Vs at T = 245 K.

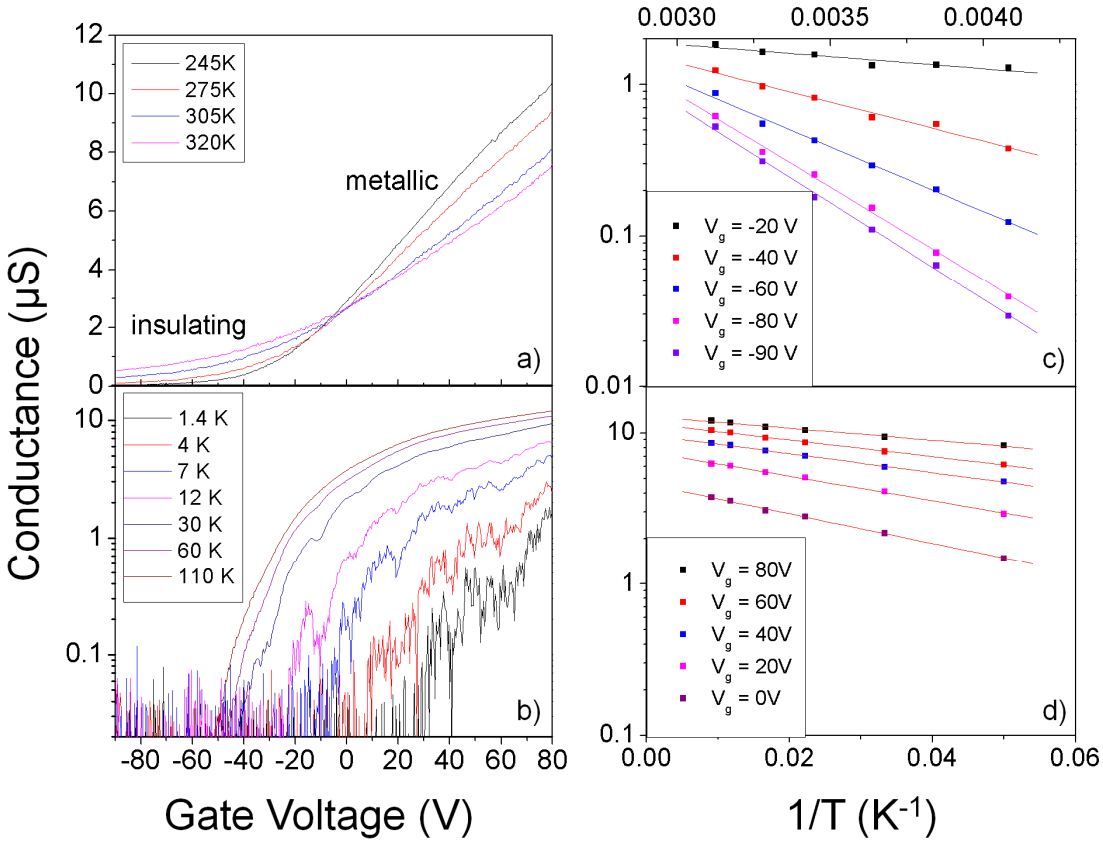

Fig. 6.7. Temperature-dependent conductance of 3.5 nm thick exfoliated Bi_2Se_3 on SiO_2/Si. (a-b) Conductance of Sample 3 vs. gate voltage at various temperatures. (c-d) Conductance of Sample 3 vs inverse temperature on a semilog scale (Arrhenius plot) showing activated behavior. Lines are linear fits to the data.

Figs. 6.7c and 6.7d show the conductance data from Figs. 6.7a and 6.7b on an Arrhenius plot. At negative gate voltage (Fig. 6.7c), strongly activated temperature-dependent conductance is observed; straight lines are fits to $G(V_g) = G_0 e^{-E_a/kT}$ where E_a is the activation energy, k is Boltzmann's constant, and G_0 a constant prefactor. At positive V_g and lower temperatures (Fig. 6.7d), activated behavior is also seen with much smaller activation energies.

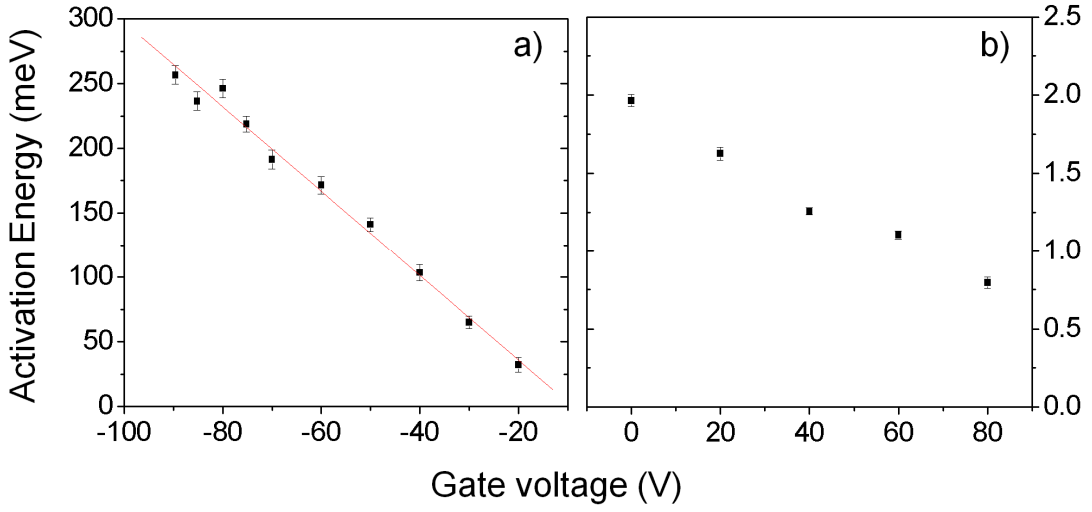

Fig. 6.8. Activation energy as a function of gate voltage determined from fits in Figs. 6.7c and 6.7d.

Figs. 6.8a and 6.8b show the gate-voltage dependence of the activation energies extracted from Figs. 6.7c and 6.7d. For negative gate voltages, the activation energy rises roughly linearly with gate voltage, extrapolating to zero at a threshold V_g = -10 V, and rising to 250 meV at V_g = -90 V. I interpret the activation energy in this regime as arising due to a barrier to conduction in the bulk; i.e. bulk insulating behavior. (I find the possibility of the activation barrier arising from an insulating contact to a metallic surface state extremely unlikely; first, I observe Ohmic contacts similarly fabricated on slightly thicker Bi_2Se_3, and second, I cannot imagine a scenario in which the contact, which lies on top of the sample, could show activation behavior continuously tuned by gate voltage from metallic to insulating.) I assume the activated behavior arises from activation of electrons from the Fermi energy, E_F to conduction band edge, E_C; that is $E_a = E_C - E_F$. Then the variation of E_a with V_g reflects the variation of E_F: $dE_F/d(eV_g) = -dE_a/d(eV_g)$. The fact that the slope

$dE_F/d(eV_g) << 1$ indicates movement of Fermi level with back gate through localized impurity states in the band gap. A change in the electrochemical potential of the gate $e\Delta V_g$ is the sum of the electrostatic potential change $e\Delta\varphi$ and the Fermi energy change ΔE_F: $e\Delta V_g = e\Delta\varphi + \Delta E_F = e^2\Delta n/C_g + e^2\Delta n/C_t$ where Δn is the change in charge number density, $C_g = 1.15\text{x}10^{-8}$ F/cm^2 is the oxide capacitance per unit area, and $C_t = e^2D(E)$ is the quantum capacitance associated with a density of localized states $D(E)$. Then the slope $dE_F/d(eV_g) = C_g/(C_g+C_t)$. From the slope $dE_F/d(eV_g) = 3.3 \text{ x } 10^{-3}$, I can estimate $D(E) = 2.1\text{x}10^{13}$ eV^{-1}cm^{-2}, and the total charge depleted at $V_g = -90$ V is estimated as $5\text{x}10^{12}$ cm^{-2} from the bandwidth 250 meV. It is notable that similar behavior was observed in another exfoliated transition-metal chalcogenide, conventional semiconductor MoS_2 FETs on SiO_2[156], where field-effect mobilities of 10-50 cm^2/Vs and a localized state density of $7 \text{ x } 10^{12}$ eV^{-1}cm^{-2} were measured. Below $T = 110$K, activated conduction behavior is seen even at positive gate voltage (Fig. 6.7b) and the activation energy is plotted in Figure 6.8b. I attribute the very small activation energies in Fig. 6.7b to a small Schottky barrier between the Pd contacts and the insulating ultrathin Bi_2Se_3.

The energy barrier in our ultrathin Bi_2Se_3 FETs is surprisingly large, approaching the bulk energy gap of ~300 meV. I interpret the activation energy as arising from an insulating state in the Bi_2Se_3, due to coupling of the top and bottom surface states. The magnitude of the energy gap is somewhat larger than the gap of 5 – 50 meV theoretically predicted for 3 QL Bi_2Se_3[143-145] and the gap of 130 meV observed for 3 QL Bi_2Se_3 by ARPES experiments[36], though it is comparable to the measured gap for 2 QL Bi_2Se_3 [36]. This suggests that the significant density of

localized states $D(E) = 2.1\text{x}10^{13}$ $eV^{-1}cm^{-2}$ observed in our experiment may reflect localization of the surface-state-derived bands (which are no longer topologically protected by localization), and conduction may occur in the bulk quantum-well states which should be separated by a gap significantly larger than the bulk gap of 300 meV.

The absence of any *p*-type conduction channel observed up to $V_g = -90$ V indicates that the actual transport gap may be even larger than 250 meV; in principle one would expect that the high-workfunction Pd contacts would show a smaller barrier for *p*-type injection. The observation of conductance $G < 10$ nS corresponds to a mean free path for any one-dimensional edge modes < 1 nm; I therefore conclude that it is unlikely that the ultrathin Bi_2Se_3 is in the quantum spin Hall state.

6.4 Conclusion

In conclusion, I have fabricated field-effect transistors from ultrathin Bi_2Se_3 crystals obtained by mechanical exfoliation. The Bi_2Se_3 FETs show *n*-type behavior, with a clear insulating OFF state and energy barriers up to 250 meV. The small subthreshold swing indicates a large density of trap states $D(E) = 2.1\text{x}10^{13}$ $eV^{-1}cm^{-2}$. The observation of a true insulating state in topological insulator Bi_2Se_3 is presumed to be due to coupling of the top and bottom surface states, resulting in a conventional two-dimensional insulator. Whether 1-2QL and 4-5QL are 2D insulators topologically trivial or nontrivial with gapless edge states is still an open question in experiment.

Bibliography

1. K. S. Novoselov, *et al.*, *Two-dimensional gas of massless Dirac fermions in graphene.* Nature, 2005. **438**: p. 197.

2. K. S. Novoselov, *et al.*, *Two-dimensional atomic crystals.* PNAS, 2005. **102**(30): p. 10451.

3. Y. Zhang, *et al.*, *Experimental observation of the quantum Hall effect and Berry's phase in graphene.* Nature, 2005. **438**: p. 201.

4. R. Saito, *et al.*, *Physical Properties of Carbon Nanotubes.* Imperial College Press 1998.

5. P.R. Wallace, *The band theory of graphite.* . Physical Review, 1947. **71**: p. 622.

6. C. Schonenberger, *Bandstructure of graphene and carbon nanotubes: An exercise in condensed matter physics.* 2000.

7. J.C. Slonczewski, *et al.*, *Band structure of graphite.* Physical Review, 1958. **109**: p. 282.

8. N. Aschcroft, *et al.*, *Solid State Physics.* Wiley, 1997.

9. J. Sakurai, *Advanced quantum mechanics.* Addison Wesley, 1999.

10. D. Tománek and S.G. Louie, *Theory and observation of highly asymmetric atomic structure in scanning–tunneling-microscopy images of graphite.* Phys. Rev. B, 1987. **35**: p. 7790.

11. E. McCann, *et al.*, *Landau-Level Degeneracy and Quantum Hall Effect in a Graphite Bilayer.* Phys. Rev. Lett., 2006. **96**: p. 086805.

12. B. Partoens, *et al.*, *From graphene to graphite: Electronic structure around the K point.* Phys. Rev. B, 2006. **74**: p. 075404.

13. C. Lu, *et al.*, *Influence of an electric field on the optical properties of few-layer graphene with AB stacking.* Phys. Rev. B, 2006. **73**: p. 144427.

14. J. Nilsson, *et al.*, *Electron-electron interactions and the phase diagram of a graphene bilayer.* Phys. Rev. B, 2006. **73**: p. 214418.

15. M. Koshino, *et al.*, *Transport in bilayer graphene: Calculations within a self-consistent Born approximation.* Phys. Rev. B 2006. **73**: p. 245403.

16. F. Guinea, *et al.*, *Electronic properties of disordered two-dimensional carbon.* Phys. Rev. B, 2006. **73**: p. 1200.

17. M. Dresselhaus, *et al.*, *Intercalation compounds of graphite* Adv. Phys. , 2002. **51**: p. 1.

18. J. Charlier, *et al.*, *First-principles study of the electronic properties of graphite.* Phys. Rev. B, 1991. **43**: p. 4579.

19. E. McCann, *Asymmetry gap in the electronic band structure of bilayer graphene.* Phys. Rev. B 2006. **74**: p. 161403.

20. K. S. Novoselov, *et al.*, *Unconventional quantum Hall effect and Berry's phase of 2 in bilayer graphene.* Nature physics, 2006. **2**: p. 177.

21. A. C. Ferrari, *et al.*, *Raman Spectrum of Graphene and Graphene Layers.* Phys. Rev. Lett., 2006. **97**: p. 187401.

22. F. Miao, *et al.*, *Phase-coherent transport in graphene quantum billiards.* Science, 2007. **317**: p. 1530.

23. C. Berger, *et al.*, *Electronic confinement and coherence in patterned epitaxial graphene.* Science, 2006. **312**: p. 1191.

24. S. Cho and M. Fuhrer, *Massless and Massive Particle-in-a-Box States in Single- and Bi-Layer Graphene.* Nano Res., 2011. **4**: p. 385.

25. V. Guttal and D. Stroud, *Model for a macroscopically disordered conductor with an exactly linear high-field magnetoresistance.* Phys. Rev. B, 2005. **71**: p. 201304.

26. J. H. Chen, *et al.*, *Charged-impurity scattering in graphene.* Nature Physics, 2008. **4**: p. 377.

27. J. Martin, *et al.*, *Observation of Electron-Hole Puddles in Graphene Using a Scanning Single Electron Transistor.* Nature Physics, 2007. **4**: p. 144.

28. S. Cho and M. Fuhrer, *Charge transport and inhomogeneity near the minimum conductivity point in graphene.* Phys. Rev. B, 2008. **77**: p. 081402.

29. S. Cho, *et al.*, *Gate-tunable graphene spin valve* Appl. Phys. Lett. 91, 123105 (2007);, 2007. **91**: p. 123105.

30. D. Hsieh, *et al.*, *A tunable topological insulator in the spin helical Dirac transport regime.* Nature, 2009. **460(7259)**: p. 1101.

31. Y. L. Chen, *et al.*, *Experimental Realization of a Three-Dimensional Topological Insulator, Bi2Te3.* Science, 2009. **325 (5937)**: p. 178.

32. Y. Xia, *et al.*, *Observation of a large-gap topological-insulator class with a single Dirac cone on the surface.* Nat. Phys., 2009. **5 (6)**: p. 398.

33. T. Hanaguri, *et al.*, *Momentum-resolved Landau-level spectroscopy of Dirac surface state in Bi2Se3.* Phys. Rev. B, 2010. **82**: p. 081305(R).

34. P. Roushan, *et al.*, *Topological surface states protected from backscattering by chiral spin texture.* Nature, 2009. **460 (7259)**: p. 1106.

35. T. Zhang, *et al.*, *Experimental Demonstration of Topological Surface States Protected by Time-Reversal Symmetry.* Phys. Rev. Lett., 2009. **103**: p. 266803.

36. Y. Zhang, *et al.*, *Crossover of the three-dimensional topological insulator Bi2Se3 to the two-dimensional limit.* Nat. Phys., 2009. **6**: p. 584.

37. S. Cho, *et al.*, *Insulating Behavior in Ultrathin Bismuth Selenide Field Effect Transistors.* Nano Lett., 2011. **11**: p. 1925.

38. T. Ohta, *et al.*, *Controlling the electronic structure of bilayer graphene.* Science, 2006. **313**: p. 951.

39. K. S. Kim, *et al.*, *Large-scale pattern growth of graphene films for stretchable transparent electrodes.* nature, 2009. **457**: p. 706.

40. K. S. Novoselov, *et al.*, *Electric field effect in atomically thin carbon films.* Science, 2004. **306**: p. 666.

41. Y. Zhang, *et al.*, *Electric field modulation of galvanomagnetic properties of mesoscopic graphite.* Phys. Rev. Lett., 2005. **94**: p. 176803.

42. S. Roddaro, *et al.*, *The Optical Visibility of Graphene: Interference Colors of Ultrathin Graphite on SiO2.* Nano Lett., 2007. **7**: p. 2707.

43. A. C. Ferrari, *et al.*, *Raman Spectrum of Graphene and Graphene Layers.* Phys. Rev. Lett., 2006. **97**: p. 187401.

44. K. von Klitzing, *et al.*, *New Method for High-Accuracy Determination of the Fine-Structure Constant Based on Quantized Hall.* Phys. Rev. Lett., 1980. **45**: p. 494.

45. L. M. Marlard, *et al.*, *Probing the electronic structure of bilayer graphene by Raman scattering.* Phys. Rev. B, 2007. **76**: p. 201401.

46. F. Miao, *et al.*, *Phase-coherent transport in graphene quantum billiards.* Science, 2007. **317**: p. 1530.

47. Y. Zhang, *et al.*, *Experimental observation of the quantum Hall effect and Berry's phase in graphene.* Nature, 2005. **438**: p. 201.

48. M. Koshino and T. Ando, *Transport in bilayer graphene: Calculations within a self-consistent Born approximation.* Phys. Rev. B, 2006. **73**: p. 245403.

49. E. McCann and V.I. Fal'ko, *Landau-Level Degeneracy and Quantum Hall Effect in a Graphite Bilayer.* Phys. Rev. Lett., 2006. **96**: p. 086805.

50. S.vDas Sarma, *et al.*, *Many-body interaction effects in doped and undoped graphene: Fermi liquid versus non-Fermi liquid.* PHys. Rev. B, 2007. **75**: p. 121406(R).

51. J. Nilson, *et al.*, *Electronic Properties of Graphene Multilayers.* phys. Rev. Lett., 2006. **97**: p. 266801.

52. B. Partoens and F. M. Peeters, *From graphene to graphite: Electronic structure around the K point.* Phys. Rev. B, 2006. **74**: p. 075404.

53. T. Ohta, *et al.*, *Controlling the Electronic Structure of Bilayer Graphene.* Science, 2006. **313**: p. 951.

54. E. A. Henriksen, *et al.*, *Cyclotron Resonance in Bilayer Graphene.* Phys. Rev. Lett., 2008. **100**: p. 087403

55. A. Bostwick, *et al.*, *Quasiparticle dynamics in graphene.* Nature Physics, 2007. **3**: p. 36.

56. W. W. Toy and M. S. Dresselhaus, *Minority carriers in graphite and the H-point magnetoreflection spectra.* Phys. Rev. B 1977. **15**: p. 4077.

57. M. S. Dresselhaus and G. Dresselhaus, *Intercalation compound of graphite.* Advances in Physics 1981. **30**: p. 139.

58. W. Liang, *et al.*, *Fabry-perot interference in a nanotube electron waveguide.* Nature, 2001. **411**: p. 665.

59. J. Cao, *et al.*, *Electron transport in very clean, as-grown suspended carbon nanotubes.* Nature Materials, 2005. **4**: p. 745.

60. P.R. Wallace, *The Band Theory of Graphite.* Phys. Rev. , 1947. **71**: p. 622.

61. Z. Jiang, *et al.*, *Infrared Spectroscopy of Landau Levels of Graphene.* phys. Rev. Lett., 2007. **98**: p. 197403.

62. M. L. Sadowski, *et al.*, *Landau Level Spectroscopy of Ultrathin Graphite Layers.* Phys. Rev. Lett., 2006. **97**: p. 266405.

63. S. Adam, *et al., self-consistent theory for graphene transport.* PNAS, 2007. **104**: p. 18392.

64. J. Martin, *et al., Observation of electron–hole puddles in graphene using a scanning single-electron transistor.* Nature Physics, 2008. **4**: p. 144.

65. J.H. Chen, *et al., Charged Impurity Scattering in Graphene.* Nature Physics, 2008. **4**: p. 377.

66. A. Misu, *et al., Near Infrared Reflectivity of Graphite under Hydrostatic Pressure. I. Experiment.* J. Phys. Soc. Jap. , 1979. **47**: p. 199.

67. V. Chejanov, *et al., Selective transmission of Dirac electrons and ballistic magnetoresistance of n-p junctions in graphene* phys. Rev. B, 2006. **74**: p. 041403(R)

68. V. Chejanov, *et al., he focusing of Electron Flow and a Veselago Lens in Graphene p-n Junctions.* Science, 2007. **315**: p. 1252.

69. M. I. Katsnelson, *et al., Chiral tunnelling and the Klein paradox in graphene.* Nature Physics, 2006. **2**: p. 620.

70. C. H. Park, *et al., Anisotropic behaviours of massless Dirac fermions in graphene under periodic potentials.* Nature Physics, 2008. **4**: p. 213.

71. M.B Lundeberg and J.A. Folk, *Spin-resolved quantum interference in graphene.* Nature Physics, 2009. **5**: p. 894.

72. A. F Young and P. Kim, *Quantum interference and Klein tunnelling in graphene heterojunctions.* Nature Physics, 2009. **5**: p. 222.

73. E. Rossi, *et al., Signatures of Klein tunneling in disordered graphene p-n-p junctions.* phys. Rev. B, 2010. **81**: p. 121408.

74. N. Gu, *et al., Landau level Collapse in Gated Graphene Structures.* arXiv:1003.2399, 2010.

75. M. Fuhrer S. Cho, *Charge transport and inhomogeneity near the minimum conductivity point in graphene.* Phys. Rev. B, 2008. **77**: p. 081402(R).

76. F. Miao, *et al., Phase-Coherent Transport in Graphene Quantum Billiards.* Science, 2007. **317**: p. 1530.

77. J.H. Chen, *et al., Printed Graphene Circuits.* Advanced Materials, 2007. **19**: p. 3623.

78. S. Adam, *et al., A self-consistent theory for graphene transport.* Proceedings of the National Academy of Sciences, 2007. **104**: p. 18392.

79. T. Ando, *Screening Effect and Impurity Scattering in Monolayer Graphene.* Journal of the Physical Society of Japan, 2006. **75**: p. 074716.

80. K. Nomura and A. H. MacDonald, *Quantum Transport of Massless Dirac Fermions.* Phys. Rev. Lett, 2007. **98**: p. 076602.

81. M. I. Katsnelson, European Physical Journal B, 2006. **51**: p. 157.

82. E. H. Hwang, *et al.*, *Carrier transport in 2D graphene layers.* Phys. Rev. Lett, 2006. **98**: p. 186806.

83. K. S. Novoselov, *et al.*, *Two-dimensional atomic crystals.* Proceedings of the National Academy of Sciences, 2005. **102**: p. 10451.

84. Because the sample is not an ideal Hall bar we estimate an error of order 10% in determining the numerical factor of proportionality between the longitudinal resistivity and the resistance[16]. However, error in this numerical factor will only rescale the vertical axes of Figs. 1b, 2a, 2b, 3 (left and right), and 4. Fig. 1c would be modified, however the half-integer QHE plateaus are unchanged since ρ_{xx} is zero there, and we find that the $\upsilon = 0$ plateau is insensitive to changing the numerical factor by as much as a factor of two. Crosstalk between the longitudinal and Hall measurements is eliminated by taking the symmetric and antisymmetric components of the magnetic field dependences, respectively (subtracted components are always <10% of the total).

85. Y. Zhang, *et al.*, *Experimental observation of the quantum Hall effect and Berry's phase in graphene.* Nature, 2005. **438**: p. 201.

86. D. A. Abanin, *et al.*, *Dissipative Quantum Hall Effect in Graphene near the Dirac Point.* Phys. Rev. Lett, 2007. **98**: p. 196806.

87. Z. Jiang, *et al.*, *Quantum Hall States near the Charge Neutral Dirac Point in Graphene.* Phys. Rev. Lett, 2007. **99**: p. 106802.

88. Y. Zhang, *et al.*, *Landau-Level Splitting in Graphene in High Magnetic Fields.* Phys. Rev. Lett, 2006. **96**: p. 136806.

89. T. Ando and Takeshi Nakanishi, *Impurity Scattering in Carbon Nanotubes – Absence of Back Scattering.* Journal of the Physical Society of Japan, 1998. **67**: p. 1704.

90. S. V. Morozov, *et al.*, *Strong Suppression of Weak Localization in Graphene.* Phys. Rev. Lett, 2006. **97**: p. 016801.

91. K. S. Novoselov, *et al.*, *Electric Field Effect in Atomically Thin Carbon Films.* Science, 2004. **306**: p. 666.

92. E. H. Hwang, *et al.*, *Transport in chemically doped graphene in the presence of adsorbed molecules.* Phys. Rev. B, 2006. **76**: p. 195421.

93. R. Magier and D. J. Bergman, *Strong-field magnetotransport of two-phase disordered media in two and three dimensions: Exact and approximate results.* Phys. Rev. B, 2006. **74**: p. 094423.

94. M. Trushin and J. Schliemann, *The Minimum Electrical and Thermal Conductivity of Graphene: Quasiclassical Approach.* Phys. Rev. Lett, 2007. **99**: p. 216602.

95. A. Cottet, *et al.*, *Nanospintronics with carbon nanotubes.* Semiconductor Science and Technology, 2006. **21**: p. S78.

96. E. W. Hill, *et al.*, *Graphene Spin Valve Devices.* IEEE Trans. Magn. , 2006. **42**: p. 2694.

97. K. Tsukagoshi, *et al.*, *Coherent transport of electron spin in a ferromagnetically contacted carbon nanotube.* . Nature, 1999. **401**: p. 572.

98. D. Orgassa, *et al.*, *Spin injection into carbon nanotubes and a possible application in spin-resolved scanning tunnelling microscopy.* . Nanotechnology, 2001. **12**: p. 281.

99. R. Thamankar, *et al.*, *Spin-polarized transport in magnetically assembled carbon nanotube spin valves.* Applied Physics Letters, 2006. **89**: p. 033119.

100. H. T. Man, *et al.*, *Spin-dependent quantum interference in single-wall carbon nanotubes with ferromagnetic contacts.* . Phys. Rev. B, 2006. **73**: p. 241401.

101. Y.-F. Chen, *Semiconducting Carbon Nanotube Transistors: Electron and Spin Transport Properties.* , in *physics*. 2006, University of Maryland: College Park.

102. T. Ando and T. Nakanishi, *Impurity scattering in carbon nanotubes: Absence of backscattering.* . J. Phys. Soc. Jpn., 1998. **67**: p. 1713.

103. T. Dürkop, *et al.*, *Properties and applications of high-mobility semiconducting nanotubes.* . Journal of Physics: Condensed Matter, 2004. **16**: p. R553.

104. K. I. Bolotin, *et al.*, *Temperature-Dependent Transport in Suspended Graphene.* Phys. Rev. Lett., 2008. **101**: p. 096802.

105. C. L. Kane and E. J. Mele, *Quantum Spin Hall Effect in Graphene.* Phys. Rev. Lett., 2005. **95**: p. 226801.

106. H. Min, *et al.*, *Intrinsic and Rashba spin-orbit interactions in graphene sheets.* Phys. Rev. B, 2006. **74**: p. 165310.

107. D. Huertas-Hernando, *et al.*, *Spin relaxation times in disordered graphene.* Eur. Phys. J. Special Topics 2007. **148**: p. 177.

108. I. Žutić and test
test, *Spintronics: Fundamentals and applications.* Rev. Mod. Phys., 2004. **76**: p. 323.

109. K. S. Novoselov, *et al.*, *Two-dimensional gas of massless Dirac fermions in graphene.* Nature, 2005. **438**: p. 197.

110. Y. Zhang, *et al.*, *Experimental observation of the quantum Hall effect and Berry's phase in graphene.* Nature, 2005. **438**: p. 201.

111. Y.-W. Son, *et al.*, *Half-metallic graphene nanoribbons.* . Nature. **444**: p. 347.

112. Y. Ji, *et al.*, *Non-local spin injection in lateral spin valves.* J. Phys. D: Appl. Phys. , 2007. **40**: p. 1280.

113. Samir Garz´on, *Spin injection and detection in copper spin valve structures.* Ph.D thesis, University of Maryland, 2005: p. 32.

114. F. J. Jedema, *Electrical spin injection and accumulation at room temperature in an all-metal mesoscopic spin valve.* Nature, 2001. **410**: p. 345.

115. F. J. Jedema, *et al.*, *Spin Injection and Spin Accumulation in Permalloy–Copper Mesoscopic Spin Valves.* . Journal of Superconductivity: Incorporating Novel Magnetism, 2002. **15**: p. 27.

116. F. J. Jedema, *et al.*, *Spin injection and spin accumulation in all-metal mesoscopic spin valves.* Phys. Rev. B, 2003. **67**: p. 085319.

117. N. Tombros, *et al.*, *Separating spin and charge transport in single-wall carbon nanotubes.* . Phys. Rev. B, 2006. **73**: p. 233403.

118. N. Tombros, *et al.*, *Electronic spin transport and spin precession in single graphene layers at room temperature.* Nature, 2007. **448**: p. 571.

119. K. S. Novoselov, *et al.*, *Unconventional quantum Hall effect and Berry's phase of 2π in bilayer graphene.* . Nature Physics, 2006. **2**: p. 177.

120. S. Adam, *et al.*, *A self-consistent theory for graphene transport. Condensed Matter Archive, 0705.1540 (2007).* PNAS, 2007. **104**: p. 18392.

121. J.H. Chen, *et al.*, *Charged-impurity scattering in graphene.* Nature Physics, 2008. **4**: p. 377.

122. S. Garzon, *et al.*, *Temperature-Dependent Asymmetry of the Nonlocal Spin-Injection Resistance: Evidence for Spin Nonconserving Interface Scattering.* Phys. Rev. Lett., 2005. **94**: p. 176601.

123. S. Cho and M. S. Fuhrer, *Charge Transport and Inhomogeneity near the Charge Neutrality Point in Graphene.* . Phys. Rev. B, 2008. **77**: p. 081402.

124. S. Datta and B. Das, *Electronic analog of the electro-optic modulator. Applied Physics Letters.* Applied Physics Letters, 1990. **56**: p. 665.

125. A. De Martino and R. R. Egger, *spin-orbit coupling and spin precession in carbon nanotubes.* Journal of Physics: Condensed Matter 2005. **17**: p. 5523.

126. S. Sahoo, *et al.*, *Electric field control of spin transport.* . Nature Physics, 2005. **1**: p. 99.

127. W. Liang, *et al.*, *Fabry-Perot interference in a nanotube electron waveguide.* . Nature, 2001. **411**: p. 665.

128. F. Miao, *et al.*, *Phase Coherent Transport of Charges in Graphene Quantum Billiard.* . Science, 2007. **317**: p. 1530.

129. S. Cho, *et al.*, *Gate-tunable graphene spin valve.* Appl. Phys. Lett., 2007. **91**: p. 123105.

130. S. Cho, *et al.*, *Graphene Spin Transistor.* ArXiv.0706.1597, 2007.

131. D. Huertas-Hernando, *et al.*, *Spin-Orbit-Mediated Spin Relaxation in Graphene.* Phys. Rev. Lett., 2009. **103**: p. 146801.

132. N. Castro, *et al.*, *Impurity-Induced Spin-Orbit Coupling in Graphene.* phys. Rev. Lett., 2009. **103**: p. 026804.

133. K. Pi, *et al.*, *Manipulation of Spin Transport in Graphene by Surface Chemical Doping.* Phys. Rev. Lett., 2010. **104**: p. 187201.

134. H. Zhang, *et al.*, *Topological insulators in Bi2Se3, Bi2Te3 and Sb2Te3 with a single Dirac cone on the surface.* Nature Physics, 2009. **5**: p. 438.

135. N. P. Butch, *et al.*, *Strong surface scattering in ultrahigh-mobility Bi2Se3 topological insulator crystals.* Phys. Rev. B, 2010. **81**: p. 241301.

136. D. X. Qu, *et al.*, *Quantum Oscillations and Hall Anomaly of Surface States in the Topological Insulator Bi2Te3.* Science, 2010. **329(5993)**: p. 821.

137. G. S. Jenkins, *et al.*, *Terahertz Kerr and reflectivity measurements on the topological insulator Bi2Se3.* Phys. Rev. B, 2010. **82** p. 125120

138. A. B. Sushkov, *et al.*, *Far-infrared cyclotron resonance and Faraday effect in Bi2Se3.* Phys. Rev. B, 2010. **82**: p. 125110.

139. M. Liu, *et al.*, *Electron interaction-driven insulating ground state in Bi2Se3 topological insulators in the two dimensional limit.* Phys. Rev. B, 2011. **83**: p. 165440.

140. J. G. Checkelsky, *et al.*, *Bulk Band Gap and Surface State Conduction Observed in Voltage-Tuned Crystals of the Topological Insulator Bi2Se3.* Phys. Rev. Lett., 2011. **106**: p. 196801.

141. H. Steinberg, *et al.*, *Surface State Transport and Ambipolar Electric Field Effect in Bi2Se3 Nanodevices.* Nano Lett., 2010. **10**: p. 5032.

142. J. G. Checkelsky, *et al.*, *Quantum Interference in Macroscopic Crystals of Nonmetallic Bi2Se3.* Phys. Rev. Lett., 2009. **103 (24)**: p. 246601.

143. H. Lu, *et al.*, *Massive Dirac fermions and spin physics in an ultrathin film of topological insulator.* Phys. Rev. B 2010. **81**: p. 115407.

144. C. Liu, *et al.*, *Oscillatory crossover from two-dimensional to three-dimensional topological insulators.* Phys. Rev. B, 2010. **81**: p. 041307.

145. J. Linder, *et al.*, *Anomalous finite size effects on surface states in the topological insulator Bi2Se3.* Phys. Rev. B, 2009. **80**: p. 205401.

146. S. Murakami, *et al.*, *Spin-Hall Insulator.* Phys. Rev. Lett., 2004. **93**: p. 156804.

147. C. L Kane and E. J. Mele, *Quantum Spin Hall Effect in Graphene.* Phys. Rev. Lett., 2005. **95**: p. 226801.

148. B. A. Bernevig and S. Zhang, *Quantum Spin Hall Effect.* Phys. Rev. Lett., 2006. **96**: p. 106802.

149. S. C. Zhang X. L. Qi, *The quantum spin Hall effect and topological insulators.* Physics Today, 2010. **63**: p. 33.

150. B. A. Bernevig, *et al.*, *Quantum Spin Hall Effect and Topological Phase Transition in HgTe Quantum Wells.* Science, 2006. **314**: p. 1757.

151. M. König, *et al.*, *Quantum Spin Hall Insulator State in HgTe Quantum Wells.* Science, 2007. **318**: p. 766.

152. S. Cho, *et al.*, *Insulating Behavior in Ultrathin Bismuth Selenide Field Effect Transistors.* Nano Letters, 2011. **11**: p. 1925

153. K. S. Novoselov, *et al.*, *Two-dimensional atomic crystals.* PNAS, 2005(102): p. 10451.

154. Y. Zhang, *et al.*, *Experimental observation of the quantum Hall effect and Berry's phase in graphene.* Nature, 2005. **438**: p. 201.

155. T. Hirahara, *et al.*, *Anomalous transport in an n-type topological insulator ultrathin Bi2Se3 film.* Phys. Rev. B, 2010. **82**: p. 155309.

156. A. Ayari, *et al.*, *Realization and electrical characterization of ultrathin crystals of layered transition-metal dichalcogenides* Journal of Applied Physics 2007. **101**: p. 014507.